INVERSE DESIGN OF PLASMONIC SENSORS: OPTIMIZATION AND PERFORMANCE ENHANCEMENT USING DEEP LEARNING

by

Sakif Yeaser (200021101)
Tasnia Nafs (200021113)
Md. Ikrama Hossain (200021114)

A Thesis Submitted to the Academic Faculty in Partial Fulfillment of the Requirements for the Degree of

BACHELOR OF SCIENCE IN ELECTRICAL AND ELECTRONIC ENGINEERING

Department of Electrical and Electronic Engineering
Islamic University of Technology (IUT)
Gazipur, Bangladesh

October 2025

Declaration of Authorship

We do hereby certify that this thesis, entitled *"Inverse Design of Plasmonic Sensors: Optimization and Performance Enhancement Using Deep Learning"*, comprises original research carried out under the supervision of Dr. Rakibul Hasan Sagor, Professor, Department of Electrical and Electronic Engineering (EEE), Islamic University of Technology (IUT). We further certify that the work was completed entirely during our undergraduate studies at IUT and has not been submitted, in whole or in part, for any other academic degree. All assistance received and all published sources consulted have been duly acknowledged and properly cited, and we accept full responsibility for the integrity and authenticity of the work presented herein.

Signatures of the Candidates

Sakif 20.10.2025

Sakif Yeaser
Student ID: 200021101

Tasnianafs 20.10.2025

Tasnia Nafs
Student ID: 200021113

Ikrama 20.10.2025

Md. Ikrama Hossain
Student ID: 200021114

INVERSE DESIGN OF PLASMONIC SENSORS: OPTIMIZATION AND PERFORMANCE ENHANCEMENT USING DEEP LEARNING

Submitted by

Sakif Yeaser (200021101)
Tasnia Nafs (200021113)
Md. Ikrama Hossain (200021114)

Approved by:

Dr. Rakibul Hasan Sagor

Supervisor and Professor,
Department of Electrical and Electronic Engineering,
Islamic University of Technology (IUT),
Boardbazar, Gazipur-1704.

Date: 20 OCT 2025

Acknowledgement

بسم الله الرحمن الرحيم

In the Name of Allah, the Most Merciful, the Most Compassionate.

First and foremost, all praise and gratitude are due to Allah Subhanahu wa Ta'ala, the Most Merciful and the Most Gracious, for granting us the health, strength, endurance, perseverance, and wisdom to complete this thesis. We offer our deepest thanks to our parents. Their steady care and sacrifice in every form, including financial, physical, and mental support, carried us to this point. Whatever we have achieved stands on their shoulders.

We are grateful to our supervisor, Dr. Rakibul Hasan Sagor, Professor, Department of Electrical and Electronic Engineering, Islamic University of Technology, for guidance, encouragement, and insight that shaped this research work. We also thank Mr. A.K.M. Rakib, Lecturer, Department of EEE, for early mentorship and dedicated teaching that built our foundation. Our appreciation goes to every member of the IUT Photonics Research Group for collegiality, thoughtful dialogue, and the generous sharing of knowledge.

Finally, we thank our friends and the wider IUT community, including faculty, staff, and support personnel. They cared for us in our families' absence, and their steady commitment and cooperation made this journey possible.

Sakif Yeaser

Tasnia Nafs

Md. Ikrama Hossain

October 2025

Table of Contents

Declaration of Authorship **ii**

Certification of Approval **iii**

Acknowledgement **iv**

List of Figures **ix**

List of Tables **xi**

List of Abbreviations **xii**

Abstract **xiii**

1 Introduction **1**

1.1 Plasmonics 1

1.1.1 Metal–Insulator–Metal (MIM) Resonator 2

1.2 Inverse Design 3

1.2.1 Reinforcement Learning 4

1.3 Thesis Objective 5

1.4 Thesis Layout 6

2 Literature Review **8**

2.1 Literature on Plasmonic Refractive-Index MIM Sensors 9

2.2 Literature on Deep-Learning-Based Inverse Design in Plasmonics 15

3 Electromagnetic Wave Theory **18**

3.1 Maxwell's Fundamental Equations 18

3.1.1 Maxwell–Ampère's Law 19

3.1.2 Faraday's Law 19

3.1.3 Gauss's law For Electric fields 20

3.1.4 Gauss's Law for Magnetic Fields 21

3.2 Constitutive Equations 21

3.3 Electromagnetic Wave Equations 23
3.3.1 Electromagnetic Wave Equations—Derivation 24
3.4 Electromagnetic Modes 25
3.4.1 Transverse Magnetic (TM) Mode 25
3.4.2 Transverse Electric (TE) Mode 26
3.4.3 Transverse Electromagnetic (TEM) Mode 26

4 Surface Plasmon Resonance **27**
4.1 Surface Plasmon Polariton (SPP) 27
4.2 Dispersion Relations 28
4.3 Propagation and Decay Properties 30
4.3.1 Propagation at the Metal–Insulator Interface 31
4.4 Coupling and Resonance Condition 32
4.4.1 Coupling Condition 32
4.4.2 Resonance Condition 33
4.5 Sensing Mechanism 34
4.6 Dielectric Loss Function and Quality Factor 35

5 Material Modeling **38**
5.1 Plasmonic Material Modelling 38
5.1.1 The Drude Model 39
5.1.2 The Lorentz Model 40
5.1.3 The Lorentz–Drude Model 41
5.2 Materials 42
5.2.1 Silver (Ag): Characteristics and Modeling 43
5.2.2 Air : Characteristics and Modeling 44

6 Simulation Modeling **45**
6.1 Finite Element Method 45
6.2 Finite-Difference Time-Domain Method 46
6.2.1 Maxwell's Time-Domain Equations 46
6.2.2 The Yee Grid 47
6.2.3 The Leapfrog Scheme 48
6.2.4 Stability Condition 48

6.2.5 FDTD Formulation . . . 49
6.2.5.1 Auxiliary Differential Equation (ADE) Technique . . . 50
6.2.5.2 Z-Transform Technique . . . 50
6.2.5.3 Recursive Convolution (RC) Techniques . . . 51
6.2.6 FDTD Softwares . . . 53
6.2.7 Boundary Conditions in Ansys Lumerical FDTD . . . 54
6.2.8 Sources in Ansys Lumerical FDTD . . . 56
6.2.9 Monitors in Ansys Lumerical FDTD . . . 58

7 Performance Metrics 60
7.1 Transmittance . . . 60
7.2 Reflectance . . . 60
7.3 Slater's Law . . . 60
7.4 Sensitivity . . . 62
7.5 Full Width at Half Maximum (FWHM) . . . 62
7.6 Figure of Merit (FOM) . . . 63
7.7 Quality Factor . . . 63
7.8 Use of Performance Metrics in This Research . . . 64

8 Inverse Design 65
8.1 Workflow . . . 65
8.1.1 Problem Setup and Target Definition . . . 65
8.1.2 Design Domain Parameterization . . . 66
8.1.3 Forward Simulation Model . . . 66
8.1.4 Objective Function Formulation . . . 66
8.1.5 Gradient Evaluation (Adjoint or Direct) . . . 66
8.1.6 Design Update and Optimization Loop . . . 67
8.2 Types of Inverse Design . . . 67

9 Reinforcement Learning 69
9.1 Key Components of Reinforcement Learning . . . 69
9.2 Markov Decision Process (MDP) . . . 71
9.3 Q-Learning . . . 72
9.4 Policy Learning . . . 73

9.5 Applying RL in Inverse Design for Plasmonic Sensors 73
9.5.1 Mapping RL Concepts to the Plasmonic Inverse Design 74
9.5.2 RL Pipeline in Plasmonic Inverse Design 75
9.6 RL Framework for Plasmonic Sensor Optimization 76

10 Re-simulation Results 78
10.1 Resimulation in COMSOL Multiphysics 78
10.1.1 Rahad *et al.* Sensor 78
10.1.2 Al Mahmud *et al.* Sensor 80
10.2 Resimulation in Lumerical FDTD 83
10.2.1 Al Mahmud *et al.* Sensor 83
10.2.2 Automation and Scripting in Lumerical FDTD 84

11 Optimization Results 87
11.1 Optimization Based on Sensitivity 87
11.2 Optimization Based on Sensitivity and FOM 90

12 Demonstration of Outcome Based Education (OBE) 93
12.1 Introduction 93
12.2 Course Outcomes (COs) Addressed 94
12.3 Aspects of Program Outcomes (POs) Addressed 95
12.4 Knowledge Profiles (K3 – K8) Addressed 96
12.5 Use of Complex Engineering Problems 97
12.6 Socio-Cultural, Environmental, and Ethical Impact 97
12.7 Attributes of Ranges of Complex Engineering Problem Solving (P1–P7) Addressed 98
12.8 Attributes of Ranges of Complex Engineering Activities (A1–A5) Addressed 99

13 Conclusions 100
13.1 Future Work 101
13.2 Limitations 101

References 103

List of Figures

1.1 Schematic of an MIM Waveguide [1] 2
1.2 Schematic of Inverse design approach [2] 4

6.1 Yee Grid.[87] 48
6.2 Narrow Source Width 58
6.3 Wider Source Width 58

9.1 Q-Learning Framework 72
9.2 Policy-Learning Framework 73
9.3 Mapping RL to Plasmonic Sensor Design 75
9.4 Flowchart of Python and Lumerical integration 76

10.1 Proposed rectangular ring resonator structure by Rahad *et al.* [30] . . . 79
10.2 Original result obtained by Rahad *et al.* [30] 79
10.3 Electric field distribution of the recreated rectangular ring resonator structure in COMSOL Multiphysics. 80
10.4 Transmittance versus wavelength spectrum obtained from COMSOL resimulation of the Rahad *et al.* sensor. 80
10.5 Proposed Pentagonal ring resonator sensor by Al Mahmud *et al.* [25] . 81
10.6 Original result obtained by Al Mahmud *et al.* [25] 81
10.7 Electric field distribution of the recreated pentagonal ring resonator structure in COMSOL Multiphysics. 82
10.8 Transmittance versus wavelength spectrum obtained from COMSOL resimulation of the Al Mahmud *et al.* sensor. 82
10.9 3D structure of the pentagonal ring resonator sensor modeled in Lumerical FDTD. 83
10.10 Transmittance–wavelength spectrum obtained from the resimulation of the Al Mahmud *et al.* structure in Lumerical FDTD. 84

11.1 Sensitivity improvement trend during RL based optimization of the pentagonal ring resonator. 88

11.2 Sensitivity improvement trend during RL based optimization of the pentagonal ring resonator with nanorod. 89
11.3 Sensitivity improvement trend during RL based optimization of the pentagonal ring resonator with nanorod and variable polygonal sides. . 90
11.4 Sensitivity and figure of merit (FOM) improvement trend during early optimization episodes (1–12). 91
11.5 Sensitivity and figure of merit (FOM) progression during later optimization episodes (59–63). 91

List of Tables

2.1 Summary of Comparative Sensing Metrics Across Geometries. 12

10.1 Structures created in Lumerical FDTD by varying number of sides and nanorods. 85

11.1 Optimization result for pentagonal ring resonator. 87

11.2 Optimization result for pentagonal ring resonator with nanorod. 88

11.3 Optimization result for pentagonal ring resonator with taking number of sides also as a tunable parameter. 89

11.4 Optimization result for pentagonal ring resonator with taking number of sides also as a tunable parameter (two-stage comparison). 92

12.1 Summary of Course Outcomes (COs) Addressed 94

12.2 Summary of Aspects of Program Outcomes (POs) Addressed 95

12.3 Summary of Knowledge Profiles (K3–K8) Addressed 96

12.4 Justification of Knowledge Profiles (K3–K8) Addressed 96

12.5 Summary of Attributes of Ranges of CE Problem Solving (P1–P7) Addressed 98

12.6 Justification of Attributes of Ranges of CE Problem Solving (P1–P7) Addressed 98

12.7 Summary of Attributes of Ranges of CE Activities (A1–A5) Addressed 99

12.8 Justification of Attributes of Ranges of CE Activities (A1–A5) Addressed 99

List of Abbreviations

ADE	Auxiliary Differential Equation
AI	Artificial Intelligence
BC	Boundary Condition
CNN	Convolutional Neural Network
DL	Deep Learning
DQN	Deep Q-Network
FDTD	Finite-Difference Time-Domain
FEM	Finite Element Method
FOM	Figure of Merit
FWHM	Full Width at Half Maximum
GSP	Gap Surface Plasmon
MDP	Markov Decision Process
MIM	Metal–Insulator–Metal
NN	Neural Network
PDE	Partial Differential Equation
PML	Perfectly Matched Layer
Q-Factor	Quality Factor
RI	Refractive Index
RL	Reinforcement Learning
SPP	Surface Plasmon Polariton
SPR	Surface Plasmon Resonance
TE	Transverse Electric
TEM	Transverse Electromagnetic
TM	Transverse Magnetic

Abstract

This research presents a reinforcement learning (RL)–based inverse design framework developed to enhance the performance of plasmonic refractive index nanosensors by optimizing their geometric and topological parameters. Plasmonic refractive index sensors operate by exploiting the interaction between light and the metal–insulator interface, where surface plasmon polaritons (SPPs) enable highly sensitive, label-free detection of refractive index variations in the surrounding medium. In this work, the inverse design framework was implemented using the Lumerical scripting language integrated with Python, enabling automated, iterative refinement of sensor geometry toward predefined targets of sensitivity and figure of merit (FOM). The optimization process employed a Deep Q-Network (DQN)–based reinforcement learning algorithm, wherein the agent dynamically adjusted key design parameters such as resonator radius, width, thickness, and nanorod dimensions. Beginning with a pentagonal ring resonator and an initial target sensitivity of 2000 nm/RIU, the RL agent progressively evolved the geometry into an octagonal configuration. Upon incorporating FOM into the reward function, the optimized design achieved a sensitivity of 2638.15 nm/RIU and an FOM of 10.71 RIU^{-1}. The results demonstrate that coupling reinforcement learning with plasmonic inverse design significantly accelerates the discovery of high-performance sensor geometries, outperforming conventional manual and brute-force optimization methods, and highlight the potential of RL-driven optimization as a transformative approach for the intelligent design of plasmonic sensors with enhanced sensitivity, compactness, and operational efficiency.

Chapter 1

Introduction

Plasmonics manipulates light at the nanoscale level by exploiting the interaction between electromagnetic waves and free electrons at metal–dielectric interfaces. Among various configurations, the **Metal–Insulator–Metal (MIM) resonator** structure has gained significant attention due to its strong field confinement, compact size, and tunable resonance characteristics, making it highly suitable for **refractive index sensing** applications. In recent years, the traditional forward design of plasmonic structures has been complemented by **inverse design** methodologies, where desired optical responses are used to automatically generate the optimal geometrical configurations. **Reinforcement Learning (RL)** and other deep learning techniques have further advanced this approach by enabling the autonomous optimization of complex plasmonic geometries toward enhanced sensitivity and performance.

1.1 Plasmonics

Plasmonics is a rapidly evolving field that investigates how electromagnetic waves interact with the collective oscillations of free electrons at metal–dielectric interfaces. When light strikes a metal surface, the oscillating electric field of the incident wave can induce coherent motion of conduction electrons. These coupled oscillations, known as **surface plasmons**, enable the confinement and manipulation of light at spatial scales much smaller than its wavelength. This unique ability to bridge photonics and electronics opens pathways toward highly compact and efficient optical components. The electromagnetic behavior of surface plasmons can be described using Maxwell's equations, from which a characteristic **dispersion relation** is derived. For a planar metal–dielectric interface, this relation links the surface plasmon polariton (SPP) wave vector to the permittivities of the metal and the dielectric. The wave is bound to the interface, with an evanescent decay on both sides, allowing extremely tight field localization. The metal's response to an optical field is typically characterized using the **Drude model**, which expresses its frequency-dependent permittivity in terms of plasma frequency and damping constant. This model captures the fundamental physics governing the excitation and propagation of SPPs and explains why metals such as silver and gold are widely used in plasmonic applications due to their low loss and negative real permittivity at optical frequencies. A key outcome of this interaction is the formation of localized electromagnetic "hot spots" where the electric field intensity is greatly enhanced. The stored electromagnetic energy in these confined regions determines the structure's overall optical response and plays a critical role in sensing, light guiding, and energy conversion processes. Even a small change in the refractive index of the surrounding medium can significantly alter the resonance condition, forming the basis of plasmonic refractive index sensors.

1.1.1 Metal–Insulator–Metal (MIM) Resonator

The **Metal–Insulator–Metal (MIM)** resonator is one of the most fundamental and widely utilized configurations in plasmonic device design due to its ability to support highly confined surface plasmon modes within a nanoscale dielectric gap. Structurally, it consists of a thin dielectric layer sandwiched between two metallic regions. When light propagates through such a waveguide, the electromagnetic field is tightly confined within the insulator layer while coupling with surface plasmons at both metal–dielectric interfaces. This dual-interface coupling leads to a strongly localized electromagnetic mode known as the **gap surface plasmon (GSP)** mode.

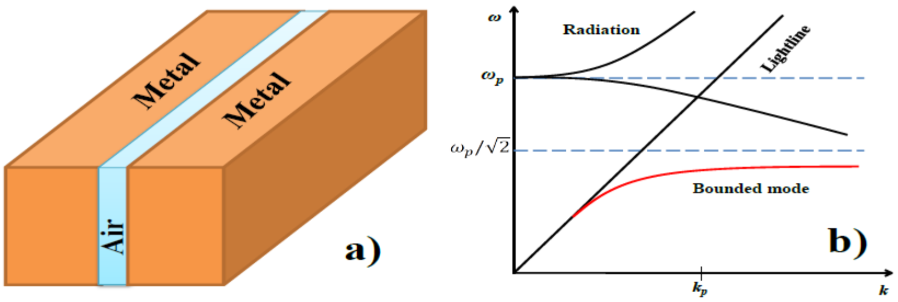

Fig 1.1: Schematic of an MIM Waveguide [1]

The dispersion behavior of the MIM structure is governed by the continuity of electromagnetic field components across the metal–dielectric interfaces. Solving Maxwell's equations for this geometry yields a characteristic mode equation that determines the propagation constant of the guided plasmonic mode. The existence of both symmetric and antisymmetric field distributions allows multiple resonant modes to be supported, depending on the thickness of the dielectric layer and the optical properties of the constituent materials. In a typical MIM waveguide, the confinement of light increases as the insulator thickness decreases, leading to enhanced field localization and stronger light–matter interaction. However, this improvement in confinement is accompanied by higher propagation loss due to absorption in the metallic regions. Therefore, the design of an MIM resonator involves a trade–off between field confinement and propagation length, which directly influences the device's sensitivity and overall performance.

1.2 Inverse Design

The conventional design approach in photonics, often referred to as the forward design method, relies on manually selecting geometrical parameters, simulating their optical response, and iteratively adjusting the structure until the desired behavior is achieved. While effective for simple systems, this process becomes highly inefficient and computationally expensive for complex plasmonic structures with multiple degrees of freedom. The parameter space grows exponentially with the number of design variables, making exhaustive search or manual optimization practically infeasible. To overcome these limitations, the concept of **inverse design** has emerged as a powerful paradigm that reverses the traditional design flow. Instead of starting from geometry and predicting the optical response, inverse design begins with a specified target response such as a particular resonance wavelength, bandwidth, or sensitivity and automatically determines the optimal geometry that can produce it. This approach leverages computational optimization techniques to explore a vast design space in a systematic and data-driven manner.

Mathematically, the inverse design problem can be expressed as an optimization process where the design variables, such as shape, size, or material distribution, are iteratively updated. In the context of plasmonics, inverse design provides an efficient

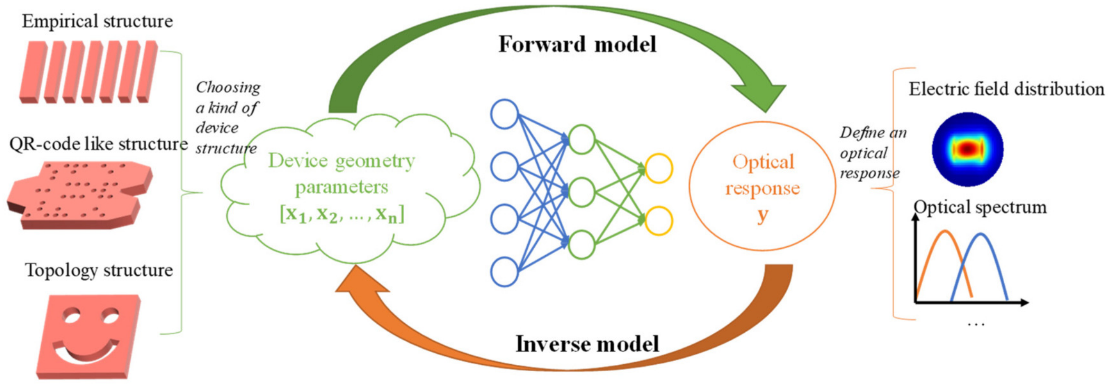

Fig 1.2: Schematic of Inverse design approach [2]

route to develop resonators, waveguides, and metamaterials with tailored spectral and field–confinement characteristics. It allows the creation of unconventional geometries that are difficult to conceive through intuition alone, thereby pushing the limits of performance metrics such as sensitivity, FWHM, and FOM. Furthermore, integrating inverse design with machine learning and deep reinforcement learning has opened new directions for achieving fully autonomous design workflows capable of adapting and learning from prior simulations.

1.2.1 Reinforcement Learning

Reinforcement Learning (RL) represents a data driven optimization framework that enables autonomous decision making through interaction with an environment. In the context of inverse design, RL provides a mechanism for exploring high dimensional design spaces where analytical gradients are difficult to compute or where system responses are governed by complex electromagnetic interactions. Instead of relying on deterministic update rules, RL employs a reward based learning strategy to guide the optimization process toward desirable outcomes. Mathematically, the RL process can be formulated as a **Markov Decision Process (MDP)** where the learning goal is to approximate a value function or Q–function, which estimates the expected reward for each state–action pair for employing deep neural networks to model Q–functions, forming the basis of algorithms such as Deep Q–Networks (DQN) and their variants. When applied to plasmonic sensor design, reinforcement learning enables the optimization of structural parameters with parameter sweeps. The agent progressively learns to balance trade-offs between sensitivity, bandwidth, and loss, converging toward configurations that satisfy target optical responses. This approach significantly reduces computational cost while improving design efficiency.

1.3 Thesis Objective

The primary objective of this thesis is to design, simulate, and optimize plasmonic refractive index sensors through an inverse design approach integrated with reinforcement learning (RL). The research focuses on enhancing the performance of Metal–Insulator–Metal (MIM) sensors by improving their sensitivity, figure of merit (FOM). To achieve these goals, the study implements a computational framework that combines Ansys Lumerical FDTD simulations with Python-based optimization algorithms. The framework automates geometry modification and electromagnetic analysis to iteratively refine sensor structures toward a target performance metric.

The specific objectives of the thesis are as follows:

1. **Study of Plasmonic Materials:** Model the optical response of conventional plasmonic metals such as silver (Ag) using Drude and Lorentz–Drude formulations, ensuring accurate dispersion and absorption representation across the visible–near-IR spectrum.

2. **Development of Structural Geometries:** Design and simulate polygonal MIM resonators—including pentagonal, octagonal, and trapezoidal structures—with integrated nanorods to improve resonance confinement and field coupling.

3. **Mathematical and Computational Modeling:** Apply analytical and numerical electromagnetic modeling through FDTD methods to study mode propagation, spectral response, and boundary behavior.

4. **Implementation of Inverse Design:** Integrate reinforcement learning within the simulation workflow to automate geometry optimization.

5. **Adaptive Optimization:** Replace traditional manual tuning with an adaptive reward-based optimization system.

6. **Performance Evaluation:** Quantitatively assess optimized sensors based on

sensitivity (nm/RIU) and FOM (RIU^{-1}), ensuring robust validation of results.

1.4 Thesis Layout

The thesis is structured into **thirteen chapters**, each addressing a distinct aspect of the research, from theoretical background to reinforcement learning–based optimization and outcome-based analysis.

Chapter 1 provides an overview of plasmonic refractive index sensors, their significance in plasmonics, and the motivation for applying inverse design and reinforcement learning to improve sensitivity and performance.

Chapter 2 summarizes previous research on MIM-based plasmonic sensors, optimization techniques, and machine-learning-based inverse design approaches, highlighting research gaps addressed in this work.

Chapter 3 provides the fundamental physics of electromagnetic wave theory, including Maxwell's equations, Faraday's law, Gauss's law, and the derivation of the electromagnetic wave equation. It also discusses the propagation characteristics of Transverse Electric (TE) and Transverse Magnetic (TM) modes, forming the theoretical foundation for plasmonic waveguide and resonator analysis.

Chapter 4 covers the theory of surface plasmon polaritons (SPPs), metal–dielectric interfaces, dispersion relations, propagation and decay characteristics, and the fundamental principles governing light–matter interactions in plasmonic systems.

Chapter 5 describes the Drude, Lorentz, and Lorentz–Drude models used to represent material dispersion and absorption. Silver (Ag) and air are considered as the metallic substrate and waveguide materials, respectively, forming the basis of the MIM sensor design.

Chapter 6 explains the implementation of FDTD simulation, including the Yee grid, leapfrog scheme, stability condition, dispersive ADE/Z-transform/RC techniques, and the setup of sources, monitors, and boundary conditions in Ansys Lumerical FDTD.

Chapter 7 defines the quantitative performance measures used in various plasmonic research for example Transmittance, Reflectance, Sensitivity, FWHM, FOM, and Q-factor and describes their role in evaluating plasmonic sensor performance.

Chapter 8 details the inverse design workflow, including parameterization, forward simulation, objective formulation, gradient computation, and design iteration. It also categorizes shape-based, topology-based, heuristic, and machine-learning-driven approaches.

Chapter 9 introduces the theoretical foundation of RL, including the Markov Decision Process (MDP), Q-learning, and policy-based learning, followed by their mapping to plasmonic inverse design. The proposed RL optimization framework for MIM sensors is formulated here.

Chapter 10 presents the COMSOL FEM and Lumerical FDTD re-simulation of previously published designs to validate baseline performance and confirm the accuracy of the implemented simulation environment.

Chapter 11 presents the RL-based optimization outcomes, illustrating progressive improvement in sensitivity through multi-stage training. The process begins with a basic pentagonal resonator, evolves into an octagonal geometry with integrated nanorods, and finally incorporates both sensitivity and FOM in the reward function for enhanced optimization performance.

Chapter 12 demonstrates Outcome-Based Education (OBE) which maps the project activities and results to Course Outcomes (COs), Program Outcomes (POs), and Knowledge Profiles (K3–K8), demonstrating alignment with IUT OBE standards and the attributes of complex engineering problem solving.

Chapter 13 summarizes the major findings of the RL-based inverse design approach, discusses the observed performance improvements, and outlines future research directions.

Chapter 2

Literature Review

Plasmonic refractive index sensors are used in biosensing, clinical diagnostics, chemical and environmental monitoring, and integrated optical communication, owing to strong metal-dielectric field confinement and pronounced sensitivity to local index changes. Recent surveys map these applications across visible and infrared bands and track materials and geometries spanning planar films, waveguides, fibers, and metamaterial platforms [3–7]. These works also outline practical considerations such as stability, fabrication compatibility, and surface functionalization strategies that enable selective detection in real samples.

Within this landscape, metal-insulator-metal waveguides are prominent because they support deep subwavelength guiding, compact cavities, and convenient tuning via stubs, slots, and ring-based configurations. Focused studies and broader overviews show how small geometric adjustments can reshape resonance behavior and coupling, enabling compact layouts that integrate with planar fabrication and on-chip routing [1, 8–10]. MIM platforms are further valued for straightforward interfacing with input and output ports, which simplifies device packaging and readout.

Despite these advances, most design workflows still rely on manual parameter sweeps and heuristic iteration. Authoritative reviews in nanophotonics argue that such trial-and-error explores only a narrow region of the feasible space and that algorithmic inverse design can reveal non-intuitive solutions more efficiently [11]. As dimensionality grows, the cost of exhaustive scans increases rapidly and interactions among variables can conceal viable operating points that intuition alone may overlook.

Machine learning offers practical remedies. Deep learning surrogates speed up forward prediction and enable approximate inverse mapping between structure and spectrum, while reinforcement learning introduces autonomous, objective-driven search that operates simulation-in-the-loop or experiment-in-the-loop. Demonstrations across photonic components indicate that data-driven strategies can navigate large design spaces and discover workable geometries with reduced human intervention [12–16].

Guided by these insights, the literature in this thesis is organized into two strands:

1. Literature on Plasmonic Refractive-Index MIM Sensors

2. Literature on Deep-Learning-Based Inverse Design in Plasmonics

Through this literature, we will map application areas, quantify reported performance and methods, and identify the precise research gap that motivates reinforcement-learning-based inverse design for MIM refractive index sensors.

2.1 Literature on Plasmonic Refractive-Index MIM Sensors

Plasmonic refractive index sensing has matured into a rigorous competition in which sensors are judged primarily by two metrics: sensitivity and figure of merit (FOM). In 2017, Yan *et al.* presented a plasmonic configuration based on a metal–insulator–metal (MIM) waveguide integrated with a ring cavity containing a lateral groove and connecting stub, which achieved a sensitivity of 1071.4 nm/RIU and a figure of merit (FOM) of 14.29 RIU^{-1} [17]. One year later, Zhang *et al.* developed a compact dual-ring sensor exhibiting sharp spectral resonances, reporting a sensitivity of 1060 nm/RIU with an FOM of 203.8 RIU^{-1} [18]. In 2019, Wang *et al.* designed a resonator with sector-shaped slits and internal barriers, attaining a performance of 1114.3 nm/RIU and an FOM of 55.71 RIU^{-1} [19]. The momentum continued in 2020, as Chou Chao *et al.* showed that embedding nanorods within a plasmonic ring enhances tunability, yielding 2080 nm/RIU and 29.92 RIU^{-1} [20]. In the same period, Hasan *et al.* presented a rectangular MIM sensor delivering 886.16 nm/RIU, while Sagor *et al.* realised a three-cavity design with quadrilateral resonators placed perpendicularly between MIM waveguides, attaining 1556 nm/RIU and 14.83 RIU^{-1} [21, 22]. In a subsequent refinement, Sagor *et al.* optimized two unequal vertical rectangular cavities and pushed the sensitivity to 2625.87 nm/RIU with an

FOM of 26.04 RIU^{-1} [23]. Collectively, these studies demonstrate how disciplined cavity engineering converts minute refractive-index variations into decisive spectral shifts, with early demonstrations already extending to blood analysis and temperature sensing.

Building upon these benchmark results, several notable plasmonic sensor designs were subsequently reported. Al Mahmud *et al.* developed a triangular-ring resonator that achieved a sensitivity of 2713 nm/RIU and a figure of merit (FOM) of 35.1 RIU^{-1}, while in a complementary study, their pentagonal ring configuration produced 2325 nm/RIU with an FOM of 46 RIU^{-1} [24, 25]. Rashid *et al.* presented a configuration consisting of three circular cavities linked to a linear metal–insulator–metal (MIM) waveguide, demonstrating 3573.3 nm/RIU with an FOM of 21.9 RIU^{-1} and highlighting its suitability for gaseous analyte sensing and label-free biochemical detection [26]. Faruque *et al.* revealed that highly doped silicon behaves optically similar to metallic plasmonic media, achieving a peak sensitivity of 4900 nm/RIU—surpassing the performance of most conventional MIM architectures [27]. Furthermore, Tathfif *et al.* designed a triple concentric ring resonator embedded in a metal–insulator–metal guide, obtaining 3639.79 nm/RIU for gas detection. Upon optimization, the same CTRR design reached 7530.49 nm/RIU within a refractive-index range of 1.30–1.40 and demonstrated additional capability as a miniaturized optical filtering structure [28].

Research momentum has continued to build, with several architectures achieving record performance and demonstrating strong application readiness. Rakib *et al.* presented a hexagonal plasmonic sensor within a metal–dielectric–metal (MDM) configuration that offered precise spectral control and achieved a sensitivity of 4571.7 nm/RIU with an FOM of 63.3 RIU^{-1} [29]. Rahad *et al.* developed a biomedical-oriented sensing platform designed for early diagnostic use; by exploiting the correlation between refractive index variation and resonance displacement, the device successfully identified multiple blood-related biomolecules associated with glucose regulation and anaemia. Using finite element analysis, the sensor achieved 2963.73 nm/RIU sensitivity, an FOM of 25.1 RIU^{-1}, and a resolution of 3.37×10^{-7} RIU [30]. In a complementary materials study, Rakib *et al.* introduced a comb-shaped ZrN–insulator–ZrN layout optimized for CMOS compatibility, which achieved 1445.46 nm/RIU and an FOM of 140.96 RIU^{-1}—outperforming conventional noble-metal MIM designs [31]. Haque *et al.* proposed an octagonal cavity enclosed within a square resonator, enhanced through silver nanodots and paired slits connected to a linear waveguide. The resulting device reached 2527.6 nm/RIU with an FOM of 16.24 RIU^{-1} and was experimentally validated for honey-quality assessment and lactose quantification [32]. Shafagh *et al.* engineered an asymmetric hexagonal nanoring tailored for oncological diagnostics, where adjustment of the cavity angle produced approximately 1800 nm/RIU with an FOM of 90.4 RIU^{-1} [33].

Building upon these advances, several works pushed toward multi-channel interrogation and clinically significant detection limits. Rahad *et al.* implemented an integrated lab-on-chip system containing a 1×2 demultiplexer that enabled simultaneous dual-sample analysis without cross-contamination. Optimized splitter and coupler parameters resulted in 865.9 nm/RIU sensitivity and an FOM of 58.4 RIU^{-1} [34]. Kabir *et al.* reported a similar biochip on a silicon–insulator–silicon framework capable of detecting refractive index variations for two analytes within a shared footprint, achieving 1273.5788 nm/RIU with a detection limit of 7.85×10^{-7} RIU [35]. Khodaie *et al.* focused on brain-cancer discrimination using multimode split-ring resonators, where the first mode exhibited 1778.3 nm/RIU sensitivity, a detection limit of 0.016 RIU, an FOM of 7 RIU^{-1}, and a quality factor of 11.7 [36]. Faraji *et al.* designed eight cube-shaped resonant cells connected by a compliant interface, supporting multimodal operation suitable for differentiating between healthy and malignant tissue. The first and second resonant modes achieved 604 nm/RIU (FOM 14.72 RIU^{-1}) and 1097.1 nm/RIU (FOM 15.64 RIU^{-1}), respectively [37]. In infectious-disease detection, Butt *et al.* conducted a computational study of a tuberculosis biosensor built on an MIM platform integrated with two Si_3N_4 mode converters for efficient free-space coupling. The optimized configuration attained approximately 900 nm/RIU with an FOM of 11.84 RIU^{-1}, demonstrating the feasibility of co-designing coupling networks with the sensing element [38].

Table 2.1 consolidates sensitivities, FOMs, and geometries across the cited studies. Most analyses employed the finite element method, with fewer adopting FDTD. The majority of MIM works model two-dimensional cross-sections and assume that, for sufficiently tall structures, two-dimensional behaviour approximates three-dimensional responses, following the rationale discussed by Danaie and collaborators [39]. Across the board, geometry selection and parameter tuning were guided by human intuition, exhaustive or semi-exhaustive sweeps, and incremental edits to gaps, widths, and cavity features. While such workflows can be effective, they rely heavily on trial-and-error and are inherently myopic and inefficient in high-dimensional design spaces. This observation motivates data-driven inverse design, where deep learning and reinforcement learning can traverse larger design spaces efficiently and reveal non-intuitive optima for plasmonic refractive index sensors.

Table 2.1: Summary of Comparative Sensing Metrics Across Geometries.

Sensor Structure	**Sensitivity (nm/RIU)**	**FOM ($\mathbf{RIU^{-1}}$)**	**Src.**
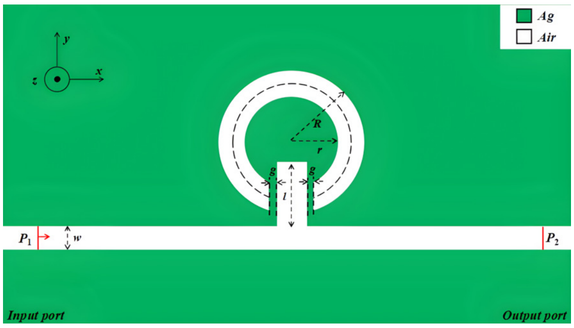	1071.40	14.29	[17]
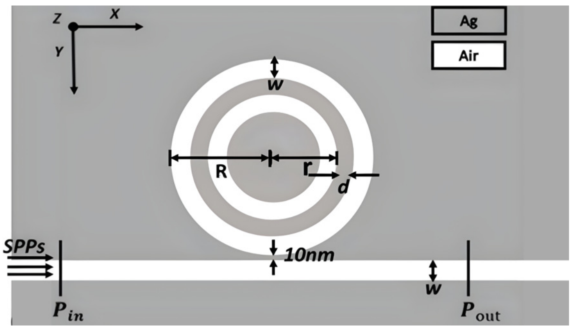	1060.00	203.8	[18]
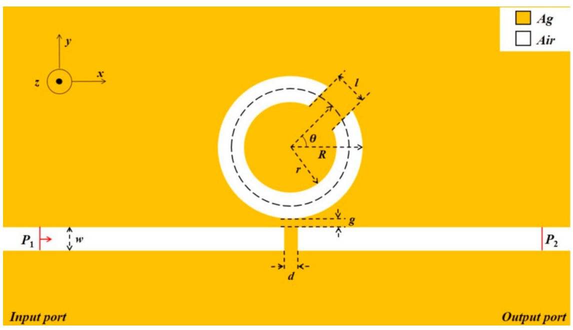	1114.30	55.71	[19]

Continued on next page

Sensor Structure	**Sensitivity (nm/RIU)**	**FOM ($\mathbf{RIU^{-1}}$)**	**Src.**
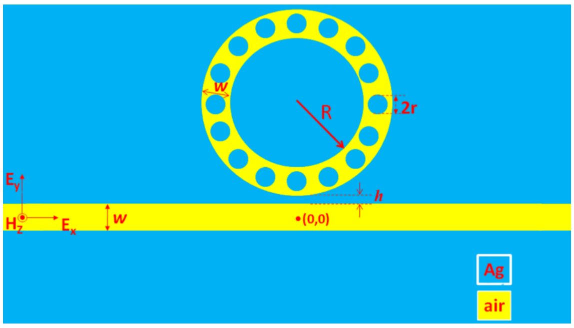	2080.00	29.92	[20]
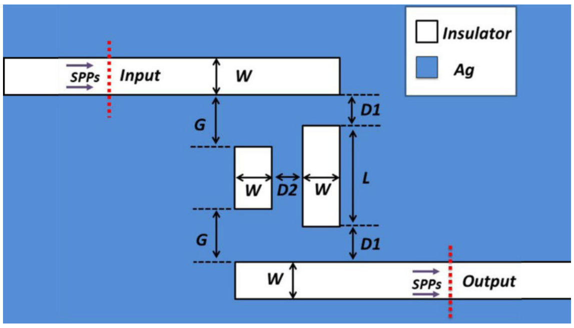	2625.87	26.04	[23]
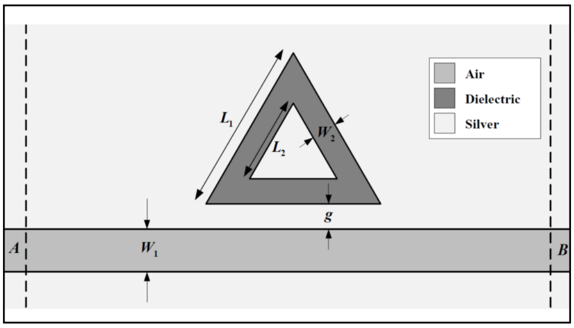	2713.00	35.10	[24]
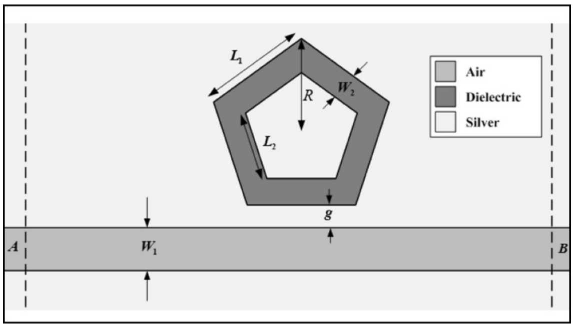	2325.00	46.00	[25]
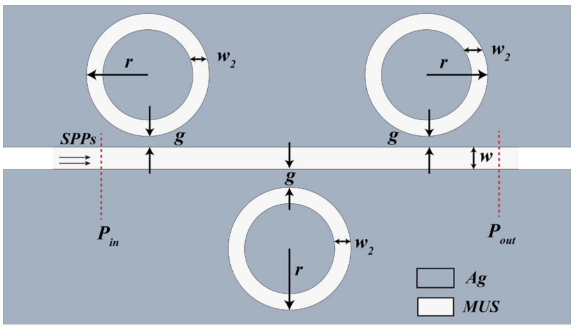	3573.30	21.90	[26]

Continued on next page

Sensor Structure	Sensitivity (nm/RIU)	FOM (RIU^{-1})	Src.
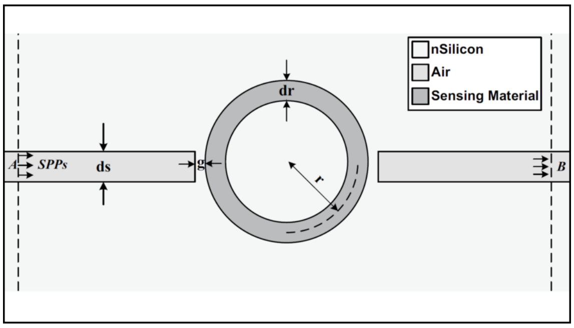	4900.00	N/A	[27]
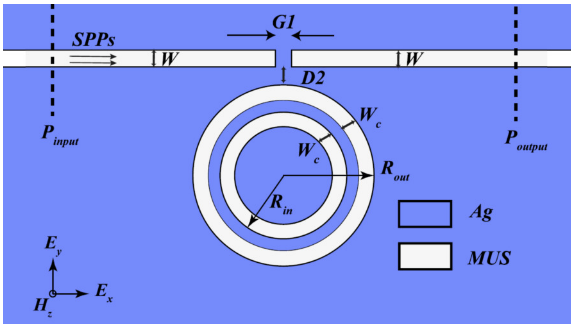	3639.79	91.02	[28]
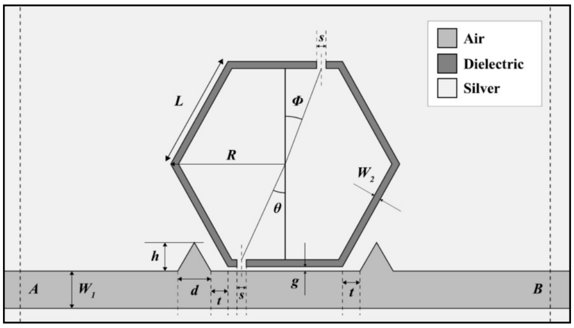	4571.70	63.30	[29]
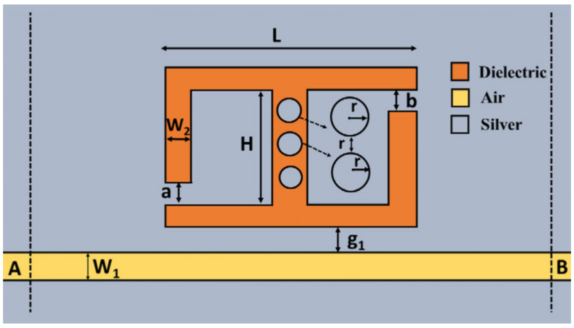	2963.73	25.10	[30]
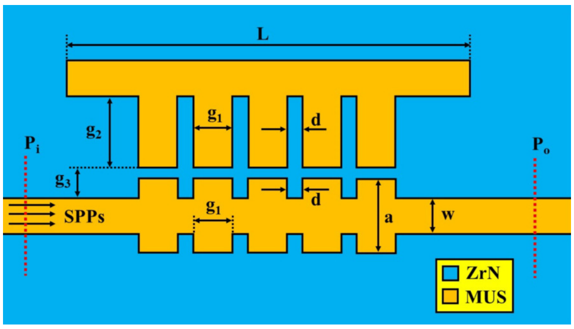	1445.46	140.96	[31]

Continued on next page

Sensor Structure	Sensitivity (nm/RIU)	FOM (RIU^{-1})	Src.
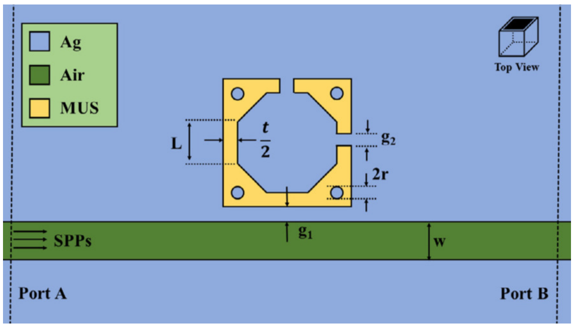	2527.60	16.24	[32]
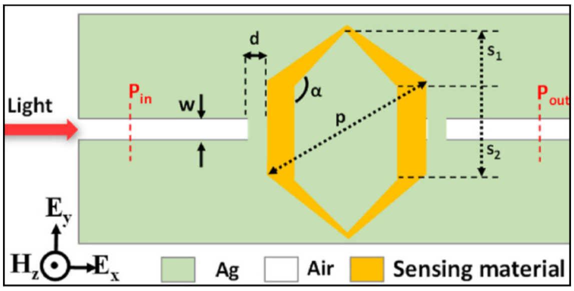	1800.00	90.40	[33]
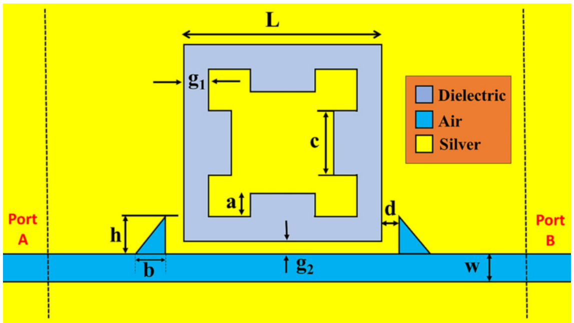	3270.30	31.15	[40]

2.2 Literature on Deep-Learning-Based Inverse Design in Plasmonics

Machine learning, particularly deep learning, has moved from exploratory promise to core engineering infrastructure, enabling rapid progress across molecular design, algorithm discovery, semiconductor design, materials exploration, high-fidelity forecasting, and general-purpose language technologies. These advances follow a pattern that motivates inverse design in engineering: learn reliable surrogates for expensive simulations, explore large design spaces efficiently, and optimize multiple objectives under practical constraints [41–48]. Building on this momentum, the inverse design starts with a performance target and, through targeted searches often accelerated by learned surrogates and generative or reinforcement learning optimizers, identifies materials, geometries, and process parameters that meet the specification [49, 50].

In this context, early computational intelligence efforts in plasmonics set the stage for learning-based workflows. Bahrami *et al.* used a genetic algorithm to tune surface-plasmon and plasmon-waveguide resonance sensors for bulk detection, improving performance without exhaustive manual scans [51]. In parallel, Lalau-Keraly *et al.* introduced adjoint shape optimization for electromagnetics, a gradient method that cuts computation and underpins many inverse design tools [52–55]. Lu and Vučković proposed full-space exploration for linear nanophotonic devices, and Piggott *et al.* used an inverse-design pipeline to realize a compact broadband on-chip demultiplexer [56, 57]. In instrumentation, Ballard *et al.* developed a learning-based framework for low-cost mobile multispectral plasmonic readers [58]. As deep learning entered the field, Li *et al.* showed that neural networks learn accurate geometry-to-spectrum maps from modest data and enable instant prediction for large candidate pools [59]. Zhang *et al.* trained networks on Monte-Carlo samples of waveguide-coupled cavities to perform spectrum prediction, parameter fitting, inverse design, and optimization with close agreement to full-wave solvers [60].

Among recent advances in deep-learning-based optimization, Adibnia *et al.* introduced a neural framework for empirical spectral prediction and inverse design of all-optical nonlinear plasmonic ring-resonator switches: the learned forward model reproduces FDTD-level spectra at far lower cost, and the inverse model retrieves geometries for target responses [61]. To address data demands, follow-on work from the same group used the Taguchi method to systematize data acquisition and reduce training burden for switching applications [62, 63].

Focusing on MIM structures, learning-guided optimization and evolutionary search are now embedded in sensor design. Khani *et al.* coupled a MIM bus to U-shaped and inverted U-shaped resonators, training an extreme-randomised-trees regressor to interpolate spectra and reporting 571.4 nm/RIU with an FOM of 14,987 RIU^{-1} [64]. Zonouri *et al.* introduced a four-channel MIM diplexer with sensitivities of 3500, 4250, 3375, and 4003 nm/RIU and FOMs of 113.4–124.7 RIU^{-1}, refined via a multilayer perceptron [65]. Darabi *et al.* optimized a compact MIM filter using particle swarm optimization to maximize sensitivity [66]. Khalilian *et al.* demonstrated a hybrid plasmonic–dielectric biosensor where a MIM bus is coupled to a silicon-core resonator; a genetic algorithm with Lumerical FDTD achieved 1276 nm/RIU and 107 RIU^{-1} [67]. In related work, Zonouri *et al.* used a group-method-of-data-handling network to optimize a rake-shaped MIM resonator, reaching 2587.87 nm/RIU [68]. These studies show that ML models accelerate spectrum prediction and parameter retrieval, and that meta-heuristics navigate high-dimensional geometries; however, data requirements remain heavy, motivating lighter-data strategies such as self-supervised learning and reinforcement learning with simulation in the loop.

Beyond supervised surrogates, reinforcement-learning approaches have begun to shape plasmonic optimization. Hamada *et al.* used deep reinforcement learning to tune a hyperbolic metamaterial absorber; Badloe *et al.* demonstrated learning guided ultra-broadband biomimetic absorbers; and Rosafalco *et al.* maximized energy-harvesting performance in graded metamaterials [69–71]. Xu *et al.* surveyed learning methods for forward simulation and inverse design and argued for more autonomous reinforcement-learning frameworks [72]. Despite this progress, reinforcement learning has been applied mainly to absorbers and energy-harvesting metamaterials; to the best of our knowledge, there are no studies applying reinforcement learning to design or optimize MIM refractive-index sensors, nor closely related MIM components such as logic gates, couplers, or multiplexers. This gap motivates the reinforcement-learning-based inverse design advanced in this thesis.

Chapter 3

Electromagnetic Wave Theory

3.1 Maxwell's Fundamental Equations

Maxwell's equations are the universal laws of classical electromagnetism—from circuits and antennas to nanophotonics and plasmonic sensors. They state, in compact form, how electric and magnetic fields arise from charges and currents, how the two fields are coupled in time, and how electromagnetic energy moves through space and materials. In this thesis, every simulation result is a solution of these equations together with the appropriate material models and boundary conditions. In differential form (SI units),

$$\nabla \times \mathbf{H} = \mathbf{J} + \frac{\partial \mathbf{D}}{\partial t} \tag{3.1}$$

$$\nabla \times \mathbf{E} = -\frac{\partial \mathbf{B}}{\partial t} \tag{3.2}$$

$$\nabla \cdot \mathbf{D} = \rho \tag{3.3}$$

$$\nabla \cdot \mathbf{B} = 0 \tag{3.4}$$

They form a closed description of field–matter interaction. In plasmonics, the material response is dispersive and complex; metals exhibit a negative real permittivity over optical bands. At a metal–dielectric interface, Maxwell's boundary conditions then support surface plasmon polaritons with strong field confinement. In a metal–insulator–metal (MIM) sensor, small changes in the analyte refractive index perturb this dispersion and shift the resonant wavelength that we measure. The finite-difference time-domain (FDTD) formulation discretizes space on a staggered (Yee) grid and advances the time-domain Maxwell equations under consistent boundary conditions, ensuring physical fidelity in the computed fields.

3.1.1 Maxwell–Ampère's Law

Maxwell–Ampère's law extends Ampère's original statement by adding the displacement current, ensuring local charge conservation and enabling electromagnetic wave propagation in dielectrics. In differential form (SI units),

$$\nabla \times \mathbf{H} = \mathbf{J} + \frac{\partial \mathbf{D}}{\partial t} \tag{3.5}$$

where $\mathbf{H}$ is the magnetic field intensity, $\mathbf{J}$ the conduction current density, and $\mathbf{D}$ the electric flux density. The added term $\partial \mathbf{D}/\partial t$ allows "current" to exist even when no charges move through a conductor (e.g., across a capacitor gap), making the theory self-consistent in time-varying fields.

The integral form over a surface S with boundary ∂S is

$$\oint_{\partial S} \mathbf{H} \cdot d\boldsymbol{\ell} = \iint_S \mathbf{J} \cdot d\mathbf{S} + \frac{d}{dt} \iint_S \mathbf{D} \cdot d\mathbf{S}. \tag{3.6}$$

This states that the magnetomotive circulation around a contour equals the sum of conduction current and displacement-current flux through any surface spanning that contour.

In finite-difference time-domain (FDTD) simulations, this law provides the explicit time update for the electric field: the numerical scheme computes $\mathbf{E}^{n+1}$ from spatial differences of $\mathbf{H}^{n+\frac{1}{2}}$ and the current terms, on a staggered (Yee) grid with appropriate boundary conditions. The displacement current term is handled naturally via $\partial \mathbf{D}/\partial t$, ensuring a discrete continuity law and stable coupling between $\mathbf{E}$ and $\mathbf{H}$.

3.1.2 Faraday's Law

Faraday's law describes how time-varying magnetic fields generate electric fields. It is the fundamental statement behind electromagnetic induction and explains induced emf in coils, transformers, and, at the nanoscale, the circulating electric fields that appear near plasmonic resonators. In differential form (SI units),

$$\nabla \times \mathbf{E} = -\frac{\partial \mathbf{B}}{\partial t} \tag{3.7}$$

where $\mathbf{E}$ is the electric field and $\mathbf{B}$ is the magnetic flux density. The negative sign encodes Lenz's law: the induced electric field acts to oppose the change in magnetic flux that created it. The integral form over a surface S with boundary ∂S is

$$\oint_{\partial S} \mathbf{E} \cdot d\boldsymbol{\ell} = -\frac{d}{dt} \iint_S \mathbf{B} \cdot d\mathbf{S}. \tag{3.8}$$

In finite-difference time-domain (FDTD) simulations, Faraday's law provides the explicit time update for the magnetic field. On the staggered (Yee) grid, spatial finite differences of the electric-field components at time step n produce $\partial \mathbf{B}/\partial t$, from which $\mathbf{H}^{n+\frac{1}{2}}$ (or $\mathbf{B}^{n+\frac{1}{2}}$) is advanced. Ampère–Maxwell's law is then used to update $\mathbf{E}$.

3.1.3 Gauss's law For Electric fields

Gauss's law links electric flux to its source-free electric charge. It states that the divergence of the electric flux density $\mathbf{D}$ equals the local free-charge density ρ:

$$\nabla \cdot \mathbf{D} = \rho \tag{3.9}$$

Equivalently, the total electric flux through any closed surface S equals the free charge enclosed in the corresponding volume V:

$$\iint_S \mathbf{D} \cdot d\mathbf{S} = \iiint_V \rho \, dV \tag{3.10}$$

In finite-difference time-domain simulations, Gauss's law acts as a constraint that must remain consistent with the time updates provided by Maxwell–Ampère and Faraday laws.

3.1.4 Gauss's Law for Magnetic Fields

Gauss's law for magnetism states that magnetic flux has no isolated sources or sinks: magnetic field lines form closed loops. In differential form,

$$\nabla \cdot \mathbf{B} = 0 \tag{3.11}$$

which says that the magnetic flux density $\mathbf{B}$ is divergence-free everywhere. The global integral statement over any closed surface S is

$$\iint_S \mathbf{B} \cdot d\mathbf{S} = 0 \tag{3.12}$$

meaning that the net magnetic flux through a closed surface is always zero. Together, these relations encode the absence of magnetic monopoles in classical electromagnetism.

In a finite-difference time-domain discretization, the staggered (Yee) placement of fields and the leap-frog updates from Faraday's law preserve a discrete, divergence-free B provided the initial state and sources are consistent. Perfectly matched layers (PMLs) and dispersive material updates are formulated to maintain this property, ensuring physically correct closed magnetic loops in and around metal–insulator–metal geometries that set the stored energy and spectral response of the sensor.

3.2 Constitutive Equations

Maxwell's equations become a complete physical model only after specifying how a material responds to the fields. These constitutive relations link field intensities $(\mathbf{E}, \mathbf{H})$ to flux densities $(\mathbf{D}, \mathbf{B})$ and to current $\mathbf{J}$, encapsulating linearity, anisotropy, dispersion, and loss.

In a linear, homogeneous, isotropic dielectric, the electric flux density is proportional to the electric field. This defines the material's permittivity and closes the electric side of the model:

$$\mathbf{D} = \epsilon \, \mathbf{E} \tag{3.13}$$

Likewise, the magnetic flux density is proportional to the magnetic field in such media. This introduces the permeability and closes the magnetic side of the model:

$$\mathbf{B} = \mu\,\mathbf{H} \tag{3.14}$$

When charge carriers are present, the material permits conduction. In the simplest form, the current density is proportional to the electric field through the conductivity:

$$\mathbf{J} = \sigma\,\mathbf{E} \tag{3.15}$$

A more general and instructive view separates vacuum response from material polarization and magnetization. This makes explicit how matter stores and reorients dipoles under applied fields:

$$\mathbf{D} = \epsilon_0\,\mathbf{E} + \mathbf{P}, \qquad \mathbf{B} = \mu_0\big(\mathbf{H} + \mathbf{M}\big) \tag{3.16}$$

For weak fields in linear media, polarization and magnetization scale with the driving fields via (possibly tensor) susceptibilities. This form is convenient for anisotropic crystals and engineered media:

$$\mathbf{P} = \epsilon_0\,\boldsymbol{\chi}_e\,\mathbf{E}, \qquad \mathbf{M} = \boldsymbol{\chi}_m\,\mathbf{H} \tag{3.17}$$

Real plasmonic metals and many dielectrics are dispersive: their response depends on past fields. In the time domain this appears as a causal convolution, linking the present flux density to the field history:

$$\mathbf{D}(t) = \epsilon_0\,\mathbf{E}(t) + \int_0^{\infty} \boldsymbol{\chi}_e(\tau)\,\mathbf{E}(t-\tau)\,d\tau \tag{3.18}$$

In metal–insulator–metal sensors, the dispersive, complex $\epsilon(\omega)$ of the metal and the refractive index of the analyte set the modal confinement and resonance. In FDTD, these relations are implemented through auxiliary differential–equation (ADE) or related updates so that $\mathbf{D}$, $\mathbf{E}$, and $\mathbf{J}$ evolve consistently with the material model.

3.3 Electromagnetic Wave Equations

In a source-free, linear, homogeneous, and isotropic medium, Maxwell's equations combine to give second-order wave equations for the electric and magnetic fields (see Eq. 3.19 and Eq. 3.20); these relations state that time-varying fields propagate as waves whose speed is set by the material parameters Eq. 3.21.

$$\nabla^2 \mathbf{E} - \mu\,\epsilon\,\frac{\partial^2 \mathbf{E}}{\partial t^2} = 0 \tag{3.19}$$

$$\nabla^2 \mathbf{H} - \mu\,\epsilon\,\frac{\partial^2 \mathbf{H}}{\partial t^2} = 0 \tag{3.20}$$

$$v = \frac{1}{\sqrt{\mu\,\epsilon}} \tag{3.21}$$

For time-harmonic fields, the same physics appears in the Helmholtz form with a single material parameter k (see Eq. 3.22 and Eq. 3.23); the material dependence is according to Eq. 3.24.

$$\nabla^2 \mathbf{E} + k^2 \mathbf{E} = 0 \tag{3.22}$$

$$\nabla^2 \mathbf{H} + k^2 \mathbf{H} = 0 \tag{3.23}$$

$$k^2 = \omega^2 \mu\,\epsilon \tag{3.24}$$

These relations link material properties (μ, ϵ) to phase, wavelength, and impedance through Eq. 3.24 and Eq. 3.21; they also set how boundaries shape modes and resonances via the field solutions of Eq. 3.22–Eq. 3.23. In practice, the finite–difference time–domain (FDTD) method advances the time–domain Maxwell system whose solutions satisfy the wave Eq. 3.19–Eq. 3.20 (equivalently, the Helmholtz forms

Eq. 3.22–Eq. 3.23), so the simulated propagation and resonance behavior directly reflect the governing physics used.

3.3.1 Electromagnetic Wave Equations—Derivation

In a source-free, linear, homogeneous, isotropic medium with $\mathbf{D} = \epsilon\mathbf{E}$ and $\mathbf{B} = \mu\mathbf{H}$, the time-domain Maxwell pair relates the time variation of one field to the spatial variation of the other.

Now starting from the two first-order relations:

$$\nabla \times \mathbf{E} = -\,\mu\,\frac{\partial \mathbf{H}}{\partial t} \tag{3.25}$$

$$\nabla \times \mathbf{H} = \epsilon\,\frac{\partial \mathbf{E}}{\partial t} \tag{3.26}$$

Then taking the curl of Eq. 3.25 and carrying the time derivative inside:

$$\nabla \times (\nabla \times \mathbf{E}) = -\,\mu\,\frac{\partial}{\partial t}(\nabla \times \mathbf{H}) \tag{3.27}$$

Next substituting Eq. 3.26 into the right-hand side to eliminate $\mathbf{H}$:

$$\nabla \times (\nabla \times \mathbf{E}) = -\,\mu\epsilon\,\frac{\partial^2 \mathbf{E}}{\partial t^2} \tag{3.28}$$

Now using the identity $\nabla \times (\nabla \times \mathbf{E}) = \nabla(\nabla \cdot \mathbf{E}) - \nabla^2\mathbf{E}$ and the source-free condition $\nabla \cdot \mathbf{E} = 0$:

$$\nabla^2\mathbf{E} - \mu\epsilon\,\frac{\partial^2 \mathbf{E}}{\partial t^2} = 0 \tag{3.29}$$

Then, by the same steps applied to $\mathbf{H}$, it is possible to obtain the symmetric result:

$$\nabla^2\mathbf{H} - \mu\epsilon\,\frac{\partial^2 \mathbf{H}}{\partial t^2} = 0 \tag{3.30}$$

Finally, assuming time-harmonic fields $e^{j\omega t}$ to reach the Helmholtz form (with $k^2 = \omega^2\mu\epsilon$, cf. Eq. 3.24):

$$\nabla^2\mathbf{E} + k^2\mathbf{E} = 0, \qquad \nabla^2\mathbf{H} + k^2\mathbf{H} = 0 \tag{3.31}$$

These steps show, in order, how Eq. 3.25–Eq. 3.26 lead directly to the wave Eq. 3.29–Eq. 3.30 and, under harmonic excitation, to the Helmholtz relations Eq. 3.31. The parameters μ and ϵ thus set the propagation, resonance, and energy transport that simulations and measurements rely on.

3.4 Electromagnetic Modes

3.4.1 Transverse Magnetic (TM) Mode

TM modes are defined by a vanishing longitudinal magnetic field and a nonzero longitudinal electric field: $H_x = 0$, $E_x \neq 0$. For a planar metal–dielectric interface (ϵ_m for $z < 0$, ϵ_d for $z > 0$) with propagation along x, guided surface waves decay away from the interface along $\pm z$ and exist when the boundary conditions link the tangential fields consistently. This yields the well-known SPP dispersion:

$$\beta = k_0 \sqrt{\frac{\epsilon_m \, \epsilon_d}{\epsilon_m + \epsilon_d}}, \qquad k_0 = \frac{\omega}{c}. \tag{3.32}$$

Bound solutions require $\operatorname{Re} \epsilon_m < 0$ and $\operatorname{Re}(\epsilon_m) + \epsilon_d < 0$, ensuring evanescent decay into both media. In a metal–insulator–metal (MIM) gap of thickness t, coupling of the two interfaces produces gap plasmons; for the symmetric branch the dispersion satisfies

$$\tanh\left(\frac{k_d t}{2}\right) = -\frac{\epsilon_m \, k_d}{\epsilon_d \, k_m}, \tag{3.33}$$

with

$$k_i = \sqrt{\beta^2 - k_0^2 \epsilon_i}, \qquad i \in \{m, d\}. \tag{3.34}$$

The transverse wave impedance for TM fields is

$$Z_{\text{TM}} = \frac{\beta}{\omega \, \epsilon}. \tag{3.35}$$

These relations explain strong field confinement and the high refractive-index sensitivity exploited in MIM sensors, where changes in ϵ_d shift $\beta(\omega)$ and the resonance wavelength.

3.4.2 Transverse Electric (TE) Mode

TE modes have no longitudinal electric field and a nonzero longitudinal magnetic field: $E_x = 0$, $H_x \neq 0$, with propagation along x. In closed waveguides the axial constant follows

$$\beta^2 = k^2 - k_c^2, \qquad Z_{\mathrm{TE}} = \frac{\omega\mu}{\beta}. \tag{3.36}$$

At a metal–dielectric interface with $\mu_d \approx \mu_m \approx \mu_0$, a surface-bound TE solution is not supported because the TE surface-wave condition

$$\frac{k_{z,d}}{\mu_d} + \frac{k_{z,m}}{\mu_m} = 0 \tag{3.37}$$

cannot be satisfied with both $k_{z,i} > 0$ when μ_d and μ_m share the same positive sign. Consequently, TE polarization does not form plasmonic surface waves in conventional optical materials and does not set the sensing resonances in MIM structures.

3.4.3 Transverse Electromagnetic (TEM) Mode

TEM modes possess neither longitudinal electric nor longitudinal magnetic components: $E_x = 0$, $H_x = 0$, with propagation along x. A true TEM solution requires at least two conductors so that transverse fields satisfy electroquasistatic relations across the cross-section; it has no cutoff and

$$\beta = k, \qquad Z_{\mathrm{TEM}} = \eta = \sqrt{\frac{\mu}{\epsilon}}. \tag{3.38}$$

Single-conductor closed waveguides do not support TEM. In deeply subwavelength gaps, fields may appear quasi-TEM over short distances, yet the resonant, surface-confined waves responsible for MIM refractive-index sensing remain TM-polarized plasmons governed by the dispersive permittivity of the metal.

Chapter 4

Surface Plasmon Resonance

Surface plasmon resonance (SPR) is the excitation of a transverse–magnetic surface wave—the surface plasmon polariton (SPP)—that propagates along a metal–dielectric boundary while decaying evanescently into both media. When the in–plane momentum of incident light matches the SPP propagation constant (via a prism, grating, or embedded waveguide), energy is transferred into the surface mode and a sharp spectral or angular dip appears in the reflected or transmitted signal. The resonance position is governed by the SPP dispersion, which depends on the metal's complex permittivity and the refractive index of the adjacent dielectric. Small changes in this dielectric environment shift the resonance, enabling refractive–index sensing with subwavelength field confinement. The resonance linewidth reflects internal (Ohmic and dielectric) losses and external (radiative/coupling) leakage; together these set the quality factor and detection limit. In the present work, SPR provides the operating principle for metal–insulator–metal resonators, where material choice and gap geometry control dispersion, confinement, and ultimately sensing performance.

4.1 Surface Plasmon Polariton (SPP)

A surface plasmon polariton (SPP) is a transverse–magnetic (TM) electromagnetic wave bound to a single, flat metal–dielectric interface. It propagates along the interface and decays exponentially into both media due to the metal's negative real permittivity at optical frequencies [73].

For a dielectric with permittivity $\varepsilon_d > 0$ and a metal with complex $\varepsilon_m(\omega)$, the longitudinal propagation constant along the interface is

$$\beta = k_0\sqrt{\frac{\varepsilon_m\,\varepsilon_d}{\varepsilon_m + \varepsilon_d}}, \qquad k_0 = \frac{\omega}{c}. \tag{4.1}$$

Eq. 4.1 sets the SPP phase velocity and effective index via $\beta' = \Re\{\beta\}$ and also introduces attenuation through $\beta'' = \Im\{\beta\}$ [73]. A bound mode requires evanescent decay in both media, which is ensured when

$$\Re\{\varepsilon_m\} < -\varepsilon_d. \tag{4.2}$$

The transverse (normal) wavenumbers in the dielectric and metal follow from the Helmholtz relation:

$$k_{z,d} = \sqrt{\beta^2 - \varepsilon_d k_0^2}, \qquad k_{z,m} = \sqrt{\beta^2 - \varepsilon_m k_0^2}. \tag{4.3}$$

The corresponding penetration depths (amplitude $1/e$) are

$$\delta_d = \frac{1}{\Re\{k_{z,d}\}}, \qquad \delta_m = \frac{1}{\Re\{k_{z,m}\}}. \tag{4.4}$$

Together, Eq. 4.3–Eq. 4.4 quantify how tightly the SPP is confined to the interface on each side [73].

Writing $\beta = \beta' + j\beta''$, the amplitude decays as $e^{-2\beta'' x}$ along the interface, giving the propagation length

$$L_p = \frac{1}{2\beta''}. \tag{4.5}$$

Eq. 4.5 links attenuation directly to material loss through β'', which itself is governed by ε''_m in Eq. 4.1 [73].

From Eq. 4.1 and Eq. 4.3: making $|\varepsilon'_m|$ more negative or increasing ε_d raises β' and tightens confinement (smaller δ_d), while larger ε''_m increases β'' and shortens L_p through Eq. 4.5. These trade–offs are the core design levers for single–interface SPPs [73].

4.2 Dispersion Relations

For a single, flat metal–dielectric interface supporting a TM surface wave, the dispersion follows from the electromagnetic boundary conditions. The tangential fields H_y and E_x are continuous at the interface, and the normal displacement $D_z = \varepsilon E_z$ is also continuous in the absence of free surface charge. Eliminating field amplitudes leads to the characteristic condition

$$D_0 \equiv \frac{k_{z,d}}{\varepsilon_d} + \frac{k_{z,m}}{\varepsilon_m} = 0, \tag{4.6}$$

which enforces that the TM field combination required by the boundary conditions is satisfied by a non-trivial surface mode.

The normal (evanescent) wavenumbers are defined by the transverse dispersion in each medium,

$$k_{z,i} = \sqrt{\beta^2 - \varepsilon_i k_0^2}, \qquad k_0 = \frac{\omega}{c}, \qquad i \in \{d, m\}, \tag{4.7}$$

so that $\Re\{k_{z,i}\} > 0$ corresponds to exponential decay away from the interface. Solving Eq. 4.6 using Eq. 4.7 yields the single-interface SPP dispersion shown in Eq. 4.1 with the existence requirement Eq. 4.2 which guarantees evanescence on both sides and hence true surface binding.

Eq. 4.1 immediately gives the effective index and phase/attenuation split via $\beta = \beta' + j\beta''$:

$$n_{\text{eff}} = \frac{\beta'}{k_0} \tag{4.8}$$

$$L_p = \frac{1}{2\beta''} \tag{4.9}$$

Because ε_m is complex, β'' reflects Ohmic loss in the metal, while $\beta' > k_0\sqrt{\varepsilon_d}$ places the SPP to the right of the dielectric light line, consistent with the need for evanescent normal fields and momentum matching in excitation.

In the metal–insulator–metal stack, the longitudinal constant β couples the two interfaces through the normal (evanescent) wavenumbers

$$k_d = \sqrt{\beta^2 - \varepsilon_d k_0^2}, \qquad k_m = \sqrt{\beta^2 - \varepsilon_m k_0^2}, \tag{4.10}$$

which enforce decay away from the gap ($\Re\{k_d\} > 0$) and into the metals ($\Re\{k_m\} > 0$).

Applying the TM boundary conditions at both interfaces yields the symmetric (even) and antisymmetric (odd) eigenvalue relations. For the fundamental **even** TM_0

branch,

$$\tanh\left(\frac{k_d\, t}{2}\right) = -\,\frac{\varepsilon_m\, k_d}{\varepsilon_d\, k_m}, \tag{4.11}$$

and for the **odd** TM_1 branch,

$$\coth\left(\frac{k_d\, t}{2}\right) = -\,\frac{\varepsilon_m\, k_d}{\varepsilon_d\, k_m}. \tag{4.12}$$

Here t is the dielectric gap thickness. Equations Eq. 4.11–Eq. 4.12 determine $\beta(\omega, t)$ for the coupled interfaces and reduce to the single–interface dispersion in the limit $t \to \infty$.

Decreasing t increases $\Re\{\beta\}$ for TM_0 (stronger confinement) and typically increases $\Im\{\beta\}$ through larger metal overlap. .

4.3 Propagation and Decay Properties

From the dispersion analysis, the single–interface SPP is characterized by the complex in–plane constant $\beta(\omega) = \beta' + j\beta''$ in Eq. 4.1 and by the normal (evanescent) wavenumbers $k_{z,d}$ and $k_{z,m}$ defined in Eq. 4.7. These quantities determine how the mode propagates along the interface and decays away from it.

With the $e^{j\omega t}$ convention, the SPP varies as

$$e^{j\beta x} = e^{j\beta' x}\, e^{-\beta'' x}$$

along the interface, and as $e^{-k_{z,d} z}$ for $z > 0$ (dielectric) and $e^{+k_{z,m} z}$ for $z < 0$ (metal) in the normal direction. The associated penetration depths (amplitude $1/e$) follow directly from Eq. 4.7:

$$\delta_d = \frac{1}{\Re\{k_{z,d}\}}, \qquad \delta_m = \frac{1}{\Re\{k_{z,m}\}}. \tag{4.13}$$

Typically $\delta_m \ll \delta_d$, so most of the energy resides in the dielectric half–space.

Because modal intensity scales as $|e^{j\beta x}|^2 = e^{-2\beta'' x}$, the $1/e$ intensity propagation length is

$$L_p = \frac{1}{2\,\beta''}. \tag{4.14}$$

The time–averaged Poynting vector $\mathbf{S} = \frac{1}{2}\Re\{\mathbf{E}\times\mathbf{H}^*\}$ indicates forward power transport along x with energy density localized within $\sim \delta_d$ and $\sim \delta_m$ on the dielectric and metal sides, respectively. Loss enters through the imaginary part of the permittivity; the local absorbed power density is

$$p_{\text{abs}}(\mathbf{r}) = \frac{\omega}{2}\,\epsilon_0\,\epsilon''(\omega)\,|\mathbf{E}(\mathbf{r})|^2, \tag{4.15}$$

so increased overlap with regions of nonzero ϵ'' raises β'' and shortens L_p via Eq. 4.14.

From Eq. 4.1 and Eq. 4.7, stronger mode confinement arises when ε_d increases or ε'_m becomes more negative, as both effects elevate $\Re\{\beta\}$ and reduce the field penetration depth δ_d. Conversely, an increase in ε''_m enhances $\Im\{\beta\}$, thereby intensifying absorption losses and shortening the propagation length L_p. As the condition $\Re\{\varepsilon_m\} \approx -\varepsilon_d$ is approached, confinement grows markedly but decay becomes more pronounced. These interdependent variations between field localization and attenuation define the fundamental propagation and decay characteristics of surface plasmon polaritons.

4.3.1 Propagation at the Metal–Insulator Interface

At a single planar boundary ($z = 0$), the surface mode propagates tangentially with the complex longitudinal constant $\beta(\omega)$ given by the dispersion in Eq. 4.1. The normal (evanescent) wavenumbers in the dielectric and metal are those in Eq. 4.7, and the boundary relation Eq. 4.6 together with the existence condition Eq. 4.2 guarantees a nontrivial TM surface solution.

The compact representation of propagation and decay in each half–space is

$$\mathbf{K}_d = \big(\beta,\, 0,\, -j\,k_{z,d}\big), \qquad \mathbf{K}_m = \big(\beta,\, 0,\, +j\,k_{z,m}\big), \tag{4.16}$$

so fields vary as $e^{j\beta x}$ along the interface and decay as $e^{-k_{z,d}z}$ for $z > 0$ (dielectric) and $e^{+k_{z,m}z}$ for $z < 0$ (metal).

Each $\mathbf{K}_i$ satisfies the transverse (Helmholtz) relation already implied by Eq. 4.7:

$$\beta^2 - k_{z,i}^2 = \varepsilon_i k_0^2 \quad\Longleftrightarrow\quad \mathbf{K}_i\cdot\mathbf{K}_i = \varepsilon_i k_0^2, \qquad i \in \{d, m\}. \tag{4.17}$$

This connects the tangential and normal components of the SPP wave vector in each medium without re-deriving the dispersion.

Phase accumulation along the interface is set by $\Re\{\beta\}$ and attenuation by $\Im\{\beta\}$; the $1/e$ intensity propagation length is Eq. 4.14. Normal confinement is quantified by the penetration depths δ_d and δ_m in Eq. 4.13. Using the TM field relations, the time–averaged Poynting vector shows guided power strictly along x (no net normal transport). Material loss enters via the absorbed–power density Eq. 4.15, which increases $\Im\{\beta\}$ and shortens L_p through Eq. 4.14.

Equations Eq. 4.16–Eq. 4.17, together with β, $k_{z,d}$, and $k_{z,m}$ referenced above, provide the complete the propagation description.

4.4 Coupling and Resonance Condition

4.4.1 Coupling Condition

Here $\beta_{\mathrm{MIM}}(\lambda, t) = \beta' + j\beta''$ denote the longitudinal constant of the guided gap mode obtained from the coupled–interface dispersion equation with transverse wavenumbers from Eq. 4.7. Coupling is achieved when the external excitation supplies the same in–plane momentum as the MIM mode, and resonance follows from a round–trip phase condition in the chosen cavity geometry.

If a direct port is utilized, for an input waveguide of effective index $n_{\mathrm{in}}(\lambda)$,

$$\beta_{\mathrm{MIM}}(\lambda, t) = k_0(\lambda)\, n_{\mathrm{in}}(\lambda). \tag{4.18}$$

The free–space wavenumber is

$$k_0(\lambda) = \frac{2\pi}{\lambda}. \tag{4.19}$$

For a periodic coupler with grating period Λ and diffraction order $m \in \mathbb{Z}$,

$$\beta_{\mathrm{MIM}}(\lambda, t) = k_0(\lambda)\, n_{\mathrm{inc}}(\lambda)\, \sin\theta \;\pm\; m\,\frac{2\pi}{\Lambda}, \tag{4.20}$$

where n_{inc} and θ describe the incident medium and angle at the coupler.

4.4.2 Resonance Condition

Assuming a TM surface wave propagating along $+x$ at the flat interface $z = 0$ (dielectric for $z > 0$, metal for $z < 0$), the magnetic field envelopes in each half–space can be written as

$$H_y^{(d)}(x, z) = h_d\, e^{j\beta x}\, e^{-k_{z,d} z}, \qquad z > 0, \tag{4.21}$$

$$H_y^{(m)}(x, z) = h_m\, e^{j\beta x}\, e^{+k_{z,m} z}, \qquad z < 0, \tag{4.22}$$

where β is the longitudinal (in–plane) propagation constant and $k_{z,i}$ are the normal (evanescent) wave numbers already defined by Eq. 4.7

It is sometimes convenient to emphasize the "generalized wave–vector" relation between the tangential and normal components in each medium:

$$\beta^2 - k_{z,i}^2 = \varepsilon_i k_0^2 \quad \Longleftrightarrow \quad \mathbf{K}_i \cdot \mathbf{K}_i = \varepsilon_i k_0^2, \qquad \mathbf{K}_i = (\beta,\, 0,\, \mp j\, k_{z,i}), \tag{4.23}$$

with the upper (lower) sign for $z > 0$ ($z < 0$).

Applying the TM boundary conditions (continuity of H_y, E_x, and D_z) gives the single–interface characteristic relation obtained in Eq. 4.6

which, together with Eq. 4.7, yields the standard SPP dispersion

$$\beta = k_0 \sqrt{\frac{\varepsilon_m\, \varepsilon_d}{\varepsilon_m + \varepsilon_d}}. \tag{4.24}$$

Hence the common tangential component at the interface is

$$K_{1x} = K_{2x} = \beta, \tag{4.25}$$

and the decay constants $k_{z,d}, k_{z,m}$ follow from Eq. 4.7.

In the lossless view, as confinement strengthens ($\Re\{\beta\} \to \infty$), Eq. 4.1 approaches the *surface–plasmon condition*

$$\varepsilon_m + \varepsilon_d = 0. \tag{4.26}$$

For a Drude metal with negligible damping and $\varepsilon_\infty \approx 1$, taking $\varepsilon_d = 1$ (air) gives $\varepsilon_m(\omega) \approx 1 - \omega_p^2/\omega^2$. Inserting this into Eq. 4.26 yields the characteristic (single–interface) surface–plasmon resonant frequency

$$\omega = \frac{\omega_p}{\sqrt{2}}, \tag{4.27}$$

and the corresponding wavelength

$$\lambda = \frac{\lambda_p}{\sqrt{2}}, \qquad \lambda_p = \frac{2\pi c}{\omega_p}. \tag{4.28}$$

4.5 Sensing Mechanism

The sensing process begins by launching light into the input port of the device. This excitation couples into the metal–insulator–metal (MIM) waveguide, where the guided optical mode excites a gap–plasmon resonance once the in–plane momentum of the incident field matches the propagation constant of the supported mode, as described by the phase–matching condition in Eq. 4.18. This ensures efficient coupling of energy into the plasmonic waveguide.

Inside the resonator section, the guided plasmon propagates and circulates multiple times, forming standing waves through constructive interference. A resonance occurs when the accumulated phase along one complete round trip equals an integer multiple of 2π, satisfying the round–trip phase condition:

$$kL + 2\phi_{\mathrm{ref}} = m \cdot 2\pi, \tag{4.29}$$

where k is the propagation constant of the MIM mode, L is the effective cavity length, ϕ_{ref} is the reflection phase at each interface, and m is an integer mode number. Under this condition, the system exhibits a sharp feature—typically a dip or peak—in its transmission or reflection spectrum, signifying strong field confinement within the cavity.

When the refractive index of the dielectric region, which may represent the sensing medium or analyte, undergoes a change, the effective permittivity of the waveguide mode is modified according to the MIM dispersion relation in Eq. 4.11, with the transverse wavenumbers k_d and k_m defined in Eq. 4.10. This change alters the propagation constant of the MIM mode and thereby the effective optical path length within the resonator. As a result, the resonance wavelength shifts proportionally to the refractive–index variation, producing a measurable red– or blue–shift in the transmission spectrum. Monitoring this wavelength displacement forms the basis of label–free refractive–index sensing.

For small refractive–index perturbations, the relationship between the resonance wavelength shift and the change in refractive index can be obtained by differentiating the round–trip phase condition given in Eq. 4.29. Physically, the shift magnitude depends on how strongly the optical field overlaps with the analyte region—greater field confinement within the dielectric gap leads to a more pronounced response. Additionally, the product of the group index and cavity length determines the group delay within the resonator; a longer delay enhances the wavelength shift for a given perturbation.

Thus, the overall sensing mechanism can be viewed as an interplay between modal confinement, effective optical path length, and dispersion within the MIM cavity. A higher field overlap in the analyte and a slower group velocity jointly increase the spectral sensitivity, enabling precise refractive–index detection through resonance–wavelength tracking.

4.6 Dielectric Loss Function and Quality Factor

In a region with complex permittivity $\varepsilon(\omega) = \varepsilon' + j\,\varepsilon''$, the time–averaged absorbed power density is

$$p_{\text{abs}}(\mathbf{r}) = \frac{\omega}{2}\,\varepsilon_0\,\varepsilon''(\omega)\,|\mathbf{E}(\mathbf{r})|^2. \tag{4.30}$$

A compact spectral indicator of dissipation is the dielectric loss function,

$$L(\omega) = \operatorname{Im}\left\{-\frac{1}{\varepsilon(\omega)}\right\}, \tag{4.31}$$

which peaks near plasmonic resonances where $\varepsilon' \approx 0$ and $\varepsilon'' > 0$.

For a guided MIM mode with longitudinal constant $\beta = \beta' + j\beta''$, distributed absorption produces exponential decay of intensity along the guide; the $1/e$ intensity propagation length is given by Eq. 4.14. It is convenient to write the internal (power) attenuation per unit length as

$$\alpha_i = 2\,\beta'', \tag{4.32}$$

so that $\exp(-\alpha_i x)$ describes the power decay along the MIM section.

When the resonator has no mirrors (e.g., a ring or closed MIM loop), the resonance condition is the phase–closure of one round trip,

$$\Re\{\beta_{\mathrm{MIM}}(\lambda)\}\,L \;=\; 2\pi m, \qquad m \in \mathbb{Z}, \tag{4.33}$$

where L is the round–trip physical length. External coupling to a bus or feed waveguide extracts a power fraction C per round trip. The associated external round–trip loss is

$$A_e \;=\; -\ln(1-C) \;\approx\; C \quad (C \ll 1), \tag{4.34}$$

and the total round–trip power loss is

$$A_{\mathrm{rt}} \;=\; A_e \;+\; 2\,\alpha_i\,L. \tag{4.35}$$

The loaded spectral linewidth of a cavity resonance is, for small total loss,

$$\Delta\lambda \;\approx\; \frac{\lambda^2}{2\pi\,n_{g,\mathrm{MIM}}\,L}\,A_{\mathrm{rt}}. \tag{4.36}$$

The loaded quality factor follows from its definition,

$$Q_L \;=\; \frac{\lambda_{\mathrm{res}}}{\Delta\lambda}. \tag{4.37}$$

It partitions into internal and external contributions as

$$\frac{1}{Q_L} \;=\; \frac{1}{Q_i} \;+\; \frac{1}{Q_e}. \tag{4.38}$$

The internal Q is governed by the guided–mode attenuation,

$$Q_i \;\approx\; \frac{\Re\{\beta_{\mathrm{MIM}}\}}{2\,\Im\{\beta_{\mathrm{MIM}}\}} \;=\; \frac{\beta'}{2\,\beta''}, \tag{4.39}$$

and the external Q by the coupling loss per round trip,

$$Q_e \;\approx\; \frac{2\pi\, n_{g,\mathrm{MIM}}\, L}{\lambda_{\mathrm{res}}\, A_e}. \tag{4.40}$$

Equations Eq. 4.30–Eq. 4.40 show how material dissipation (ε''), modal attenuation (β''), and external coupling (A_e) set the observable linewidth and loaded quality factor of MIM resonators.

Chapter 5

Material Modeling

Material modeling links a material's structure and processing to its measurable properties and field response. It relies on constitutive relations that map stimuli (fields, stress, temperature) to outputs (polarization, magnetization, strain, conductivity) while respecting causality, conservation, and passivity. Models may be physics-based, phenomenological, or data-driven, but in all cases parameters are calibrated to reliable data and validated on independent conditions. The focus here is optical electromagnetics, where the central quantity is the complex, frequency-dependent permittivity (and, when needed, permeability or surface conductivity) used consistently in analysis and simulation.

5.1 Plasmonic Material Modelling

Plasmonic material modelling describes the optical response of metals and dielectrics through a complex, frequency-dependent permittivity.

$$\epsilon(\omega) = \epsilon'(\omega) + j\,\epsilon''(\omega) \tag{5.1}$$

The real part $\epsilon'(\omega)$ governs dispersion and the existence/position of surface–plasmon modes, while the imaginary part $\epsilon''(\omega)$ sets absorption, linewidth, and quality factor—thereby controlling confinement and sensing figures of merit in MIM devices[73].

Across typical sensing bands, metals are compactly represented by **Drude** (free–electron) or **Drude–Lorentz** (free + interband) forms that are causal and passive (Kramers–Kronig consistent); fitted over the band of interest, these models reproduce measured optical constants [73, 74]. Reliable target datasets include Johnson–Christy for noble metals and the tabulations in Palik's *Handbook of Optical Constants of Solids*; for the infrared, Ordal *et al.* provide canonical values [75–77].

In simulations and dispersion calculations, the chosen $\epsilon(\omega)$ is used directly in the frequency domain, or realized in the time domain via standard dispersive updates (e.g., ADE in FDTD), ensuring that computed mode profiles, resonance wavelengths, and linewidths reflect the same physically measured material response adopted for design[73, 74].

5.1.1 The Drude Model

The Drude model views conduction electrons as a free, classical electron gas that responds to an applied optical field while undergoing random collisions at an average rate $\gamma = 1/\tau$. Under these assumptions the material behaves linearly and locally, and its optical response is fully described by a complex, frequency-dependent permittivity with three parameters: the high-frequency background ϵ_∞ (accounting for bound electrons), the plasma frequency ω_p, and the damping rate γ [73, 74].

$$\epsilon(\omega) = \epsilon_\infty - \frac{\omega_p^2}{\omega^2 + j\gamma\omega} \tag{5.2}$$

The plasma frequency depends on the carrier density n and effective mass m^*:

$$\omega_p^2 = \frac{ne^2}{\epsilon_0 m^*}. \tag{5.3}$$

From Eq. 5.2 the following characteristics can be obtained about a particular material:

- **Dispersion.** The real part of $\epsilon(\omega)$ is typically negative for $\omega \lesssim \omega_p/\sqrt{\epsilon_\infty}$, which is the regime that supports surface-plasmon modes at metal–dielectric interfaces; above this crossover it becomes positive and the metal behaves more like a lossy dielectric [73].

- **Loss/linewidth.** The imaginary part grows with γ, describing Ohmic dissipation. Larger γ (e.g., in thin or rough films) broadens resonances and lowers quality factor; conversely, cleaner materials with smaller γ yield sharper spectral features [74, 75].

- **Low-frequency limit.** Using $\epsilon(\omega) = \epsilon_\infty - j\,\sigma(\omega)/(\epsilon_0\omega)$, the Drude form implies the familiar dc conductivity
$$\sigma_0 = \frac{\epsilon_0\,\omega_p^2}{\gamma}, \tag{5.4}$$
linking transport and optics through the same ω_p and γ.

the Drude model captures the free-electron response that dominates many plasmonic metals over near-IR to mid-IR bands. At higher photon energies, interband transitions of bound electrons produce additional structure in $\epsilon(\omega)$ not contained in Eq. 5.2; those contributions are treated separately in the following subsections. For numerical work (e.g., FDTD), ϵ_∞, ω_p, and γ are taken from reliable optical-constants datasets or fitted over the operating band to ensure causal, passive behavior in simulation [73, 74].

5.1.2 The Lorentz Model

The Lorentz model describes the bound–electron part of a material's optical response. Electrons are treated as harmonically bound to restoring centers and driven by an external field while experiencing damping from scattering and dephasing. This mechanism dominates in dielectrics and is required for metals at photon energies where interband transitions occur.

The driven–damped harmonic equation of motion for a representative electron (charge $-e$, effective mass m^*), with resonance frequency ω_0 and damping rate Γ, under a monochromatic field $E(t) = \Re\{E_0 e^{j\omega t}\}$ is given in Eq. 5.5.

$$m^*\ddot{x} + m^*\Gamma\dot{x} + m^*\omega_0^2 x = -\,e\,E_0 e^{j\omega t} \tag{5.5}$$

With number density n, the polarization is $P = -ne\,x$ and $D = \epsilon_0 E + P$. Solving Eq. 5.5 in steady state gives the single–oscillator permittivity Eq. 5.6.

$$\epsilon(\omega) = \epsilon_\infty + \frac{f\,\omega_p^2}{\omega_0^2 - \omega^2 - j\,\Gamma\omega} \tag{5.6}$$

Here ϵ_∞ is the high–frequency background, $\omega_p^2 = ne^2/(\epsilon_0 m^*)$ sets the spectral weight scale, and f is the (dimensionless) oscillator strength. Real materials are represented by a sum of oscillators as in Eq. 5.7.

$$\epsilon(\omega) = \epsilon_\infty + \sum_k \frac{f_k\,\omega_{p,k}^2}{\omega_{0,k}^2 - \omega^2 - j\,\Gamma_k\omega} \tag{5.7}$$

Separating Eq. 5.6 (or each term of Eq. 5.7) into real and imaginary parts yields Eq. 5.8–Eq. 5.9.

$$\epsilon'(\omega) = \epsilon_\infty + f\,\omega_p^2\,\frac{\omega_0^2 - \omega^2}{(\omega_0^2 - \omega^2)^2 + (\Gamma\omega)^2} \tag{5.8}$$

$$\epsilon''(\omega) = f\,\omega_p^2\,\frac{\Gamma\omega}{(\omega_0^2 - \omega^2)^2 + (\Gamma\omega)^2} \tag{5.9}$$

From Eq. 5.8–Eq. 5.9 the practical implications are:

- **Dispersion.** Near ω_0, the real part in Eq. 5.8 transitions from normal to anomalous dispersion, producing steep phase and group–index variation.
- **Absorption/linewidth.** The imaginary part in Eq. 5.9 peaks around ω_0 with a Lorentzian width set primarily by Γ, matching interband absorption in metals and electronic/vibrational bands in dielectrics.
- **Causality and passivity.** With $f_k > 0$ and $\Gamma_k > 0$, the multi–oscillator form Eq. 5.7 is Kramers–Kronig consistent and passive.
- **Role in plasmonics.** Lorentz terms raise $\epsilon'(\omega)$ and add $\epsilon''(\omega)$ near resonances (per Eq. 5.8–Eq. 5.9), shifting SPP dispersion and broadening spectral features relative to a free–electron description.

5.1.3 The Lorentz–Drude Model

The Lorentz–Drude model combines the free–electron response of metals with bound–electron resonances from interband transitions, yielding a compact, causal, and passive description of complex permittivity over wide spectral ranges [73, 74].

$$\epsilon(\omega) = \epsilon_\infty - \frac{\omega_p^2}{\omega^2 + j\gamma\omega} + \sum_k \frac{f_k\,\omega_{p,k}^2}{\omega_{0,k}^2 - \omega^2 - j\,\Gamma_k\omega} \tag{5.10}$$

where ϵ_∞ is the high–frequency background, ω_p and γ are the free–electron plasma frequency and damping rate, and each Lorentz term has oscillator strength f_k, resonance $\omega_{0,k}$, damping Γ_k, and spectral weight $\omega_{p,k}^2$. Positive f_k and Γ_k ensure passivity and Kramers–Kronig consistency.

From Eq. 5.10, the following characteristics can be observed:

- **Low–frequency (Drude–dominated).** The Drude term drives $\epsilon'(\omega)$ negative over a broad band and sets the baseline loss via γ, enabling surface plasmons at metal–dielectric interfaces [73].
- **Near interband energies (Lorentz–dominated).** Each oscillator produces a dispersive feature: $\epsilon'(\omega)$ varies rapidly (normal to anomalous dispersion) while $\epsilon''(\omega)$ peaks with width set mainly by Γ_k. These features shift zero–crossings of $\epsilon'(\omega)$, move resonances, and add absorption [73, 74].
- **Asymptotes.** As $\omega \to \infty$, both Drude and Lorentz contributions vanish as $1/\omega^2$, giving $\epsilon(\omega) \to \epsilon_\infty$; at microwave/terahertz limits, the behavior reduces to the Drude response with conductivity controlled by γ [73]..

The combined form captures the broad free–electron background and narrow interband structure with a minimal parameter set; in MIM sensors, the Drude part sets confinement and baseline loss, while Lorentz terms govern visible–band dispersion and linewidth, affecting resonance wavelength, FWHM, and figure of merit [73, 74]

5.2 Materials

Silver (Ag) served as the substrate (ground) metal, chosen for its visible–near-IR permittivity combining a large negative real part with comparatively low loss; its dispersion was modeled with a Lorentz–Drude form fitted to the dataset in *Optical Constants of the Noble Metals* [76]. Air acted as the waveguide gap and was treated as linear, isotropic, and lossless with $\epsilon = \epsilon_0$, $\mu = \mu_0$, and $\sigma = 0$. Together these choices set the baseline confinement, resonance position, and linewidth for the guided TM mode in the metal–insulator–metal (MIM) resonator.

5.2.1 Silver (Ag): Characteristics and Modeling

Silver was selected for visible–near-IR plasmonics because its permittivity combined a large negative real part with comparatively low loss across much of the visible band; interband transitions lay mainly in the near-UV, so absorption remained modest where the device operated. Consequently, field confinement was tighter, resonances were sharper, and figures of merit were higher than for most alternative metals. These trends were consistent with canonical optical-constants measurements for silver and were used as the target for model fitting [75].

For device modelling, Ag was represented by a Drude background with a small number of Lorentz oscillators to capture near-UV interband features, fitted to the dataset over the operating band [76]. When thin films were employed, additional damping from grain boundaries and surface roughness was reflected by an increased Drude damping rate relative to bulk, which broadened spectral features in simulation and measurement. Size-induced damping was described by

$$\gamma_{\text{eff}} \approx \gamma_{\text{bulk}} + A\,\frac{v_F}{L}, \tag{5.11}$$

with v_F the Fermi velocity, L a characteristic dimension (e.g., film thickness or feature size), and $A \sim \mathcal{O}(1)$ capturing surface specularity. Impact of Ag on the structure:

- **Substrate (ground) metal:** Ag formed the reflective ground plane, setting the phase condition and providing a low-loss return path.
- **Field coupling and confinement:** The large negative ϵ' supported strong TM surface–plasmon coupling at the metal–dielectric interface and maintained high reflectivity without excess damping.
- **Loss and linewidth:** The comparatively small ϵ'' reduced Ohmic dissipation in the ground layer, yielding **narrower linewidths** (higher Q) than higher-loss metals for the same geometry.

- **Sensitivity (nm/RIU):** For a fixed geometry, the spectral shift was governed mainly by the gap material; using Ag as the substrate altered sensitivity only weakly through dispersion.

- **Figure of merit (FOM):** Narrower lines from lower ϵ'' improved the ratio of sensitivity to linewidth relative to higher-loss substrates.

5.2.2 Air : Characteristics and Modeling

Air was used as the waveguide material (gap) in the metal–insulator–metal (MIM) structure. With $n \approx 1$ and negligible absorption across the operating band, it behaved as a linear, isotropic, lossless medium with essentially flat dispersion over the wavelengths of interest.

A low-index gap lowered the modal effective index and reduced field confinement compared with higher-index fills. The smaller metal–field overlap decreased Ohmic loss, so resonances were **narrower** and propagation lengths **longer** than for the same geometry filled with a higher-index material. Spectrally, the fundamental TM gap-plasmon resonance appeared at a **shorter wavelength** (blue-shifted) relative to higher-index fills.

Reasoning behind choosing Air:

- **Sensitivity (nm/RIU):** Lower than with higher-index gap materials. Because the field fraction in the gap was smaller and the dispersion slope with respect to the gap index was gentler, the resonance wavelength shifted **less per unit index change** when the baseline medium was air.

- **FOM (sensitivity/linewidth):** Often **higher** with air despite the lower absolute sensitivity. The reduced loss in the low-index gap produced **narrower linewidths**, which improved the ratio of sensitivity to linewidth.

- **Trade-off:** Replacing air with a higher-index gap generally **increased sensitivity** (larger wavelength shift per RIU) but **broadened** the resonance (larger FWHM) due to stronger metal overlap; keeping air typically yielded **moderate sensitivity** but **superior FOM** for the same geometry.

Chapter 6

Simulation Modeling

Physical phenomena in science and engineering, such as electromagnetic wave interaction, heat conduction, fluid dynamics, and many more, are inherently dependent on both space and time. These processes are typically governed by partial differential equations (PDEs), which describe how physical quantities evolve continuously within a medium. However, when the system involves complex geometries, heterogeneous materials, or nonlinear interactions, obtaining exact analytical solutions becomes exceedingly challenging. To overcome these challenges, numerical methods are employed to approximate field variations by discretizing both space and time into finite elements or grids. Among these, techniques such as the Finite Difference Time Domain (FDTD), Finite Element Method (FEM) [78] are widely adopted for solving PDEs in physics and engineering. Modern computational tools implement these methods to simulate the propagation, absorption, and interaction of waves or particles within intricate structures. As a result, computer-based simulations have become essential for predicting real-world behavior, optimizing device performance, and visualizing physical phenomena that are otherwise difficult to observe experimentally.

6.1 Finite Element Method

For solving partial differential equations, the Finite Element Method (FEM) is a powerful numerical technique, particularly in systems with complex geometries and nonuniform materials. It works by dividing the domain into small interconnected elements where field quantities are approximated, and PDEs are transformed into algebraic equations that can be solved computationally. FEM works on irregular shapes, mixed element types, and adaptive mesh refinement to improve accuracy [79, 80].

However, the Finite Difference Time Domain (FDTD) [81] method offers key advantages for time-dependent electromagnetic problems. Unlike FEM, which often works in the frequency domain and requires solving large matrix equations, FDTD directly computes field evolution in the time domain using simple update equations. This makes it faster and more memory-efficient. FDTD is especially effective for studying wave propagation, scattering, and plasmonic behavior in dispersive or nonlinear media, making it a preferred method for modern plasmonic simulations.

6.2 Finite-Difference Time-Domain Method

The Finite Difference Time Domain (FDTD) method is a widely adopted numerical approach for solving Maxwell's equations in both time and space domains to simulate electromagnetic wave propagation, interaction, and scattering in complex structures. The fundamental concept behind FDTD is the discretization of Maxwell's time-dependent equations on a spatial grid, where field components are updated step by step over successive time intervals. FDTD can capture the full transient behavior of electromagnetic fields through this explicit time-stepping scheme, making it especially effective for time-dependent analyses. Because it directly computes both electric and magnetic field components over the computational domain, the method offers clear physical insight into plasmonic device design [82].

6.2.1 Maxwell's Time-Domain Equations

The starting point of the Finite-Difference Time-Domain (FDTD) method is Maxwell's curl equations in differential form:

$$\frac{\partial \mathbf{H}}{\partial t} = -\frac{1}{\mu}(\nabla \times \mathbf{E}) \tag{6.1}$$

$$\frac{\partial \mathbf{E}}{\partial t} = \frac{1}{\varepsilon}(\nabla \times \mathbf{H}) \tag{6.2}$$

Here, $\mathbf{E}$ is the electric field vector, $\mathbf{H}$ is the magnetic field vector, μ is the permeability, and ε is the permittivity of the medium.

Since both $\mathbf{E}$ and $\mathbf{H}$ are vector fields, each with three components, the above equations expand into six coupled first-order partial differential equations in Cartesian coordinates:

$$\frac{\partial H_x}{\partial t} = -\frac{1}{\mu}\left(\frac{\partial E_z}{\partial y} - \frac{\partial E_y}{\partial z}\right) \tag{6.3}$$

$$\frac{\partial H_y}{\partial t} = -\frac{1}{\mu}\left(\frac{\partial E_x}{\partial z} - \frac{\partial E_z}{\partial x}\right) \tag{6.4}$$

$$\frac{\partial H_z}{\partial t} = -\frac{1}{\mu}\left(\frac{\partial E_y}{\partial x} - \frac{\partial E_x}{\partial y}\right) \tag{6.5}$$

$$\frac{\partial E_x}{\partial t} = \frac{1}{\varepsilon}\left(\frac{\partial H_z}{\partial y} - \frac{\partial H_y}{\partial z}\right) \tag{6.6}$$

$$\frac{\partial E_y}{\partial t} = \frac{1}{\varepsilon}\left(\frac{\partial H_x}{\partial z} - \frac{\partial H_z}{\partial x}\right) \tag{6.7}$$

$$\frac{\partial E_z}{\partial t} = \frac{1}{\varepsilon}\left(\frac{\partial H_y}{\partial x} - \frac{\partial H_x}{\partial y}\right) \tag{6.8}$$

These coupled equations highlight the interdependence of electric and magnetic fields in space and time, forming the mathematical basis of the FDTD method [83–85].

6.2.2 The Yee Grid

To implement these equations numerically, space and time must be discretized. The most common discretization framework is the **Yee grid**, introduced by Kane S. Yee in 1966. In this scheme, the computational domain is divided into small cubic cells. The electric field components (E_x, E_y, E_z) are positioned along the edges of each cube, while the magnetic field components (H_x, H_y, H_z) are positioned at the centers of the cube's faces. This staggered arrangement ensures that every electric field component is surrounded by four magnetic field components, and every magnetic field component is surrounded by four electric field components. Such positioning directly enforces Faraday's and Ampère's laws on the grid, ensuring accurate coupling of the fields.The yee grid is shown in Fig. 6.1. The Yee grid also staggers the fields in time. Electric fields are updated at integer multiples of the time step, while magnetic fields are updated at half-integer multiples. This combination of spatial and temporal staggering forms the basis of the leapfrog scheme [86].

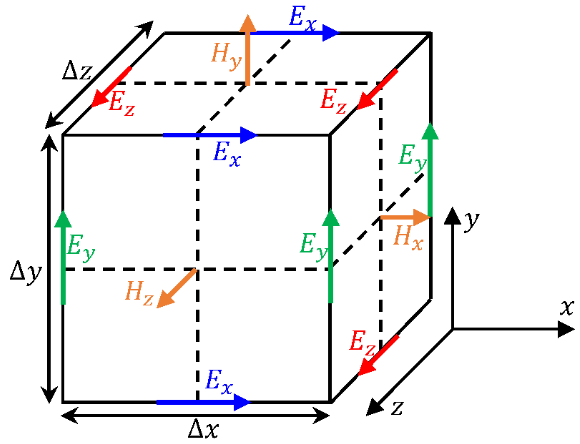

Fig 6.1: Yee Grid.[87]

6.2.3 The Leapfrog Scheme

The leapfrog scheme is the time-stepping method used in FDTD. It updates the electric and magnetic fields alternately in time, with each set of fields computed half a time step apart.

Electric fields are updated at times $t = n\Delta t$, and magnetic fields are updated at times $t = (n + \frac{1}{2})\Delta t$.

The update sequence is as follows:

1. Use magnetic fields $\mathbf{H}(t - \frac{1}{2}\Delta t)$ to calculate electric fields $\mathbf{E}(t)$.
2. Use the newly calculated electric fields $\mathbf{E}(t)$ to update magnetic fields $\mathbf{H}(t+\frac{1}{2}\Delta t)$.

This leapfrogging process continues through successive time steps, with the electric and magnetic fields "leaping" over one another. The scheme ensures strong temporal coupling, provides second-order accuracy in both time and space, and naturally conserves energy [88].

6.2.4 Stability Condition

A critical factor in FDTD simulations is ensuring numerical stability. If the time step Δt is too large, the solution becomes unstable and diverges. Stability is governed by the Courant–Friedrichs–Lewy (CFL) condition:

$$\Delta t \leq \frac{1}{c\sqrt{\left(\frac{1}{\Delta x^2}+\frac{1}{\Delta y^2}+\frac{1}{\Delta z^2}\right)}} \tag{6.9}$$

Here, Δx, Δy, and Δz are the spatial step sizes in the three directions, and c is the speed of light in the medium. This condition ensures that the numerical wave velocity does not exceed the physical propagation speed [89].

6.2.5 FDTD Formulation

In conventional FDTD analysis, the permittivity of a material is often treated as a fixed constant; however, this assumption is not accurate in practice. In reality, both the permittivity and permeability of materials vary with frequency, leading to dispersion, a phenomenon where different frequency components of a wave travel at different speeds. This frequency dependence distorts the waveform as it propagates, making it essential to use dispersive FDTD techniques for realistic electromagnetic modeling.

To accurately represent this behavior, the FDTD method has been extended into three principal formulations for handling material dispersion:

1. **The Auxiliary Differential Equation (ADE) Method:** Proposed by **Taflove**, this technique introduces auxiliary differential equations to represent frequency-dependent material behavior in the time domain.

2. **The Z-Transform (ZT) Approach:** Developed by **Sullivan**, this method employs Z-domain algebra to convert convolution operations into discrete recurrence relations, improving numerical precision in dispersive simulations.

3. **The Recursive Convolution (RC) Technique:** Introduced by **Luebbers**, this approach uses recursive evaluation of convolution integrals to efficiently incorporate material dispersion without heavy computational cost.

Each of these methods provides a systematic framework for incorporating frequency-dependent material properties into the FDTD algorithm.

6.2.5.1 Auxiliary Differential Equation (ADE) Technique

The ADE technique translates frequency-domain material equations into time-domain differential equations that can be integrated alongside Maxwell's equations in FDTD. The starting point is the frequency-domain form of Ampère's law,

$$j\omega\varepsilon_r(\omega)c\mathbf{E} = \nabla \times \mathbf{H}, \tag{6.10}$$

where c is the speed of light in vacuum. Applying the inverse Fourier transform ($j\omega \to \partial/\partial t$) leads to a system of coupled time-domain equations:

$$\varepsilon_\infty \frac{\partial \mathbf{E}}{\partial t} + \mathbf{J} + \sum_{p=1}^{P} \frac{\partial \mathbf{Q}_p}{\partial t} = c\nabla \times \mathbf{H}, \tag{6.11}$$

$$\frac{\partial \mathbf{J}}{\partial t} + \nu_D \mathbf{J} = \omega_D^2 \mathbf{E}, \tag{6.12}$$

$$\frac{\partial^2 \mathbf{Q}_p}{\partial t^2} + \nu_p \frac{\partial \mathbf{Q}_p}{\partial t} + \omega_p^2 \mathbf{Q}_p = \Delta\varepsilon G_p \omega_p^2 \mathbf{E}. \tag{6.13}$$

In these equations, $\mathbf{J}$ is the polarization current density associated with the free-electron Drude response, and $\mathbf{Q}_p$ is the induced polarization of the p-th Lorentz oscillator. Eq. 6.12 describes a first-order damped oscillator: electrons accelerate under the electric field (term $\omega_D^2\mathbf{E}$) and lose momentum through collisions (term $\nu_D\mathbf{J}$). Eq. 6.13 is a second-order oscillator equation representing bound electrons vibrating about equilibrium positions with natural frequency ω_p and damping ν_p.

By discretizing these equations with central finite differences in both time and space, the ADE method introduces auxiliary variables $\mathbf{J}$ and $\mathbf{Q}_p$ into the FDTD algorithm. These auxiliary quantities are updated at every time step together with the electromagnetic fields, thereby allowing the model to reproduce frequency dispersion without evaluating convolution integrals. Because of its simplicity and stability, ADE is widely used for Drude and Drude–Lorentz metals in plasmonic simulations[90, 91].

6.2.5.2 Z-Transform Technique

The Z-Transform (ZT) method provides another route to represent dispersion in discrete time. It exploits the property that convolution in the time domain becomes multiplication in the Z-domain, enabling the derivation of exact difference equations that relate **D** and **E**.

Rewriting the Drude–Lorentz permittivity in a form suited for discrete implementation gives

$$\varepsilon_r(\omega) = \varepsilon_\infty + \frac{\omega_D^2/\nu_D}{j\omega - \omega_D^2/\nu_D} + \sum_{p=1}^{P} \frac{\Delta\varepsilon G_p \omega_p^2 \beta}{\beta^2 + \alpha^2 + j2\alpha\omega + j\omega^2}. \tag{6.14}$$

Here α and β are real coefficients describing damping and oscillation, respectively. Applying the Z-transform to the constitutive relation $\mathbf{D}(\omega) = \varepsilon_r(\omega)\mathbf{E}(\omega)$ and performing the inverse transform yields the discrete-time update equations:

$$\mathbf{E}^{n+1} = \frac{1}{\varepsilon_\infty}\left(\mathbf{D}^{n+1} - \mathbf{M}^n - \sum_{p=1}^{P} \mathbf{Q}_p^n\right), \tag{6.15}$$

$$\mathbf{M}^{n+1} = (1 + e^{-\nu_D \Delta t})\mathbf{M}^n - e^{-\nu_D \Delta t}\mathbf{M}^{n-1} + \omega_D^2 \frac{\Delta t}{\nu_D}(1 - e^{-\nu_D \Delta t})\mathbf{E}^{n+1}, \tag{6.16}$$

$$\mathbf{Q}_p^{n+1} = 2e^{-\alpha\Delta t}\cos(\beta\Delta t)\mathbf{Q}_p^n - e^{-2\alpha\Delta t}\mathbf{Q}_p^{n-1} + \Delta\varepsilon G_p \omega_p^2 \frac{\Delta t}{\beta} e^{-\alpha\Delta t}\sin(\beta\Delta t)\mathbf{E}^{n+1}. \tag{6.17}$$

The index n denotes the discrete time step and Δt is the FDTD time increment. **M** represents the auxiliary variable for the Drude response, and $\mathbf{Q}_p$ corresponds to Lorentz polarizations. Because these relations are derived analytically rather than through approximate differencing, the Z-Transform technique yields higher numerical accuracy and reduced phase error compared with ADE, making it suitable for broadband analyses [92, 93].

6.2.5.3 Recursive Convolution (RC) Techniques

The Recursive Convolution (RC) family represents a third approach for dispersive modeling in FDTD. These methods start directly from the convolution relation between **D** and **E** in the time domain:

$$\mathbf{D}(\omega) = \varepsilon_0 \varepsilon_r(\omega)\mathbf{E}(\omega), \tag{6.18}$$

whose inverse Fourier transform is

$$\mathbf{D}(t) = \varepsilon_0 \varepsilon_\infty \mathbf{E}(t) + \varepsilon_0 \int_0^t \mathbf{E}(t-\tau)\chi(\tau)\, d\tau. \tag{6.19}$$

Here ε_0 is the vacuum permittivity and $\chi(\tau)$ is the impulse-response (susceptibility) function describing how past electric fields influence the present displacement. The integral term $\mathbf{P}(t) = \varepsilon_0 \int_0^t \mathbf{E}(t-\tau)\chi(\tau)\,d\tau$ represents the induced polarization. Evaluating this integral directly at every time step is computationally expensive; hence, recursive schemes are introduced.

In the basic RC method, the polarization is approximated as a discrete sum:

$$\mathbf{P}(n\Delta t) = \sum_{m=0}^{n-1} \mathbf{E}^{n-m}\,\chi_m. \tag{6.20}$$

where

$$\chi_m = \int_{m\Delta t}^{(m+1)\Delta t} \chi(\tau)\,d\tau. \tag{6.21}$$

This assumes $\mathbf{E}$ remains constant during each time step. To improve accuracy, the Piecewise Linear Recursive Convolution (PLRC) method assumes the field varies linearly:

$$\mathbf{P}(n\Delta t) = \sum_{m=0}^{n-1} \left[\mathbf{E}^{n-m}\chi_m + (\mathbf{E}^{n-m-1} - \mathbf{E}^{n-m})\xi_m\right], \tag{6.22}$$

where

$$\xi_m = \frac{1}{\Delta t}\int_{m\Delta t}^{(m+1)\Delta t} (\tau - m\Delta t)\chi(\tau)\,d\tau. \tag{6.23}$$

A further refinement, the Trapezoidal Recursive Convolution (TRC) technique, uses the average of two successive electric fields:

$$\mathbf{P}(n\Delta t) = \sum_{m=0}^{n-1} \frac{\mathbf{E}^{n-m} + \mathbf{E}^{n-m-1}}{2}\chi_m. \tag{6.24}$$

Substituting this form into Maxwell's curl equation leads to

$$\mathbf{E}^{n+1} = \frac{\varepsilon_\infty - \chi_0/2}{\varepsilon_\infty + \chi_0/2}\mathbf{E}^n + \frac{1}{\varepsilon_\infty + \chi_0/2}\boldsymbol{\phi}^n + \frac{c\Delta t}{\varepsilon_\infty + \chi_0/2}(\nabla \times \mathbf{H}^{n+1/2}), \tag{6.25}$$

where $\boldsymbol{\phi}^n = \boldsymbol{\phi}_D^n + \sum_{p=1}^{P} \Re[\boldsymbol{\phi}_p^n]$ and

$$\boldsymbol{\phi}_D^n = \frac{\mathbf{E}^n + \mathbf{E}^{n-1}}{2}\Delta\chi_D^0 + e^{-\nu_D \Delta t}\boldsymbol{\phi}_D^{n-1}, \tag{6.26}$$

$$\boldsymbol{\phi}_p^n = \frac{\mathbf{E}^n + \mathbf{E}^{n-1}}{2}\Delta\chi_p^0 + e^{\gamma\Delta t}\boldsymbol{\phi}_p^{n-1}, \tag{6.27}$$

with $\gamma = -\alpha + j\beta$. For materials following the Drude–Critical-Point model, the time-domain susceptibility is

$$\bar{\chi}_p(t) = 2\Delta\varepsilon_p \omega_p e^{-\nu_p t} \sin(\omega_p t - \rho_p), \tag{6.28}$$

which is not directly recursive because of the sine term. Introducing a complex susceptibility

$$\tilde{\chi}_p(t) = 2j\Delta\varepsilon_p \omega_p e^{j\rho_p} e^{-\gamma t}, \qquad \Re[\tilde{\chi}_p(t)] = \bar{\chi}_p(t), \tag{6.29}$$

yields the recursive expression

$$\boldsymbol{\phi}_p^n = \frac{\mathbf{E}^n - \mathbf{E}^{n-1}}{2} \Delta\tilde{\chi}_0 + e^{-\gamma\Delta t} \boldsymbol{\phi}_p^{n-1}. \tag{6.30}$$

This allows the critical-point correction to be integrated seamlessly into the TRC-FDTD framework, while the Drude term is handled analogously via Eq. 6.26. Thus, the TRC formulation unifies Drude, Lorentz, and D-CP contributions under a single recursive scheme [94].

6.2.6 FDTD Softwares

There are nearly thirty well-known software platforms developed for electromagnetic simulation based on the Finite-Difference Time-Domain (FDTD) method. The first commercial FDTD solver was introduced by Computer Simulation Technology (CST), marking the beginning of numerical time-domain analysis tools for complex electromagnetic structures [95]. Following this, several other powerful and specialized solvers were developed, including MEEP [96], FDTD++ [97], FullWave [98], Tidy3D [99] , and ANSYS Lumerical FDTD [100]. Among these, ANSYS Lumerical FDTD has gained wide recognition for its accuracy, user-friendly interface, and advanced capabilities in nanophotonics and plasmonic sensor design. One of its key advantages is the Lumerical Script Language (LSF), which allows users to fully automate simulations, control parameters, and perform post-processing with precision. Furthermore, Lumerical provides Python integration tools through its LumAPI library, enabling seamless communication between Python and the FDTD engine [101]. This integration allows researchers to combine numerical simulations with optimization algorithms, reinforcement learning, and data analysis workflows. Additionally, Lumerical's extensive example library and documentation offer a wide range of pre-built models and tutorials, covering applications from basic waveguide analysis to advanced plasmonic and photonic device design, making it a versatile and powerful platform for this research work. [100]

6.2.7 Boundary Conditions in Ansys Lumerical FDTD

In Ansys Lumerical FDTD, several boundary conditions are available to define how electromagnetic fields interact with the edges of the simulation region. The appropriate selection of boundary type depends on the geometry, symmetry, and excitation source of the structure. The commonly used boundary conditions are described below:

1. **Metal (Perfect Electric Conductor) Boundary**
   The metal or perfect electric conductor (PEC) boundary assumes that the surface is an ideal reflector. Under this condition, 100% of the incident wave is reflected and 0% is transmitted or absorbed. The tangential component of the electric field becomes zero at the surface, and the reflected wave undergoes a phase reversal. This type of boundary is typically used for metallic walls or when exploiting electric-field symmetry where a node exists along the plane [102].

2. **Periodic Boundary Condition (PBC)**
   The periodic boundary condition is used when both the geometry and the electromagnetic field distribution repeat periodically in space. It is commonly applied with a plane wave source, where the field on one boundary face is linked to the opposite boundary with a phase shift corresponding to the wave propagation vector. This enables efficient simulation of infinite or repeating structures such as photonic crystals, metamaterial arrays, or plasmonic gratings using only a single unit cell [103].

3. **Perfectly Matched Layer (PML)**
   The perfectly matched layer (PML), introduced by Berenger, is one of the most effective boundary techniques in FDTD. It functions as an artificial layer surrounding the computational domain, designed to allow electromagnetic waves

to exit the simulation region without reflection. As waves enter the PML, they are exponentially attenuated until they diminish to negligible levels, preventing their return to the main region [104].

In Ansys Lumerical, several PML variants are available:

- **Standard PML:** Used for normal incidence and general-purpose applications.
- **Steep-Angle PML:** Optimized for oblique or grazing incidence waves.
- **Stabilized PML:** Improves numerical stability for broadband or long-duration simulations.
- **Custom PML:** Allows manual tuning of layer thickness, polynomial grading, and scaling profiles to achieve user-specific performance.

4. **Symmetric and Antisymmetric Boundaries**
These boundary conditions are employed when the electromagnetic field exhibits mirror symmetry relative to a reference plane. The **symmetric boundary** enforces zero normal derivative of the electric field across the plane (magnetic mirror condition), while the antisymmetric boundary forces the electric field itself to zero along the plane (electric mirror condition). Such symmetry-based boundaries significantly reduce computational time by allowing only half or a quarter of the structure to be simulated [105].

In this study, **Perfectly Matched Layer (PML)** boundaries were implemented on all exterior sides of the computational domain to suppress unwanted reflections and achieve accurate representation of wave propagation in an open-space environment. Because computational memory and processing capacity are inherently limited, it is not feasible to model an infinitely large region within FDTD simulations. The PML overcomes this limitation by enclosing the finite simulation domain with an absorbing layer that attenuates outward-propagating electromagnetic waves, thereby preventing their reflection back into the active simulation region. [104]

6.2.8 Sources in Ansys Lumerical FDTD

In Lumerical FDTD, a variety of excitation sources are available to model different physical conditions of electromagnetic wave propagation. The choice of the appropriate source depends on the geometry of the structure, type of illumination, and the desired analysis outcome. Each source provides a specific way to introduce electromagnetic energy into the simulation domain, allowing accurate modeling of light–matter interaction in plasmonic and photonic systems. The major types of sources available in Lumerical FDTD [106] are discussed below :

1. **Plane Wave Source:**
   The plane wave source generates light that propagates in a uniform direction, with the same phase and amplitude at all grid points. This makes it ideal for simulating uniform illumination across large areas, such as in thin-film structures or plasmonic surfaces. It is particularly effective for studying surface plasmon excitation, reflection, transmission, and absorption under both normal and oblique incidences.

2. **Gaussian Source:**
   A Gaussian Source in Lumerical FDTD defines a beam of electromagnetic radiation that propagates in a specific direction, with its amplitude following a Gaussian distribution across the cross-section of the beam. This results in a beam that has the highest intensity at its center and gradually decays toward the edges. By default, Gaussian sources in Lumerical employ the scalar beam approximation for the electric field, which assumes that the field components in the direction of propagation are negligible. This approximation remains valid as long as the beam waist is significantly larger than the diffraction limit, ensuring that the field variation is primarily transverse.

3. **BFAST (Broadband Fixed Angle Source Technique):**
   The BFAST source is used to perform broadband simulations at a fixed angle of incidence. This approach allows the analysis of wavelength-dependent responses for structures illuminated at specific angles without running separate simulations for each angle. It is especially useful for studying the spectral characteristics of

plasmonic and photonic sensors under angular illumination.

4. **Beam Source:**
   When the structure cannot employ periodic boundary conditions—such as in isolated or non-periodic geometries—a beam source is used. It represents a focused Gaussian beam that naturally decays at the boundaries of the simulation domain. This property allows the application of **Perfectly Matched Layer (PML)** boundary conditions on the sides to absorb outgoing waves efficiently. The beam source is commonly used to model focused light, such as in microscopy or localized excitation in plasmonic devices.

5. **Dipole Source:**
   The dipole source represents a point emitter that radiates electromagnetic energy from a specific location and orientation. It is used to model nanoscale emitters such as fluorescent molecules, quantum dots, or nanoantennas. This source is valuable for studying near-field interactions, spontaneous emission, and coupling effects between nanoscale emitters and surrounding plasmonic structures.

6. **Total-Field Scattered-Field (TFSF) Source:**
   The TFSF source defines a rectangular region within the simulation that separates the total-field region (containing both incident and scattered fields) from the scattered-field region (containing only scattered fields). The FDTD algorithm automatically removes the incident field outside the box, ensuring that only scattered or reflected light is observed in that region. This configuration is particularly useful for calculating scattering and absorption cross-sections of nanoparticles and other resonant structures.

7. **Mode Source:**
   The mode source is used when light is confined within a specific guiding structure, such as an optical fiber or waveguide. It injects a predefined optical mode consistent with the geometry and refractive index distribution of the guiding medium. This source is essential for simulating integrated photonic circuits, plasmonic waveguides, and coupling between guided modes and resonant cavities.

In this research, a **Mode Source** has been used to excite the fundamental optical mode through the waveguide structure. The source region was carefully designed with a sufficiently large width so that the electromagnetic fields are not truncated at the edges of the source. When the source region is too narrow, a significant portion of the optical field is clipped, causing mode distortion and undesired spreading of light (see Fig. 6.2). Increasing the source width reduces eigenmode tail-clipping, leading to lower propagation loss and improved mode confinement (see Fig. 6.3).

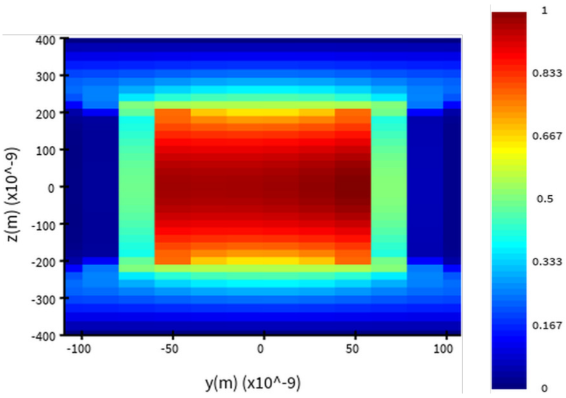

Fig 6.2: Narrow Source Width

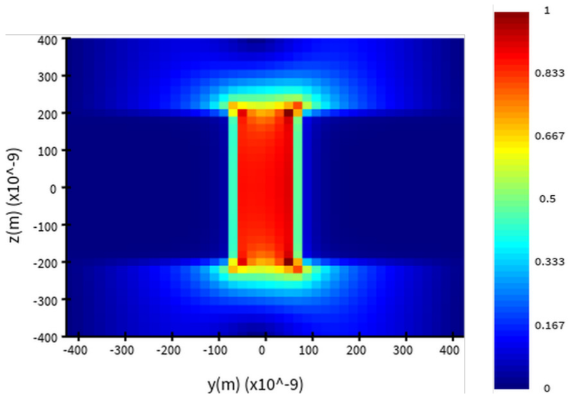

Fig 6.3: Wider Source Width

6.2.9 Monitors in Ansys Lumerical FDTD

In Finite-Difference Time-Domain (FDTD) simulations, **monitors** are used to record electromagnetic field data, material properties, and power flow at specific regions or time intervals. Lumerical FDTD provides a variety of built-in monitor types, each tailored for a particular analysis objective. The most commonly used monitors are described below.

1. **Refractive Index Monitor:** The Refractive Index Monitor provides a spatial map of the refractive index distribution throughout the simulation domain. It displays both the real and imaginary components of the refractive index at each point of the simulation region.

2. **Field Time Monitor:** The Field Time Monitor records the time-dependent evolution of the electromagnetic fields (**E** and **H**) during the simulation. This is essential for understanding the transient response of a structure. The recorded data can be used to study wave propagation, reflection, and absorption as functions of time.

3. **Movie Monitor:** The Movie Monitor allows visualization of field propagation as an animation. It records field snapshots over time, enabling users to observe how electromagnetic waves travel, interact with materials, and evolve throughout the simulation space.

4. **Frequency-Domain Field Profile Monitor:** The Frequency-Domain Field Profile Monitor captures the steady-state field distribution over a specified frequency or wavelength range. It computes the electric (**E**) and magnetic (**H**) field components in the frequency domain using Fourier transforms of the time-domain data. To obtain field intensity maps at resonance wavelengths, this monitor can be used.

5. **Frequency-Domain Field and Power Monitor:** The Frequency-Domain Field and Power Monitor extends the field profile analysis by also computing the power flow, Poynting vector, and transmission spectra across the monitored region. In this research, the recorded data represent only the intrinsic coupling between the incident light and the resonator. This configuration allows precise evaluation of light coupling, resonance strength, sensitivity, and the figure of merit (FOM) in the plasmonic sensor.

6. **Mode Expansion Monitor:** The Mode Expansion Monitor decomposes the electromagnetic field into a set of orthogonal waveguide modes or eigenmodes at a specified cross-section. It calculates the modal power coupling coefficients to determine how much optical power is transmitted into specific modes of a waveguide or resonator.

7. **RCWA Field Monitor:** The Rigorous Coupled-Wave Analysis (RCWA) Field Monitor is used for periodic or multilayered structures where the field can be represented as a sum of Fourier harmonics.

Chapter 7

Performance Metrics

7.1 Transmittance

Transmittance quantifies the fraction of input optical power that reaches the output port of the device. For a sensor excited by a guided mode, the time-averaged power through a port is obtained by integrating the normal component of the Poynting vector over the port cross-section [107]. If P_{in} and P_{out} denote the input and output powers, then

$$T = \frac{P_{\text{out}}}{P_{\text{in}}}. \tag{7.1}$$

7.2 Reflectance

Reflectance represents the fraction of incident optical power that is reflected back from the surface or interface of the plasmonic sensor. When an electromagnetic wave impinges on the metal–dielectric interface, a portion of it is reflected, a portion is transmitted, and some part may be absorbed due to ohmic losses in the metal [108]. The reflectance (R) quantifies the ratio of reflected power P_{ref} to incident power P_{in}.

$$R = \frac{P_{\text{ref}}}{P_{\text{in}}}. \tag{7.2}$$

7.3 Slater's Law

Slater's Law is an empirical rule that provides an approximate method to estimate the effective refractive index or dielectric constant of a composite material based on the refractive indices and volume fractions of its constituent materials. In plasmonic sensor design, Slater's Law is particularly useful when dealing with multilayered or composite media, where metals and dielectrics coexist within the same effective region.

This law enables the estimation of how the refractive index varies when a metallic nanostructure is embedded within a dielectric host or when multiple dielectric layers are stacked.

In simple terms, Slater's Law helps predict the effective dielectric constant, ε_{eff}, of a heterogeneous medium using a weighted average of its constituents' dielectric constants. Mathematically, it can be expressed as:

$$\varepsilon_{\text{eff}} = f_1\varepsilon_1 + f_2\varepsilon_2 + f_3\varepsilon_3 + \cdots \tag{7.3}$$

Here, ε_{eff} denotes the effective permittivity of the composite medium, ε_i represents the permittivity of each component, and f_i is the corresponding volume fraction, where $\sum_i f_i = 1$.

In terms of refractive index, the same relationship can be written as:

$$n_{\text{eff}} = f_1 n_1 + f_2 n_2 + f_3 n_3 + \cdots \tag{7.4}$$

In plasmonic structures such as metal–insulator–metal (MIM) sensors, the electromagnetic field often penetrates through both metallic and dielectric regions. Therefore, the effective refractive index experienced by surface plasmon polaritons (SPPs) depends on both materials. Using Slater's Law, one can approximate this combined refractive index and understand how variations in dielectric thickness, metallic fraction, or material substitution influence the propagation characteristics of the guided plasmonic mode.

This relationship is particularly valuable during the design and optimization stage of plasmonic sensors, as it allows for quick estimation of the optical response without the need for full-wave simulation every time a material parameter changes. Although it is an approximation and does not account for all field interactions at nanoscale boundaries, Slater's Law provides an essential foundation for evaluating the dispersion and coupling strength between metal and dielectric regions before conducting rigorous numerical analysis [109].

7.4 Sensitivity

Sensitivity measures how strongly the resonance wavelength responds to a change in the surrounding refractive index (RI). Using two operating points with indices n_1 and n_2 and resonance wavelengths λ_1 and λ_2,

$$S = \frac{\Delta\lambda_{\mathrm{res}}}{\Delta n} = \frac{\lambda_2 - \lambda_1}{n_2 - n_1} \quad [\mathrm{nm/RIU}]. \tag{7.5}$$

In differential form, $S = \mathrm{d}\lambda_{\mathrm{res}}/\mathrm{d}n$. High-$S$ devices produce larger spectral shifts per RIU, enabling easier discrimination of small index changes. From Slater's theorem, S is enhanced by high field overlap with the analyte region and by strong dispersion of the guided or plasmonic mode [110].

7.5 Full Width at Half Maximum (FWHM)

The Full Width at Half Maximum (FWHM) is an important parameter that quantifies the spectral sharpness or bandwidth of a resonance curve. In the context of plasmonic refractive index sensors, the FWHM represents the wavelength range over which the transmittance (or reflectance) signal remains at least half of its maximum value. It effectively measures how narrow or broad a resonance dip is and is directly related to the quality and selectivity of the resonance.

When light passes through a plasmonic sensor, the interaction between the waveguide mode and the resonator produces one or more dips in the transmittance spectrum. These dips correspond to resonant wavelengths, where strong coupling occurs between the guided mode and surface plasmon polaritons (SPPs). The depth and width of each dip reveal important information about energy confinement and losses within the structure.

To calculate the FWHM, two key quantities are first identified: the maximum transmittance ($T_{\max}$) and the minimum transmittance ($T_{\min}$) of the resonance curve. The midpoint transmittance value is then determined as

$$T_{\mathrm{mid}} = \frac{T_{\max} + T_{\min}}{2}. \tag{7.6}$$

This midpoint corresponds to the half-maximum level of the resonance. The wavelengths on the left and right sides of the resonance dip, denoted by λ_L and λ_R respectively, are then located such that

$$T(\lambda_L) = T(\lambda_R) = T_{\text{mid}}. \tag{7.7}$$

The Full Width at Half Maximum is defined as the difference between these two wavelengths:

$$\text{FWHM} = \lambda_R - \lambda_L. \tag{7.8}$$

A smaller FWHM indicates a sharper and more selective resonance, implying lower energy loss and better wavelength discrimination. Conversely, a larger FWHM corresponds to a broader resonance, often resulting from increased damping or material absorption in the metallic region [111].

7.6 Figure of Merit (FOM)

The Figure of Merit (FOM) serves as a key parameter for evaluating the overall performance of a refractive index sensor. It represents a combined measure of both sensitivity and spectral resolution, offering a more comprehensive assessment of the sensor's detection capability [112]. Mathematically, the FOM is defined as the ratio of the sensitivity (S) to the full width at half maximum (FWHM) of the resonance dip in the transmittance spectrum,

$$\text{FOM} = \frac{S}{\text{FWHM}} \quad [\text{RIU}^{-1}]. \tag{7.9}$$

7.7 Quality Factor

The quality factor, commonly known as the Q-factor, is a dimensionless parameter that characterizes the sharpness or selectivity of a resonance in a plasmonic sensor. It reflects how efficiently the resonator stores electromagnetic energy relative to the energy dissipated per cycle. A higher Q-factor indicates a narrower resonance bandwidth, implying lower energy loss and greater precision in detecting wavelength shifts. Mathematically, the Q-factor is defined as the ratio of the resonance wavelength to the full width at half maximum (FWHM) of the resonance dip,

$$Q = \frac{\lambda_{\text{res}}}{\text{FWHM}} = \frac{\omega_0}{\Delta\omega} \quad \text{(dimensionless)}. \tag{7.10}$$

Here, λ_{res} represents the resonance wavelength at which surface plasmon polaritons (SPPs) are most strongly coupled to the resonator, resulting in a standing-wave field pattern and a distinct dip in the transmittance spectrum. The narrower the dip (smaller FWHM), the higher the Q-factor, and consequently, the more sensitive and selective the sensor becomes in detecting refractive-index variations [113].

7.8 Use of Performance Metrics in This Research

In this research, three primary performance metrics have been employed to evaluate and compare the sensing capability of the proposed plasmonic structures: Sensitivity, Full Width at Half Maximum (FWHM), and Figure of Merit (FOM). The sensitivity quantifies the sensor's ability to detect small variations in the refractive index of the surrounding medium, expressed in nanometers per refractive index unit (nm/RIU). The FWHM measures the spectral width of the resonance dip at its half-maximum transmission level, providing insight into the sharpness of the resonance and the degree of energy confinement within the resonator. Finally, the FOM, defined as the ratio of sensitivity to FWHM, serves as a comprehensive indicator of overall sensing performance by accounting for both detection capability and spectral selectivity.

Chapter 8

Inverse Design

Inverse design is a computational methodology that reverses the conventional process of designing and simulating plasmonic sensors. This approach allows for systematic and automated exploration of different design spaces that would be intractable through trial and error.

Optimization of electromagnetic behavior can be achieved by inverse design, which plays a crucial role in modern plasmonic research, where the relationships between geometry, material properties, and optical response are highly nonlinear. It is particularly powerful in applications such as plasmonic refractive index sensors, optical filters, and metasurfaces [114].

8.1 Workflow

The inverse design process follows a structured computational workflow to design toward the desired electromagnetic performance. The key steps are outlined below.

8.1.1 Problem Setup and Target Definition

The process begins by initializing the required electromagnetic response of the system. This involves setting target quantities such as transmission spectra or field intensity distributions within a specified design domain. These targets are mathematically formulated as objective functions that quantify how closely a simulated response matches the desired outcome [11].

8.1.2 Design Domain Parameterization

Next, the design region is parameterized so that it can be mathematically manipulated during optimization. Two major strategies are used:

Shape-based parameterization: distinct geometric features (for example, ring radius, width, or gap distance) are represented as tunable variables [115].

Topology-based parameterization: the design domain is represented by a continuous field of material densities, often ranging from 0 to 1, that defines the local presence or absence of material [116].

8.1.3 Forward Simulation Model

A forward simulation model is then used to evaluate the electromagnetic response of a given design. This step numerically solves Maxwell's equations using high-accuracy solvers such as the Finite-Difference Time-Domain (FDTD) method, the Finite Element Method (FEM), or frequency-domain integral equation solvers.

The forward solver computes the electromagnetic fields, transmission, and reflection spectra for each simulation. To ensure physically accurate results, proper boundary conditions and mesh resolution are applied.

8.1.4 Objective Function Formulation

The optimization process is guided by an objective or cost function that quantifies how close the simulated output is to the target behavior. This function typically measures the difference between the desired and actual spectra, power transmission, or field intensity.

8.1.5 Gradient Evaluation (Adjoint or Direct)

Gradient-based optimization methods are typically employed for high-dimensional problems with many design variables. The efficiency of such methods depends on how the derivative of the objective function with respect to all design variables is computed.

Two main approaches exist:

Finite Difference Method: each variable is perturbed individually, and the forward problem is re-simulated to estimate the gradient numerically. This approach is simple but computationally expensive, requiring one simulation per variable.

Adjoint Method: only two simulations—the forward and adjoint problems—are required regardless of the number of variables. The adjoint simulation efficiently backpropagates the sensitivity of the objective function to all design parameters simultaneously. The adjoint approach is thus highly efficient and widely used in inverse photonics design [52].

8.1.6 Design Update and Optimization Loop

Once gradients are obtained, the optimization algorithm updates the design parameters to move toward the optimal solution. Each iteration involves three main steps: running the forward simulation, computing gradients (either by adjoint or direct methods), and updating the geometry or material field. The process continues until the objective function converges, indicated by minimal change in value or gradient magnitude between successive iterations.

8.2 Types of Inverse Design

Inverse design methods can be categorized according to how they represent geometry, compute gradients, and search for optimal solutions. The main approaches are as follows:

1. Shape-Based Inverse Design This method adjusts a small set of explicit geometric parameters, such as width, radius, or angle. It is suitable for problems with low dimensionality where intuition about geometry-performance relationships exists. Gradient-free algorithms such as genetic algorithms or simulated annealing are often used in this context [115].

2. Topology Optimization (Density-Based) In topology optimization, the structure is represented by a continuous material density field that can vary throughout the design region. This method allows for discovering entirely new, non-intuitive geometries by optimizing the material distribution itself. It is powerful for freeform design and enables subwavelength feature generation [116].

3. Level-Set-Based Inverse Design The level-set method defines the structure implicitly using a continuous scalar function, where the zero-level contour corresponds to the material boundary. This approach naturally handles changes in topology, such as merging or splitting regions, and produces smooth, well-defined interfaces during optimization.

4. Adjoint-Based Gradient Optimization This category utilizes the adjoint method to compute sensitivities of the objective function efficiently. Because it requires only two simulations regardless of the number of variables, it is well-suited for large and complex design problems. Adjoint-based optimization is one of the most computationally efficient inverse design techniques for photonics.

5. Heuristic-Based Inverse Design Heuristic methods, such as genetic algorithms, particle swarm optimization, or simulated annealing, search the design space stochastically. These methods do not require gradient information, making them robust against discontinuities or non-convex objective functions. However, they often require many iterations and are computationally slower.

6. Machine Learning-Based Inverse Design Machine learning approaches use data-driven models such as neural networks, variational autoencoders, or Gaussian processes to learn mappings between design parameters and optical responses. Once trained, these models can instantly predict structural parameters for new target spectra, dramatically reducing computational cost compared to iterative simulations.

7. Reinforcement Learning-Based Inverse Design Reinforcement learning (RL) treats the inverse design problem as a sequential decision-making task. An RL agent interacts with the simulation environment by adjusting design parameters step by step, receiving rewards based on how well the resulting performance matches the target. Over time, the agent learns an optimal policy that maximizes performance metrics such as sensitivity or figure of merit [69].

Chapter 9

Reinforcement Learning

Reinforcement Learning (RL) is a subdomain of machine learning where an agent learns to take actions in an environment to maximize a cumulative reward. Unlike supervised learning, RL does not depend on explicit input-output pairs. Instead, it operates through a process of exploration and feedback, allowing the agent to learn from interaction rather than instruction. The fundamental concept behind RL is trial-and-error learning: the agent explores different actions, observes their outcomes, and adapts its strategy based on the received rewards.

A crucial element of RL is the trade-off between *exploration* and *exploitation*. Exploration enables the agent to test new actions and discover potentially better strategies, whereas exploitation involves selecting actions that are already known to yield high rewards. The *epsilon-greedy* strategy is a popular technique used to balance these two aspects. In this approach, the agent randomly explores actions with probability ϵ and exploits its current knowledge by choosing the best-known action with probability $(1 - \epsilon)$. As training proceeds, ϵ decays over time, gradually shifting the agent's focus from exploration to exploitation and promoting convergence toward an optimal policy [117].

9.1 Key Components of Reinforcement Learning

Agent: The decision-making entity that interacts with the environment. It learns from experience, adapts its behavior, and selects actions to improve its policy over time [118].

Environment: The system or domain in which the agent operates. It responds to the agent's actions by producing new states and rewards, guiding the learning process.

State (s): A snapshot representing the current configuration of the environment. It provides all relevant information necessary for the agent to choose the next action.

Action (a): A decision made by the agent that influences the state of the environment. The set of possible actions may vary depending on the state.

Reward (r): A scalar feedback signal provided after performing an action. Positive rewards reinforce desirable actions, while negative rewards (punishments) discourage poor decisions.

Return (G): The total accumulated reward over time, often computed as a discounted sum of future rewards, which the agent seeks to maximize.

Policy (π): A mapping from states to actions that defines the agent's behavior. A deterministic policy selects a single action for each state, while a stochastic policy assigns probabilities to possible actions.

Value Function (V): Estimates the expected return from a particular state under a given policy, providing a measure of the state's long-term desirability.

Q-Function (Q): Also known as the action-value function, it estimates the expected return for taking a specific action in a given state and subsequently following a particular policy.

Episode: A complete sequence of states, actions, and rewards that ends in a terminal condition. Episodes structure the training process and allow periodic evaluation.

Termination: The end of an episode, triggered by achieving a goal, reaching a predefined number of steps, or encountering a terminal state.

Punishment: A negative reward used to penalize undesirable behavior. It accelerates convergence by explicitly defining the consequences of suboptimal actions.

9.2 Markov Decision Process (MDP)

The mathematical foundation of reinforcement learning is the *Markov Decision Process* (MDP), which models sequential decision-making in uncertain environments. An MDP is defined by a 5-tuple (S, A, P, R, γ), where:

- **States (S):** The set of all possible configurations the environment can occupy. Each state provides sufficient information for decision-making.
- **Actions (A):** The set of all feasible actions available to the agent at each state.
- **Transition Probability Function (P):** $P(s'|s, a)$ defines the probability of transitioning to state s' after taking action a in state s. It captures the stochastic dynamics of the environment.
- **Reward Function (R):** $R(s, a, s')$ gives the immediate scalar feedback for a transition from s to s' via action a, representing the desirability of that action.
- **Discount Factor (γ):** A value between 0 and 1 that determines the importance of future rewards. Lower γ emphasizes immediate gains, while higher γ promotes long-term reward accumulation.

The agent-environment interaction proceeds as follows:

1. The agent observes the current state $s \in S$.
2. It selects an action $a \in A$ according to its current policy π.
3. The environment transitions to a new state s' based on $P(s'|s, a)$.
4. The agent receives a reward $r = R(s, a, s')$.

This cycle repeats, forming trajectories of states, actions, and rewards. The objective is to find an optimal policy π^* that maximizes the expected discounted cumulative reward:

$$J(\pi) = \mathbb{E}\left[\sum_{t=0}^{\infty} \gamma^t R_t\right]$$

MDPs satisfy the *Markov Property*, meaning that the future depends only on the present state and action, not on the sequence of past events. This property enables algorithms to make optimal decisions using only current information, simplifying computation and enabling effective learning [119].

9.3 Q-Learning

Q-learning is a model-free, value-based RL algorithm that seeks to learn the optimal action-value function $Q(s, a)$ [120]. The framework of Q-learning is shown in Fig. 9.1. It operates by iteratively updating Q-values according to the rule:

$$Q(s,a) \leftarrow Q(s,a) + \alpha \left[r + \gamma \max_{a'} Q(s',a') - Q(s,a) \right]$$

where α is the learning rate, γ is the discount factor, r is the reward, s' is the next state, and a' is the next action. The optimal policy is then derived by choosing the action with the highest Q-value for each state:

$$\pi^*(s) = \arg\max_{a} Q(s,a)$$

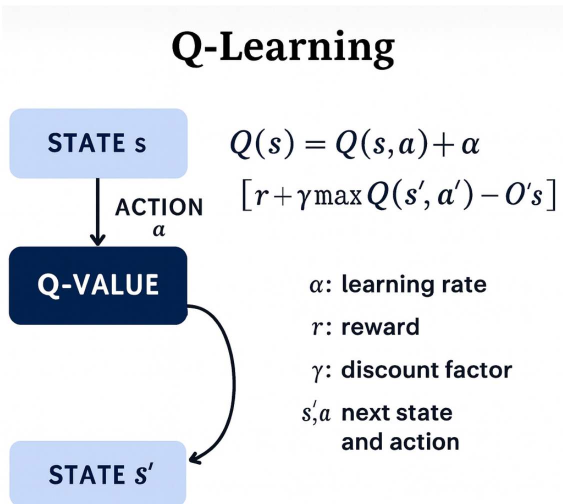

Fig 9.1: Q-Learning Framework

9.4 Policy Learning

A *policy* defines the mapping from states to actions, $\pi(s) = a$. In value-based approaches like Q-learning, the policy is implicit, derived from Q-values. In contrast, policy-based methods (such as Policy Gradient or Proximal Policy Optimization, PPO) represent the policy explicitly using parameterized functions. The objective is to maximize the expected return:

$$J(\theta) = \mathbb{E}[R|\pi_\theta]$$

where θ denotes the policy parameters. Deep Reinforcement Learning uses neural networks to approximate π_θ, which are optimized through gradient ascent to improve performance iteratively [121]. The framework of Q-learning is shown in Fig. 9.2.

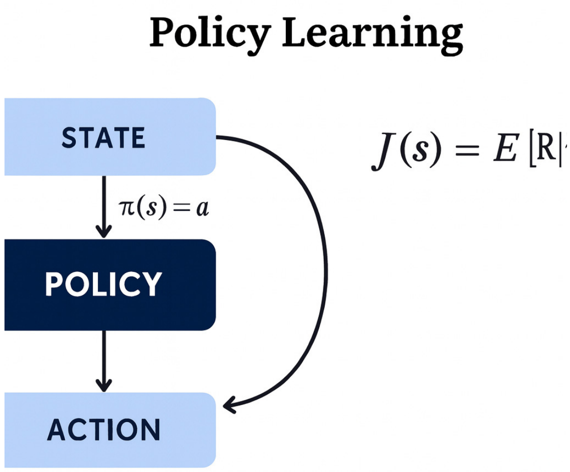

Fig 9.2: Policy-Learning Framework

9.5 Applying RL in Inverse Design for Plasmonic Sensors

Conventional photonic design relies on a forward methodology, where designers begin with an initial geometry, simulate its performance, and iteratively adjust parameters to reach a satisfactory result. This approach is both time-consuming and dependent on human expertise. In contrast, inverse design starts from a target performance metric such as maximizing sensitivity in a plasmonic sensor and seeks the geometry that fulfills that objective through algorithmic optimization.

Reinforcement Learning introduces a new paradigm to this process. In an RL-based inverse design framework, the agent autonomously explores geometric configurations and learns how to optimize performance through interaction with a simulation environment. For instance, the agent observes a current structure, modifies design parameters, and receives a reward based on the resulting sensitivity.

This approach is particularly suited for plasmonic refractive index sensors, where small geometric changes can significantly alter resonance behavior. The design space is inherently high-dimensional and nonlinear, including parameters such as the outer radius (R), ring width (w_2), gap (g), nanohole radius, and polygonal side count. RL enables efficient navigation of this complex design space by balancing exploration of new geometries with exploitation of high-performing configurations.

9.5.1 Mapping RL Concepts to the Plasmonic Inverse Design

- **Agent:** Implemented using a Deep Q-Network (DQN), the agent determines which design parameter to modify at each step. It takes the current geometry as input and outputs an optimal action.
- **Environment:** The simulation environment is constructed using Lumerical FDTD Solutions, which enables geometric updates, simulation execution, and reward computation.
- **State:** A vector representation of the current geometry, such as $[R, w_2, g, \text{thickness}, \text{hole\_radius}, \text{sides}]$.
- **Action:** A parameter modification applied to the structure.
- **Reward:** Defined based on sensitivity or a normalized function of the obtained sensitivity.

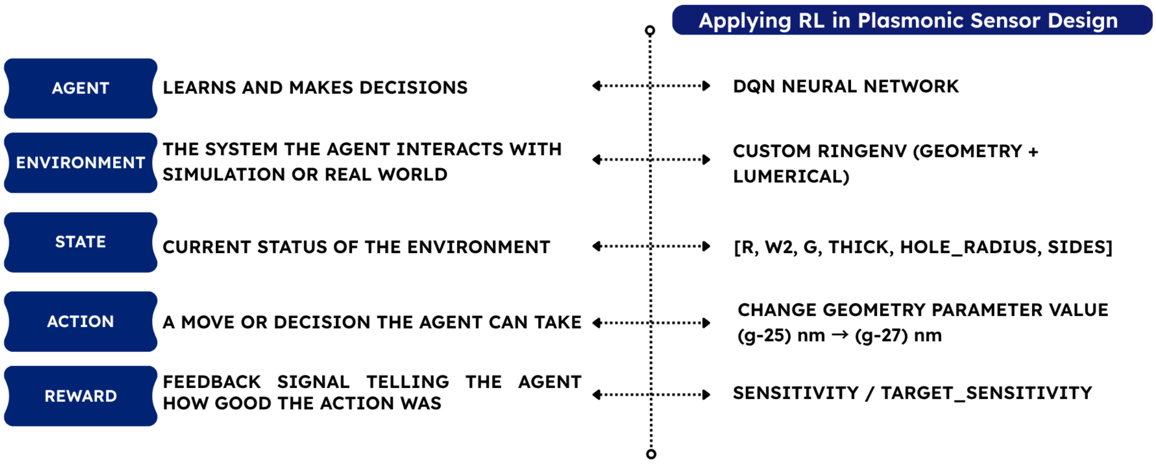

Fig 9.3: Mapping RL to Plasmonic Sensor Design

9.5.2 RL Pipeline in Plasmonic Inverse Design

1. **Defining the Environment:** Identify all tunable geometric and material parameters. Set bounds and constraints for each variable.

2. **Creating the Simulation Interface:** Develop a Python interface linking the RL agent to the FDTD simulator. This interface should handle geometry updates, simulation execution, and data retrieval.

3. **Selecting an RL Algorithm:** Choose an appropriate algorithm. Deep Q-Learning suits discrete action spaces, while Proximal Policy Optimization (PPO) or other actor-critic methods are better for continuous domains.

4. **Training Loop:** For each episode, the agent begins with an initial geometry, iteratively modifies design parameters, and updates its Q-values or policy based on observed rewards until termination.

5. **Evaluation and Post-Optimization:** After training, the final optimized structure is validated through simulation and compared to benchmarks for performance verification.

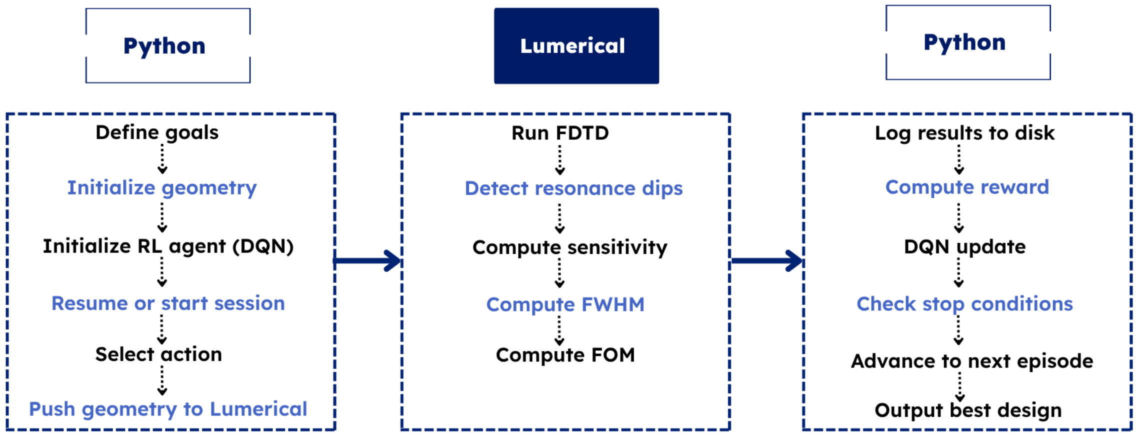

Fig 9.4: Flowchart of Python and Lumerical integration

9.6 RL Framework for Plasmonic Sensor Optimization

The proposed optimization method employs a Reinforcement Learning (RL) framework to autonomously guide the design process of highly sensitive plasmonic sensors. This framework integrates a neural network-based agent with a simulation-driven environment to iteratively optimize sensor geometry until the desired target sensitivity is achieved.

At the center of this system is the *Agent Neural Network (Agent NN)*, which receives as input a vector of geometric parameters representing the current design state. These parameters include radius, width, gap, thickness, hole size, and the number of polygonal sides. Together, they define the *state* of the environment. The agent processes this input through multiple hidden layers to evaluate a set of Q-values—each corresponding to a possible action it could take, such as increasing or decreasing a geometric parameter.

Based on the computed Q-values, the agent selects the action associated with the highest expected reward, i.e., the action that yields the largest Q-value. This selected action is then executed in the environment by modifying the geometric configuration of the plasmonic sensor.

The environment operates in two main stages:

1. **Change Geometric Parameter:** The selected action updates one of the geometric parameters of the design (for instance, adjusting the radius, gap, or thickness).

2. **Run Simulation in Lumerical:** The modified design is then passed to the simulation module in Lumerical FDTD, where the optical response of the structure is computed and the corresponding sensitivity is extracted.

Following the simulation, a reward is calculated to quantify how close the achieved sensitivity is to the target sensitivity. This reward serves as feedback for the agent, forming an experience tuple (s, a, r, s'), where s denotes the current state, a the executed action, r the received reward, and s' the new state resulting from the action. Using this feedback, the agent updates its Q-values, thereby refining its understanding of which actions lead to improved outcomes.

This feedback-driven learning loop continues over multiple episodes. With each iteration, the agent incrementally improves its policy, learning which parameter combinations maximize the plasmonic sensor's sensitivity. The optimization process terminates once the target sensitivity is reached or a convergence criterion is satisfied, at which point the framework outputs an optimized design configuration that achieves superior sensing performance.

Chapter 10

Re-simulation Results

In this chapter, we have re-simulated some well-known plasmonic refractive index sensor designs from existing literature using both FDTD and FEM-based tools. The main goal was to verify their performance, especially in terms of sensitivity and transmission behavior, and to check whether similar results could be reproduced in our setup. This also helped us to understand the working principles more clearly and gave a solid reference point for the optimization and inverse design work we did later.

10.1 Resimulation in COMSOL Multiphysics

10.1.1 Rahad *et al.* Sensor

The work by Rahad *et al.* introduced a refractive-index sensor employing a metal–insulator–metal (MIM) waveguide coupled to a rectangular ring resonator containing two silver baffles and a central nanorod. The design was investigated and optimized in COMSOL Multiphysics using the finite element method (FEM), where geometric parameters such as the baffle size, resonator width, and nanorod radius were tuned to strengthen field confinement and enhance coupling within the dielectric region. Through this optimization process, the device demonstrated a pronounced resonance shift with variation in the surrounding refractive index, yielding a maximum sensitivity of 2883.63 nm/RIU [30]. The configuration proposed by Rahad *et al.* is illustrated in Fig. 10.1, while the corresponding transmission spectrum is depicted in Fig. 10.2.

The resimulation in COMSOL Multiphysics successfully reproduced the structure proposed by Rahad *et al.* for refractive index sensing, incorporating a rectangular resonator with a silver nanorod and dual baffles. The electric field distribution confirms strong localization near the resonator cavity, indicating effective plasmon

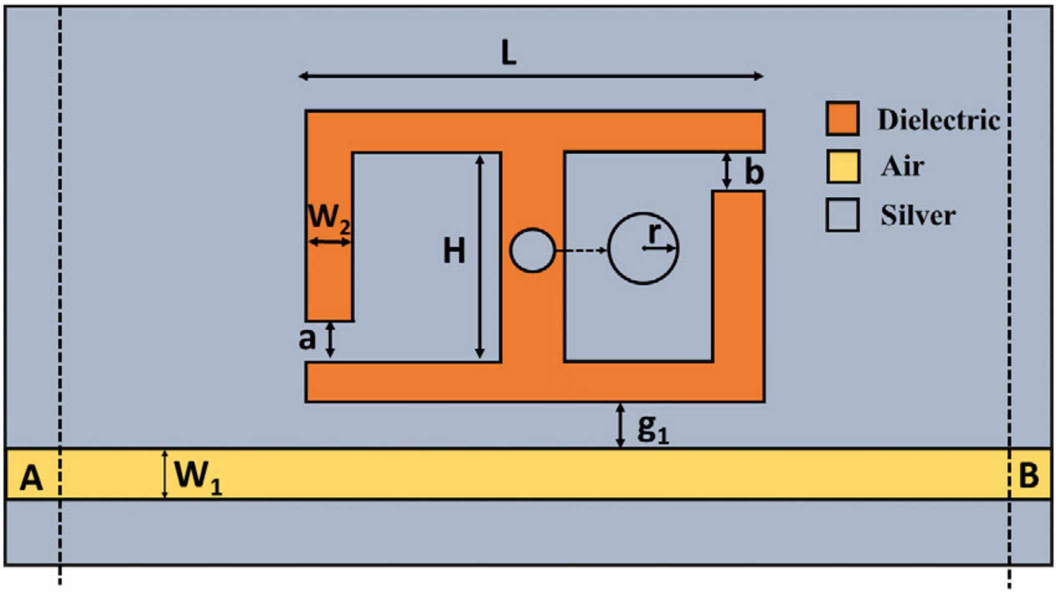

Fig 10.1: Proposed rectangular ring resonator structure by Rahad *et al.* [30]

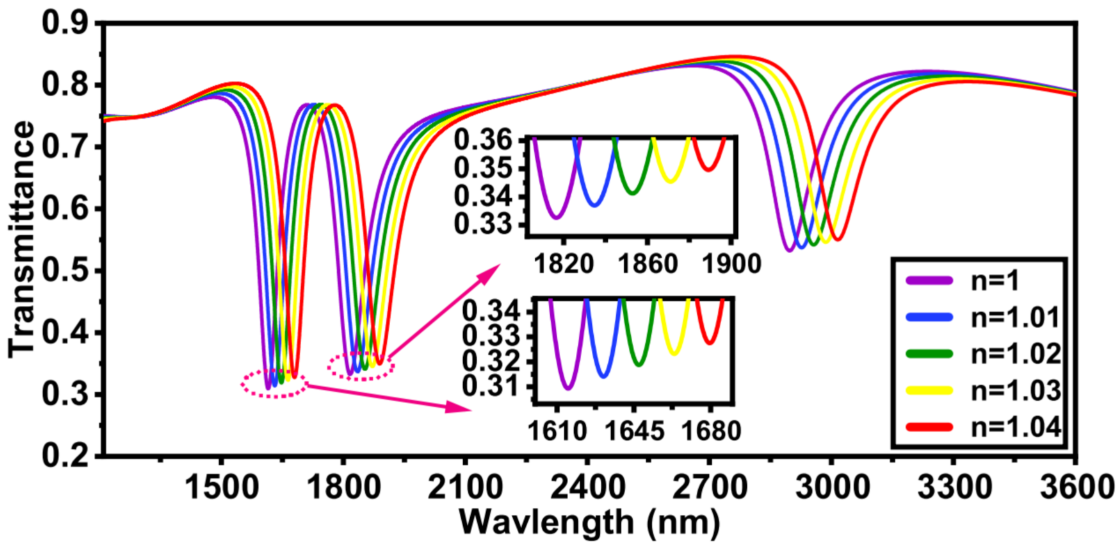

Fig 10.2: Original result obtained by Rahad *et al.* [30]

excitation. Most notably, the transmission spectrum reveals a substantial redshift in resonance wavelength as the refractive index increases from 1.00 to 1.04. The resulting maximum sensitivity, calculated from the slope of the wavelength shift versus refractive index, exceeds 2883.63 nm/RIU, which closely aligns with the original paper's reported performance. Fig. 10.3 shows the electric field distribution of the recreated structure, and Fig. 10.4 presents the transmittance–wavelength spectrum obtained from the resimulation.

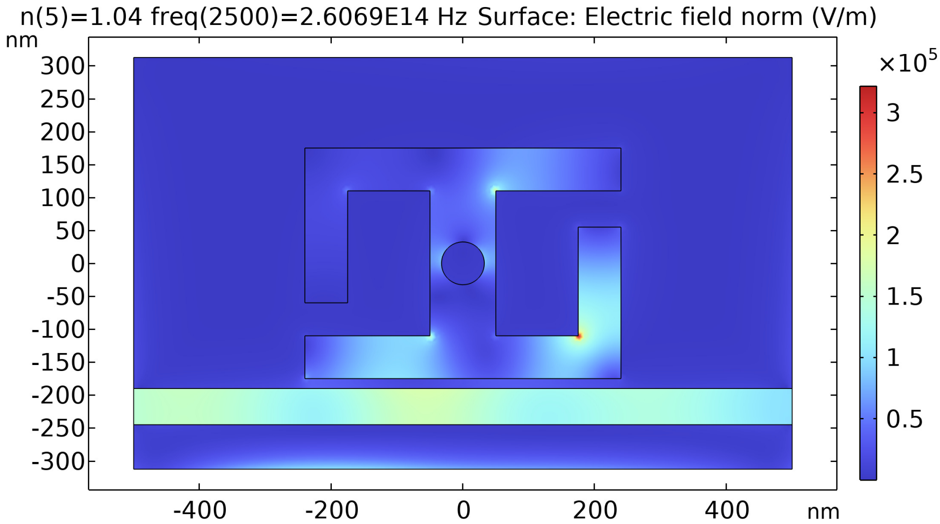

Fig 10.3: Electric field distribution of the recreated rectangular ring resonator structure in COMSOL Multiphysics.

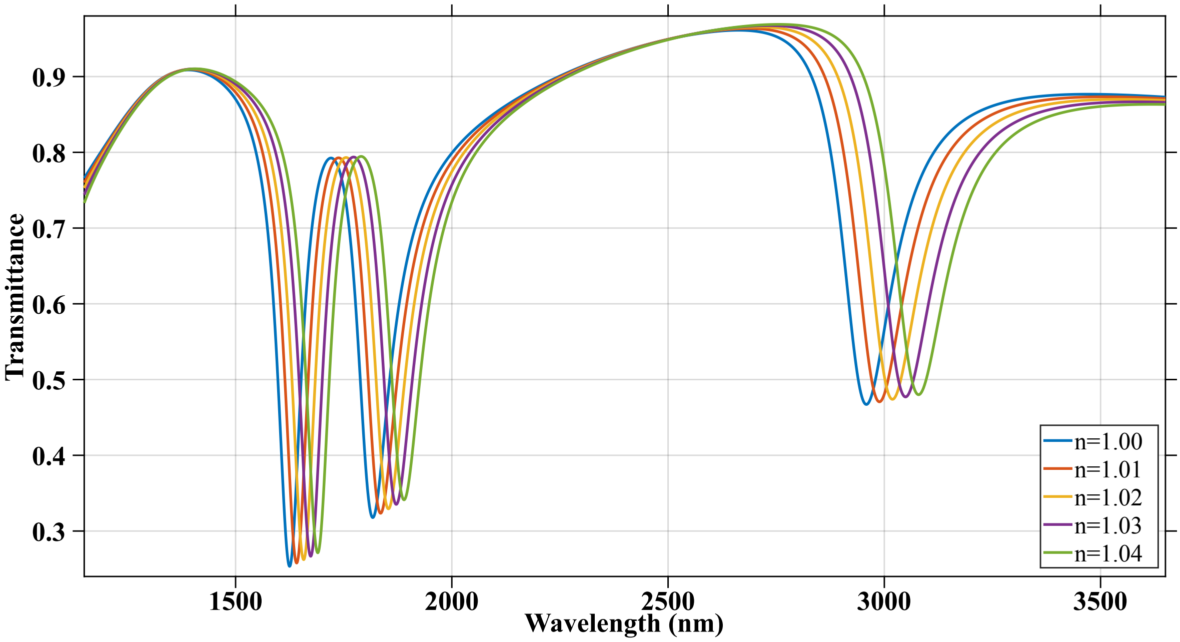

Fig 10.4: Transmittance versus wavelength spectrum obtained from COMSOL resimulation of the Rahad *et al.* sensor.

10.1.2 Al Mahmud *et al.* Sensor

The original study by Al Mahmud *et al.* introduced a plasmonic refractive index sensor featuring a metal–insulator–metal (MIM) waveguide coupled to a ring-type pentagonal resonator. By optimizing the resonator's geometric parameters—specifically the gap, ring width, and outer radius—the authors achieved high-performance metrics using FEM-based simulations in COMSOL Multiphysics. The sensor demonstrated strong electromagnetic confinement, leading to a notable redshift in the resonant wavelength in response to increasing refractive index values. As a result, the structure achieved a maximum sensitivity of 2325 nm/RIU with a corresponding FOM of 46 RIU^{-1} [25]. The structure proposed by Al Mahmud *et al.* is shown in Fig. 10.5, and their obtained wavelength–transmittance spectrum is presented in Fig. 10.6.

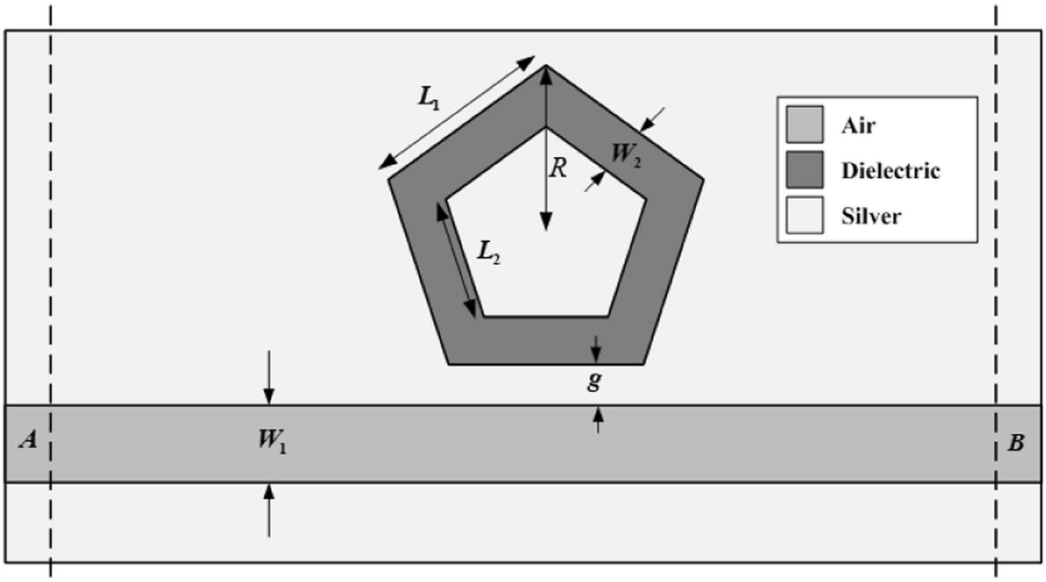

Fig 10.5: Proposed Pentagonal ring resonator sensor by Al Mahmud *et al.* [25]

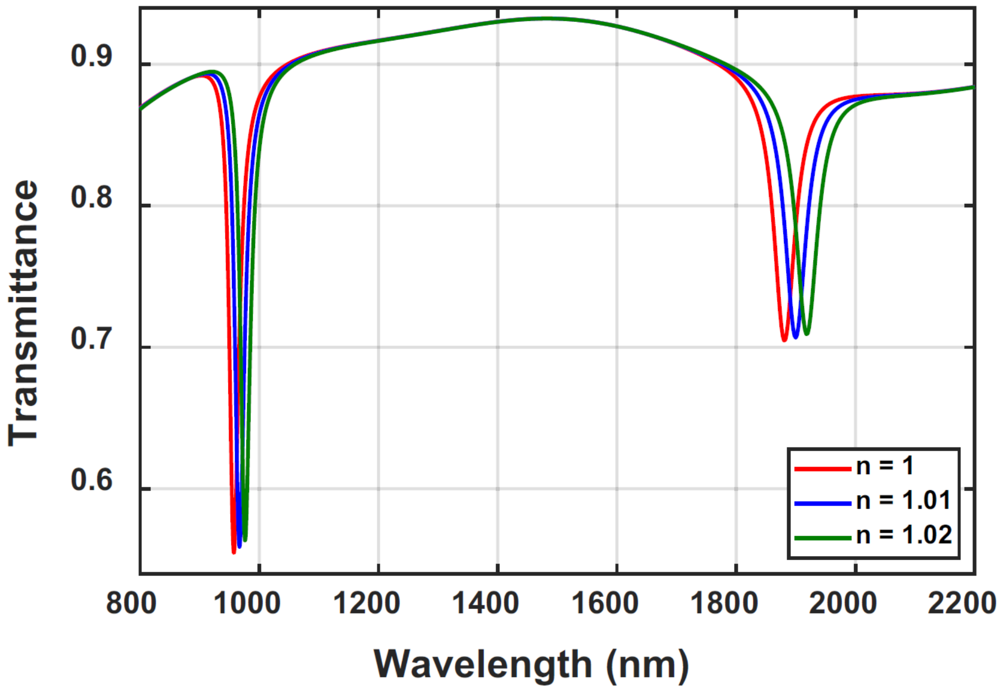

Fig 10.6: Original result obtained by Al Mahmud *et al.* [25]

In the resimulation of the design by Al Mahmud *et al.*, the pentagonal ring resonator was reproduced in COMSOL Multiphysics. The dielectric refractive index inside the cavity was varied, and the resulting transmission spectrum exhibited a linear redshift similar to the original study. The maximum sensitivity obtained was 2325 nm/RIU, aligning well with the reported result. Fig. 10.7 illustrates the simulated electric-field profile, while Fig. 10.8 shows the corresponding transmittance–wavelength response.

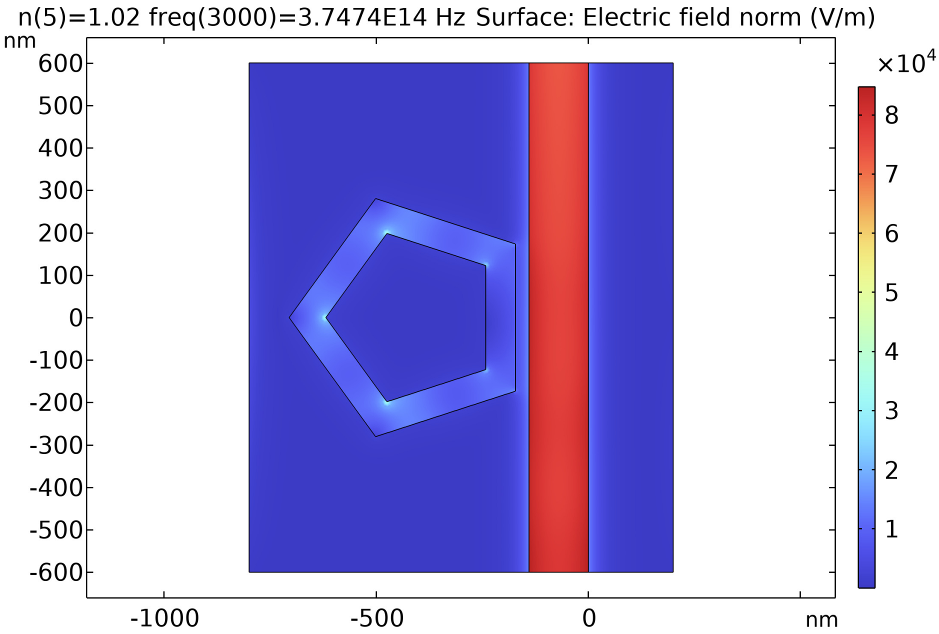

Fig 10.7: Electric field distribution of the recreated pentagonal ring resonator structure in COMSOL Multiphysics.

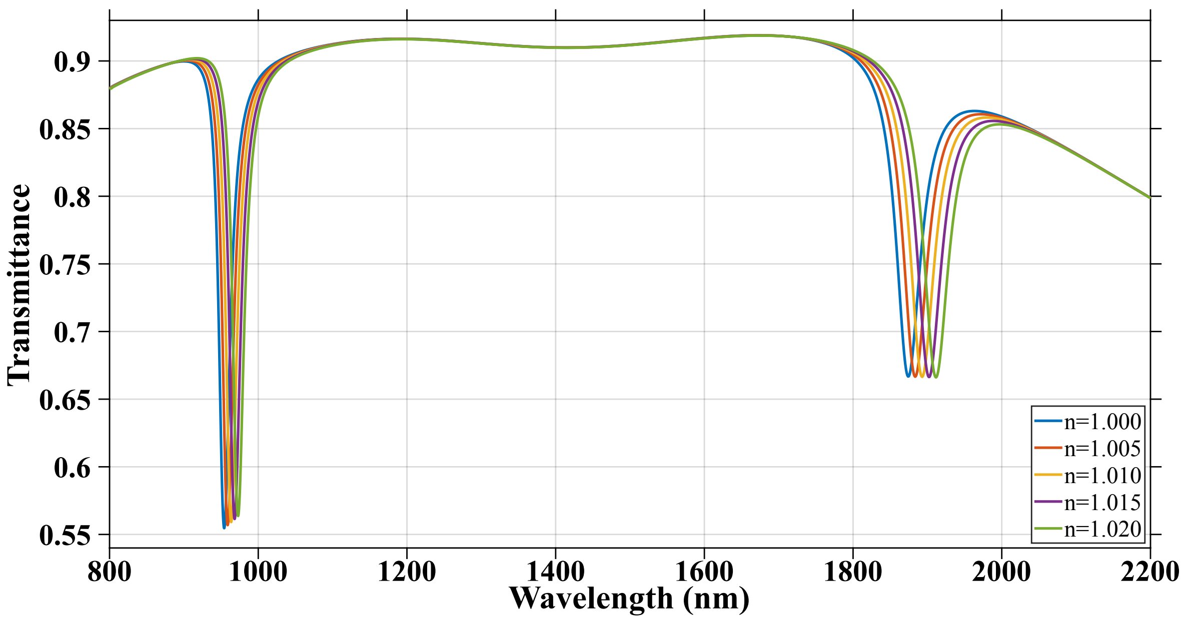

Fig 10.8: Transmittance versus wavelength spectrum obtained from COMSOL resimulation of the Al Mahmud *et al.* sensor.

10.2 Resimulation in Lumerical FDTD

10.2.1 Al Mahmud *et al.* Sensor

The structure proposed by Al Mahmud *et al.* [25] was also resimulated using the Lumerical FDTD method, where a full 3D model was constructed to enhance physical accuracy. Unlike the original FEM-based simulation in COMSOL, which used a 2D approximation assuming the device height to be greater than 800 nm, this resimulation included the complete z-dimension, addressing vertical field components and edge effects more precisely. As a result, while the spectral profile remained consistent, a slight variation in the sensitivity value was observed—yielding a peak sensitivity of **2155.98 nm/RIU**, whereas the sensitivity obtained from the Lumerical FDTD resimulation was **2325 nm/RIU**. This discrepancy is attributed to dimensional and meshing differences between the 2D FEM and 3D FDTD simulations, aligning with findings reported by Danaie *et al.* [39] regarding the impact of height on effective refractive index calculations. Fig. 10.9 shows the 3D structure of the pentagonal resonator sensor constructed in Lumerical FDTD, while Fig. 10.10 presents the transmittance–wavelength spectrum obtained from the resimulation.

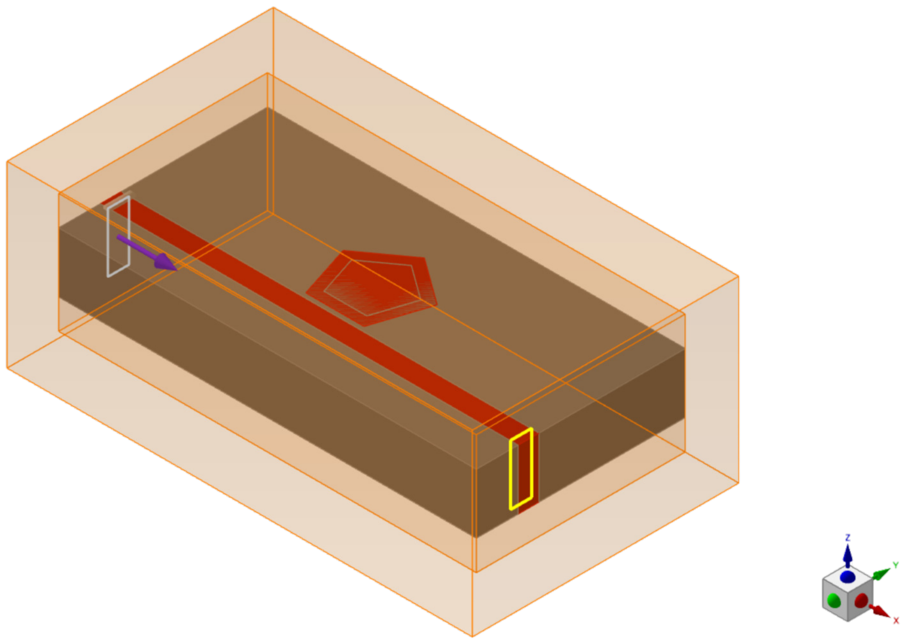

Fig 10.9: 3D structure of the pentagonal ring resonator sensor modeled in Lumerical FDTD.

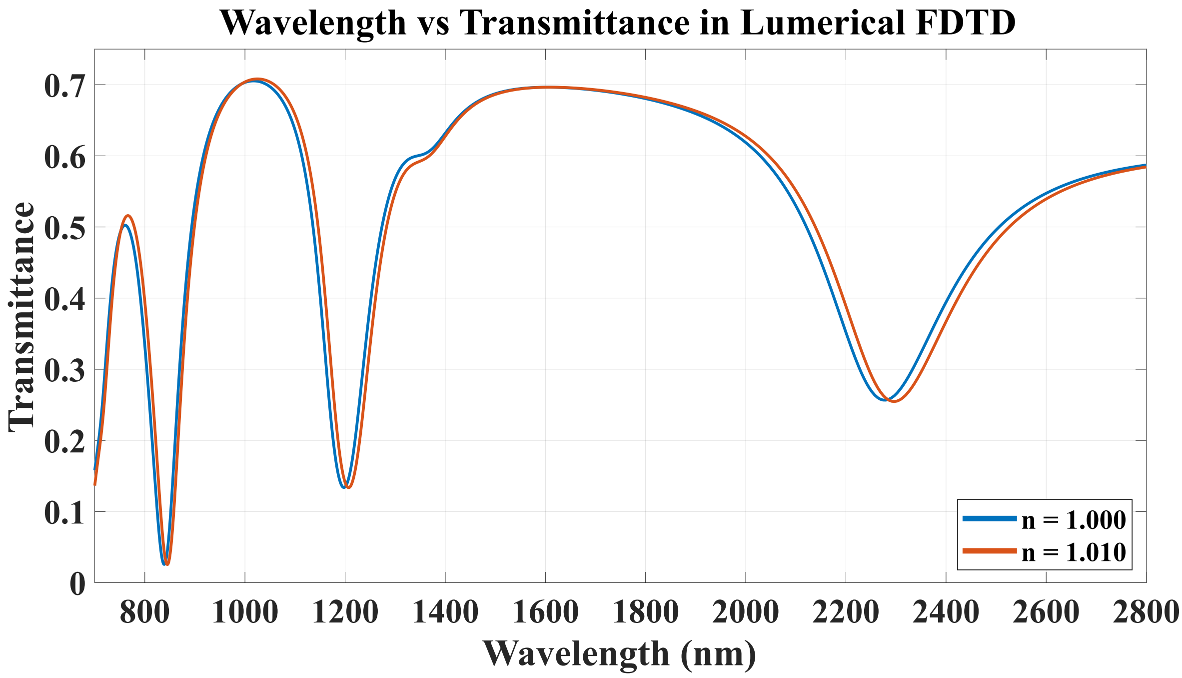

Fig 10.10: Transmittance–wavelength spectrum obtained from the resimulation of the Al Mahmud *et al.* structure in Lumerical FDTD.

10.2.2 Automation and Scripting in Lumerical FDTD

Following the resimulation of the Al Mahmud *et al.* sensor, it was observed that Lumerical FDTD produced slight variations in results compared to finite-element platforms such as COMSOL. However, its scripting interface offers major advantages in flexibility, repeatability, and optimization. Instead of relying on the graphical interface, the scripting environment enables full automation of simulations, making it ideal for iterative and parametric optimization in inverse design. Through scripting, geometric and simulation parameters can be modified programmatically, including the number of polygonal sides, nanorod placement, and cavity dimensions, along with mesh density and wavelength range. This automation minimizes human error, ensures consistent setups, and allows seamless integration with reinforcement-learning algorithms. In this research, scripting formed the foundation for inverse design, where the agent interacted with the simulator to modify geometry, run simulations, and evaluate metrics such as transmittance, resonance wavelength, sensitivity, and figure of merit. By combining precise electromagnetic modeling with programmable control, Lumerical FDTD scripting transforms the platform into a self-adaptive environment bridging conventional simulation and intelligent design. Table 10.1 illustrates how this scripting capability can generate plasmonic resonator structures by varying geometric parameters such as polygonal sides and nanorod count.

Table 10.1: Structures created in Lumerical FDTD by varying number of sides and nanorods.

Polygonal Ring Resonator	**Polygonal Ring Resonator with Nanorods**
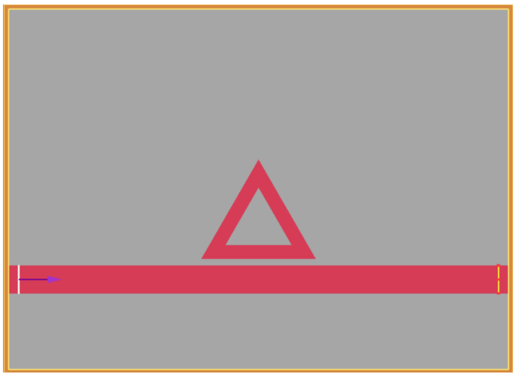	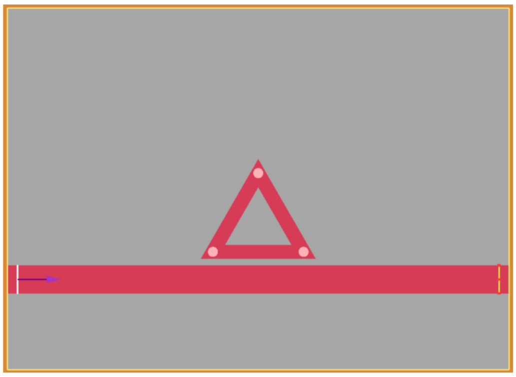
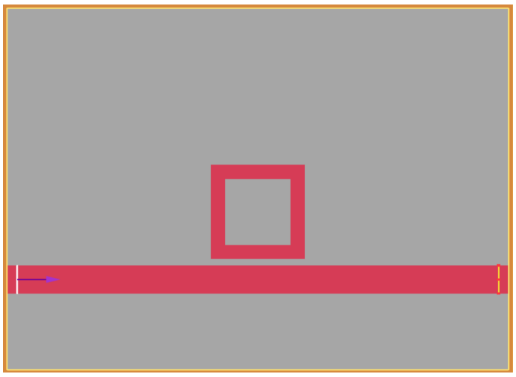	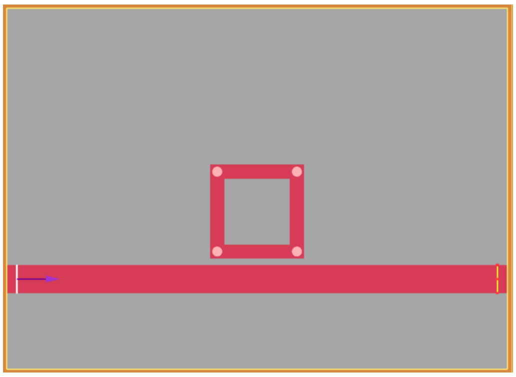
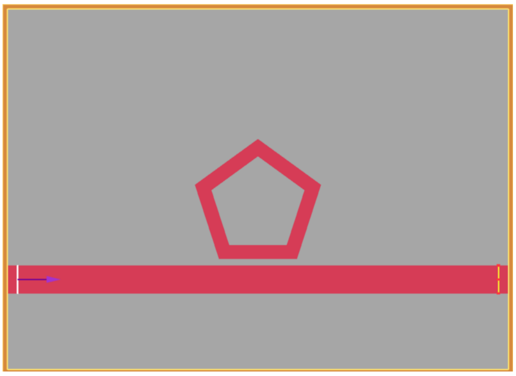	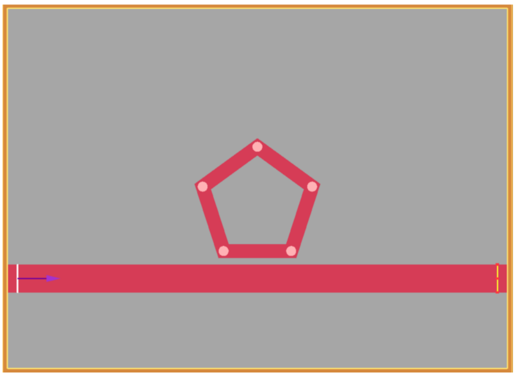
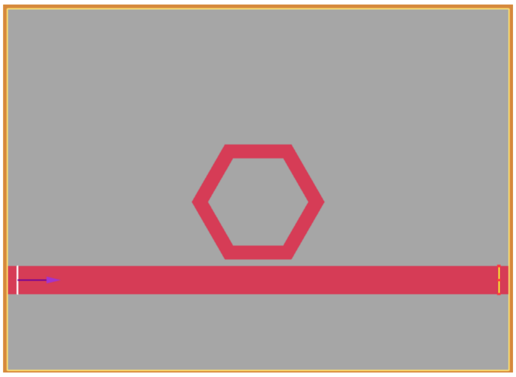	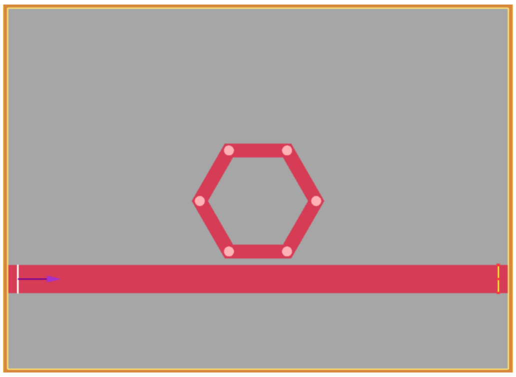

Continued on next page

Polygonal Ring Resonator	**Polygonal Ring Resonator with Nanorods**
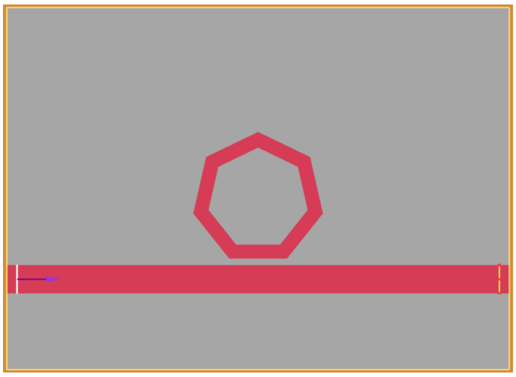	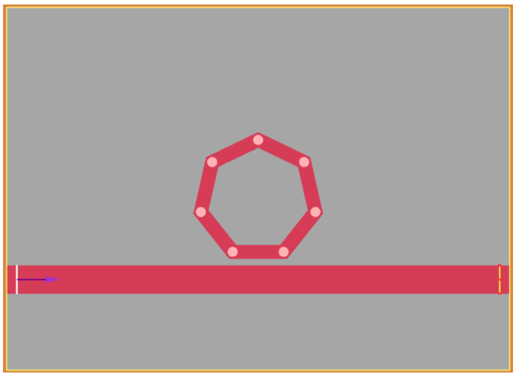
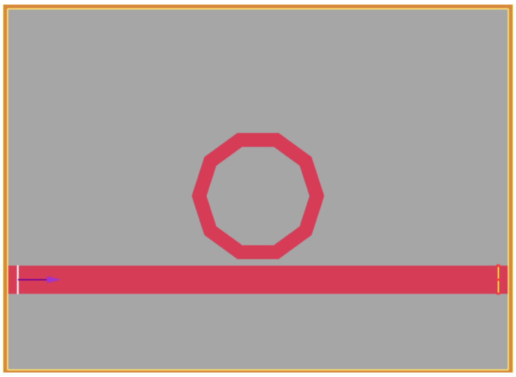	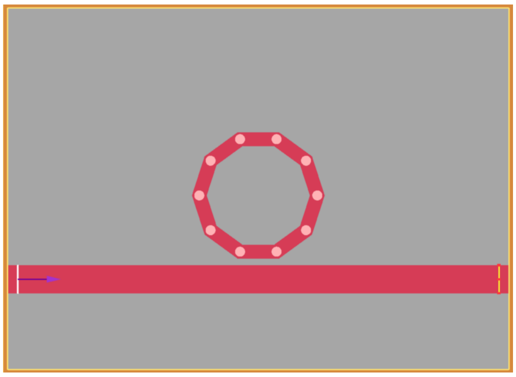
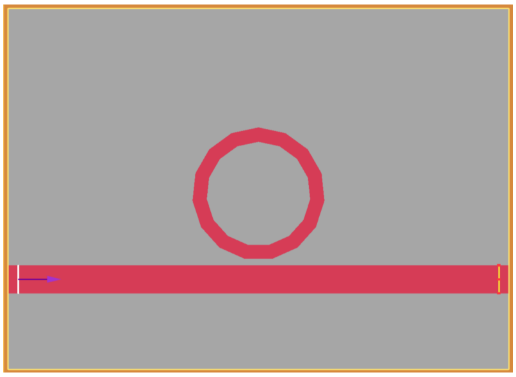	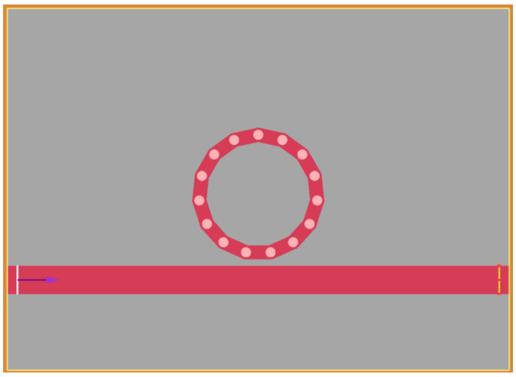
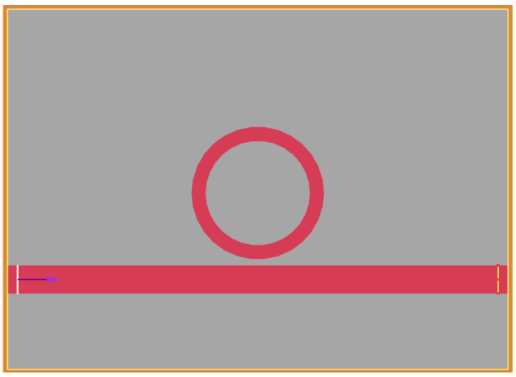	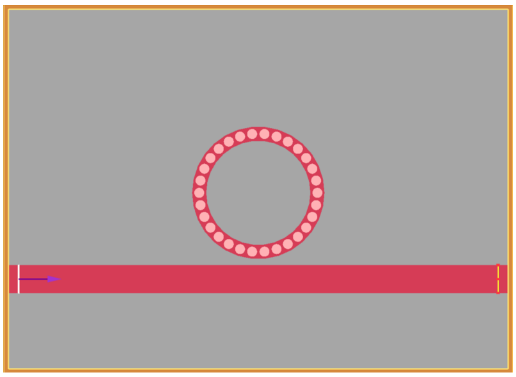

Chapter 11

Optimization Results

11.1 Optimization Based on Sensitivity

The reinforcement-learning-based inverse design optimization was initiated using a pentagonal ring resonator integrated into a metal–insulator–metal (MIM) waveguide system. Initially, four geometric parameters were defined: radius of the pentagon, width of the resonator, gap between the sensor and waveguide, and thickness of the sensor. Before optimization, the structural parameters were set as follows: gap = 32 nm, pentagon radius = 331 nm, and resonator width = 70 nm, with standard metal-layer thickness applied. The reinforcement learning (RL) agent was assigned a target sensitivity of 2000 nm/RIU and trained for 10 episodes, each consisting of up to 20 steps. As training progressed, the agent effectively explored the design space and identified an improved configuration that achieved a peak sensitivity of 2319.45 nm/RIU—representing a notable enhancement over the unoptimized pentagonal resonator, which exhibited 2155.98 nm/RIU. Table 11.1 lists the parameter values after optimization, while Fig. 11.1 illustrates the progressive improvement in sensitivity across episodes and steps.

Table 11.1: Optimization result for pentagonal ring resonator.

Parameter	**Optimized Value**
Radius of pentagon	326 nm
Width of resonator	66 nm
Gap between sensor and waveguide	35 nm
Thickness of sensor	400 nm
Sensitivity	2319.45 nm/RIU

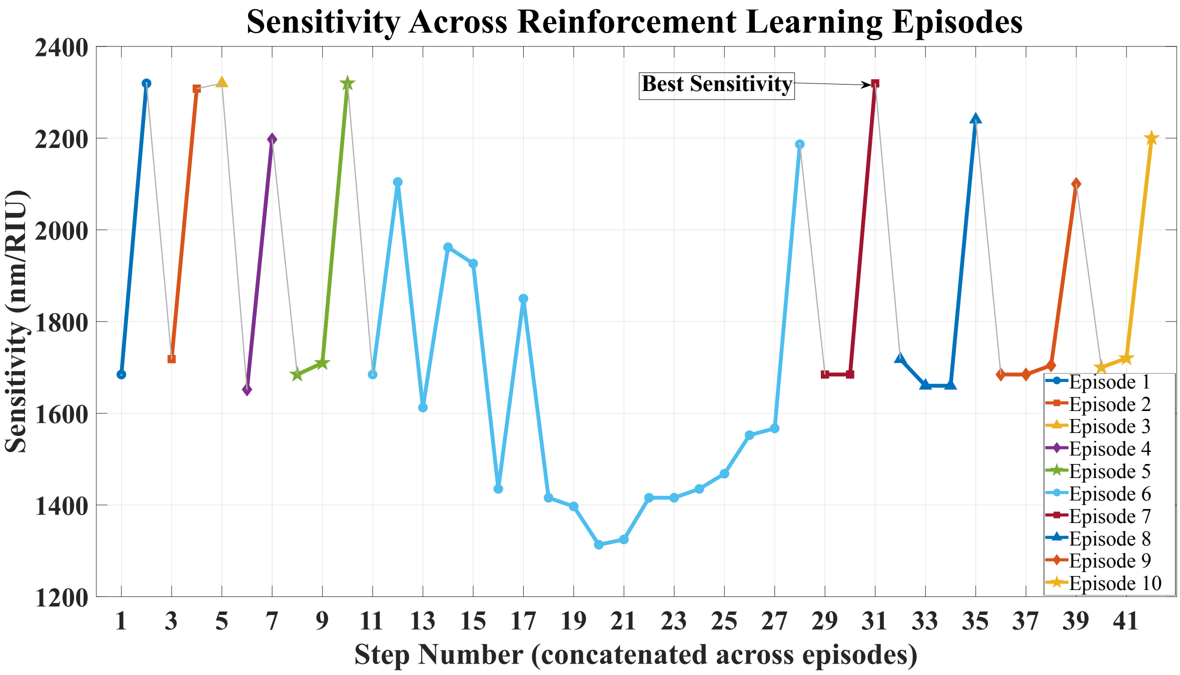

Fig 11.1: Sensitivity improvement trend during RL based optimization of the pentagonal ring resonator.

In the next phase, the optimization process was extended by introducing nanorods into the structure. The radius of each nanorod was incorporated as an additional tunable parameter, providing a higher degree of freedom in the design space. To examine the adaptability of the RL agent under tighter constraints, the number of training episodes was reduced to five, with each episode consisting of up to ten steps. Even within this shorter learning duration, the RL agent successfully converged to an optimized configuration that achieved a peak sensitivity of 2580.20 nm/RIU. This outcome demonstrated that fine-tuning the nanorod geometry further enhanced field confinement and resonance performance of the plasmonic structure. The optimized parameter values are summarized in Table 11.2, while the progression of sensitivity across episodes and steps is illustrated in Fig. 11.2.

Table 11.2: Optimization result for pentagonal ring resonator with nanorod.

Parameter	**Optimized Value**
Radius of pentagon	331 nm
Width of resonator	70 nm
Gap between sensor and waveguide	35 nm
Radius of nanorod	34 nm
Thickness of sensor	400 nm
Sensitivity	2580.20 nm/RIU

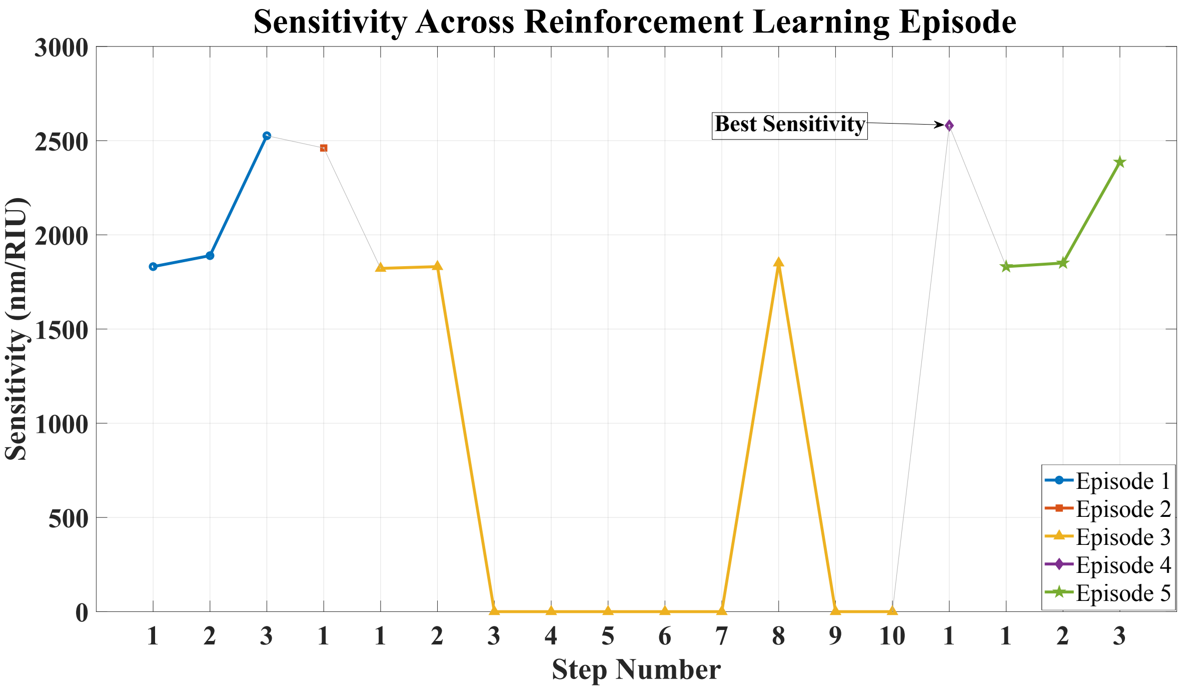

Fig 11.2: Sensitivity improvement trend during RL based optimization of the pentagonal ring resonator with nanorod.

Finally, the design flexibility was further extended by allowing the RL agent to vary the number of sides of the polygonal resonator. Starting from the previously optimized pentagonal form, the agent was free to explore alternative geometries. Along with the previous parameters, the number of sides was introduced as an additional tunable parameter. The training configuration remained the same, while the target sensitivity was slightly increased to 2500 nm/RIU. During optimization, the structure evolved from a pentagonal to an octagonal resonator, achieving a peak sensitivity of 2814.45 nm/RIU. This represented the highest performance attained in the entire sequence of optimization experiments. The optimization result is shown in Fig. 11.3, and the optimized parameters are listed in Table 11.3.

Table 11.3: Optimization result for pentagonal ring resonator with taking number of sides also as a tunable parameter.

Parameter	**Optimized Value**
Radius of pentagon	331 nm
Width of resonator	70 nm
Gap between sensor and waveguide	35 nm
Radius of nanorod	34 nm
Thickness of sensor	400 nm
No of sides	8
Sensitivity	2814.45 nm/RIU

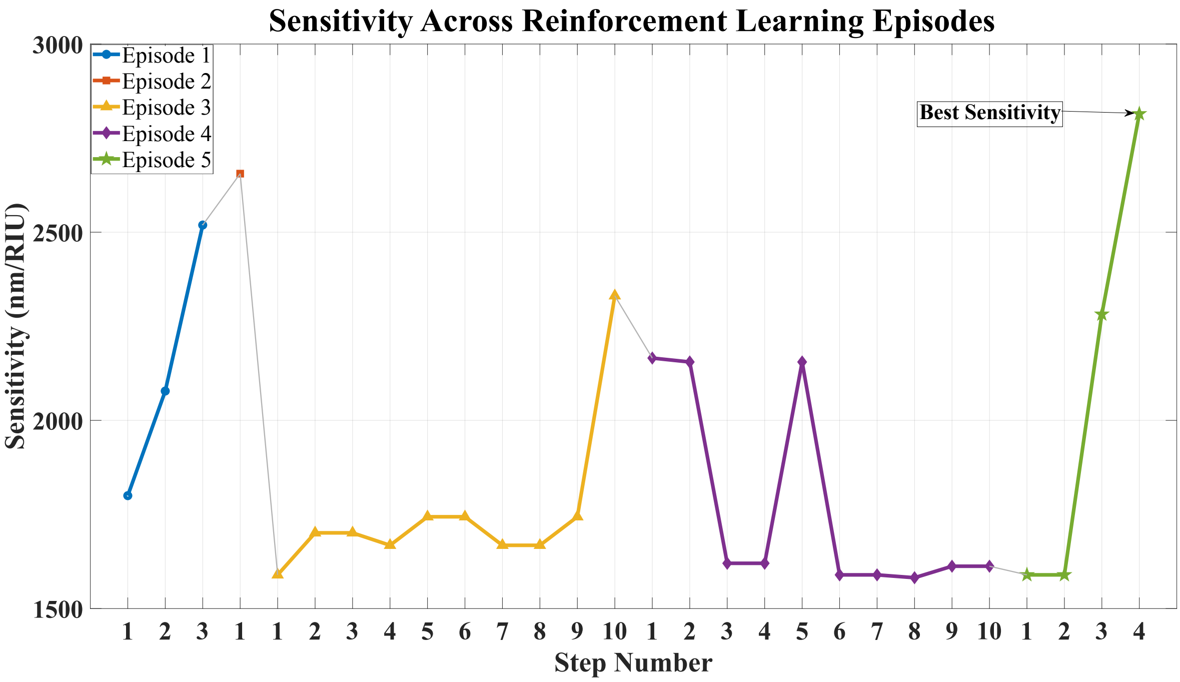

Fig 11.3: Sensitivity improvement trend during RL based optimization of the pentagonal ring resonator with nanorod and variable polygonal sides.

11.2 Optimization Based on Sensitivity and FOM

As discussed in Section 11.1, the reinforcement learning (RL) reward was computed solely based on the achieved sensitivity. In the next stage, the reward formulation was extended to include both Sensitivity and Figure of Merit (FOM) as performance indicators. The scoring function for the RL agent was defined as a weighted combination of these two objectives, as expressed in Eq. 11.1.

$$\text{Score} = 0.6 \times \left(\frac{\text{Sensitivity}}{\text{Target}_S}\right) + 0.4 \times \left(\frac{\text{FOM}}{\text{Target}_F}\right) \tag{11.1}$$

where the target values were set as:

$$\text{Target}_S = 2000 \text{ nm/RIU}, \quad \text{Target}_F = 8.00 \text{ RIU}^{-1}.$$

This weighted reward function encourages the agent to simultaneously maximize both sensitivity and FOM, balancing spectral selectivity with refractive index responsiveness.

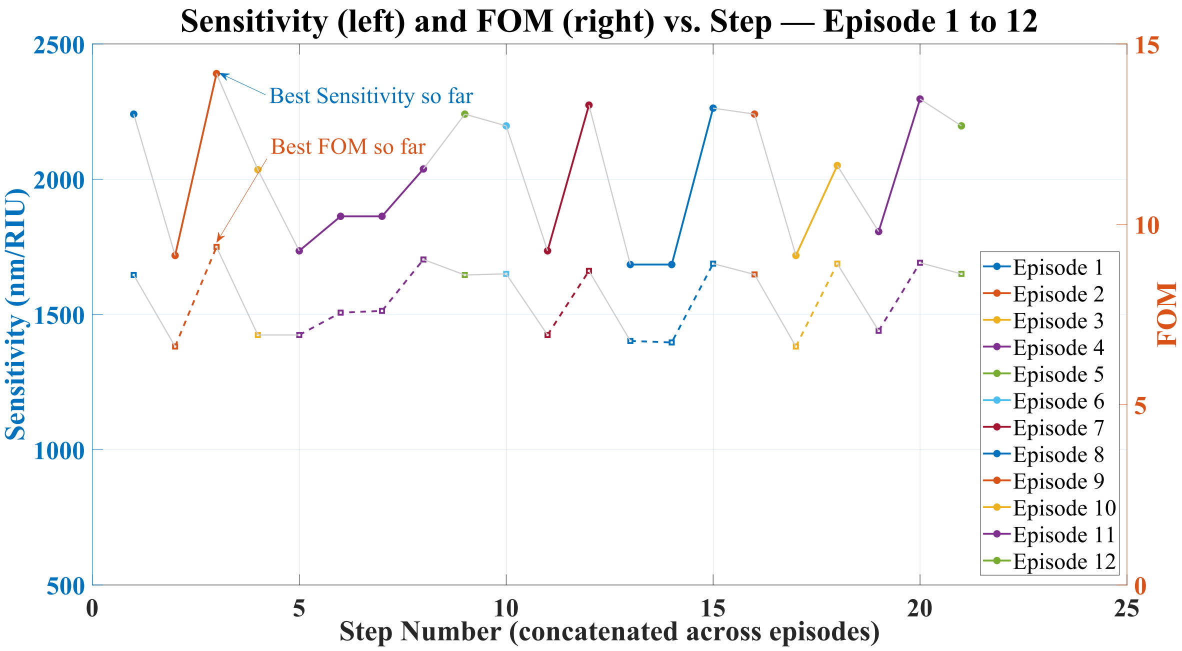

Fig 11.4: Sensitivity and figure of merit (FOM) improvement trend during early optimization episodes (1–12).

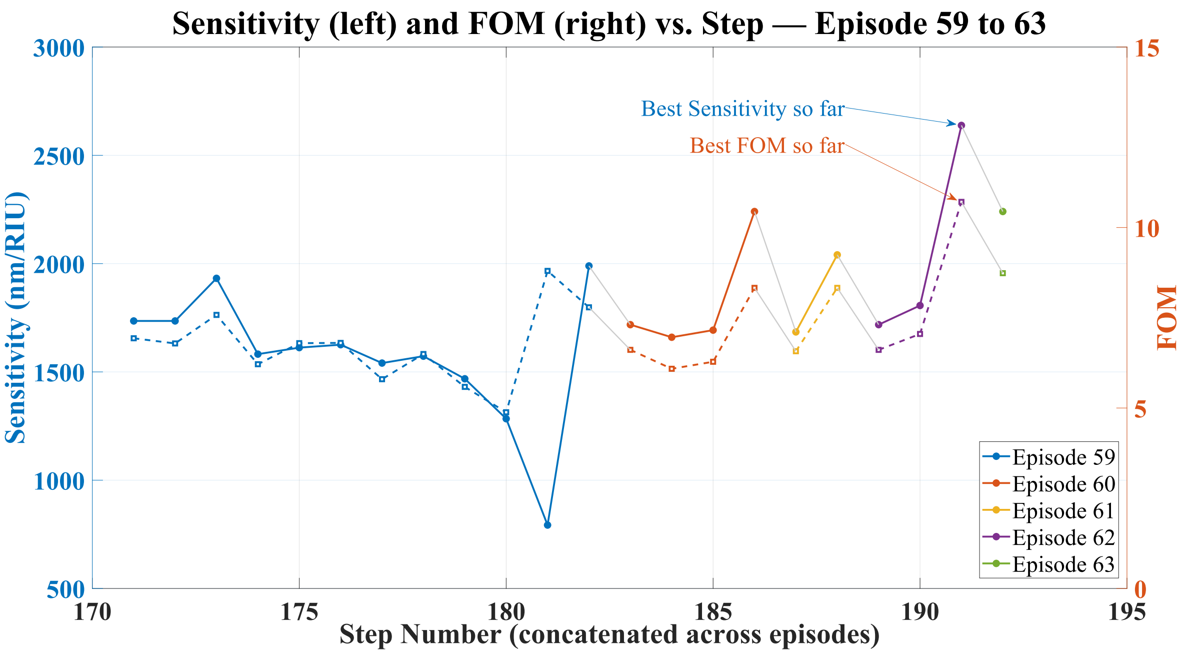

Fig 11.5: Sensitivity and figure of merit (FOM) progression during later optimization episodes (59–63).

In this phase, the optimization was conducted over an extended training duration of 70 episodes to allow deeper exploration of the design space. The performance progression for both sensitivity and figure of merit (FOM) during the early episodes (1–12) is illustrated in Fig. 11.4, while the improvement trends observed in the later episodes (59–63) are presented in Fig. 11.5. In this stage, the tunable geometric parameters included the radius of the resonator, resonator width, gap between the sensor and waveguide, sensor thickness, and the number of sides of the polygonal structure. The optimized parameter values obtained in these two optimization phases are summarized in Table 11.4.

Table 11.4: Optimization result for pentagonal ring resonator with taking number of sides also as a tunable parameter (two-stage comparison).

Parameter	**Optimized Value(Stage 1)**	**Optimized Value(Stage 2)**
Radius of resonator	336 nm	341 nm
Width of resonator	70 nm	66 nm
Gap between sensor and waveguide	32 nm	34 nm
Radius of nanorod	34 nm	34 nm
Thickness of sensor	400 nm	415 nm
Number of sides	6	5
Sensitivity	2390.45 nm/RIU	2638.15 nm/RIU
FOM	9.37 RIU^{-1}	10.71 RIU^{-1}

Chapter 12

Demonstration of Outcome Based Education (OBE)

The Outcome Based Education (OBE) framework builds both theoretical understanding and practical competencies required for real-world engineering. This thesis project, conducted under EEE 4700/4800 (Project and Thesis), reflects the application of OBE principles through structured problem solving, design thinking, and disciplined research—from selecting a relevant problem to simulation and optimization—while addressing the targeted Course Outcomes (COs) and Program Outcomes (POs).

This project designs and inversely optimizes plasmonic sensors based on metal–insulator–metal (MIM) structures to enhance refractive-index sensitivity. Lumerical FDTD is integrated with custom Python scripting and reinforcement-learning models to achieve advanced design and analysis objectives. Independent and team activities, data interpretation, and presentation of results were maintained throughout.

This chapter maps each activity and deliverable to the relevant COs, POs, and knowledge profiles, showing alignment with OBE objectives and readiness for professional practice and lifelong learning.

12.1 Introduction

The rapid evolution of modern industries, driven by the demand for compact, intelligent, and efficient devices, requires that engineering students develop skills to solve complex real-world problems. OBE plays a key role in this transformation by emphasizing measurable knowledge, analytical ability, and design competence.

EEE 4700/4800 (Project and Thesis) provides the platform to apply theoretical learning to practical research, aligning academic outcomes with professional needs. Through this thesis on inverse design of plasmonic sensors, challenges in photonic device optimization were addressed using machine learning. The process involved literature study, simulation, and experimentation, strengthening both technical and soft skills such as teamwork, critical thinking, and lifelong learning.

12.2 Course Outcomes (COs) Addressed

The following table shows the COs addressed in EEE 4700/4800 for Project and Thesis.

COs	**CO Statement**	**POs**	**Put Tick (✓)**
CO1	Apply knowledge of electrical and electronic engineering to the solution of complex engineering problems.	PO1	✓
CO2	Identify a contemporary real life problem related to electrical and electronic engineering by reviewing and analyzing existing research works.	PO2	✓
CO3	Determine functional requirements of the problem considering feasibility and efficiency through analysis and synthesis of information.	PO4	✓
CO4	Select a suitable solution and determine its method considering professional ethics, codes and standards.	PO8	✓
CO5	Adopt modern engineering resources and tools for the solution of the problem.	PO5	✓
CO6	Prepare management plan and budgetary implications for the solution of the problem.	PO11	✓
CO7	Analyze the impact of the proposed solution on health, safety, culture and society.	PO6	✓
CO8	Analyze the impact of the proposed solution on environment and sustainability.	PO7	✓
CO9	Develop a viable solution considering health, safety, cultural, societal and environmental aspects.	PO3	✓
CO10	Work effectively as an individual and as a team member for the accomplishment of the solution.	PO9	✓
CO11	Prepare various technical reports, design documentation, and deliver effective presentations for demonstration of the solution.	PO10	✓
CO12	Recognize the need for continuing education and participation in professional societies and meetings.	PO12	✓

12.3 Aspects of Program Outcomes (POs) Addressed

The following table shows the aspects addressed for certain Program Outcomes (POs) addressed in EEE 4700/4800 for Project and Thesis.

POs	Statement	Different Aspects	Put Tick (✓)
PO3	**Design/development of solutions:** Design solutions for complex electrical and electronic engineering problems and design systems, components or processes that meet specified needs with appropriate consideration for public health and safety, cultural, societal, and environmental considerations.	Public health	✓
		Safety	✓
		Cultural	
		Societal	
		Environmental	✓
PO4	**Investigation:** Conduct investigations of complex electrical and electronic engineering problems using research-based knowledge and research methods including design of experiments, analysis and interpretation of data, and synthesis of information to provide valid conclusions.	Design of experiments	✓
		Analysis and interpretation of data	✓
		Synthesis of information	✓
PO6	**The engineer and society:** Apply reasoning informed by contextual knowledge to assess societal, health, safety, legal and cultural issues and the consequent responsibilities relevant to professional engineering practice and solutions to complex electrical and electronic engineering problems.	Societal	
		Health	✓
		Safety	✓
		Legal	✓
		Cultural	
PO7	**Environment and sustainability:** Understand and evaluate the sustainability and impact of professional engineering work in the solution of complex electrical and electronic engineering problems in societal and environmental contexts.	Societal	
		Environmental	✓
PO8	**Ethics:** Apply ethical principles embedded with religious values, professional ethics and responsibilities, and norms of electrical and electronic engineering practice.	Religious values	✓
		Professional ethics and responsibilities	✓
		Professional codes and standards	✓
PO10	**Communication:** Communicate effectively on complex engineering activities with the engineering community and with society at large, such as being able to comprehend and write effective reports and design documentation, make effective presentations, and give and receive clear instructions.	Comprehend and write effective reports	✓
		Design documentation	✓
		Make effective presentations	✓
		Receive and give clear instructions	✓

POs	Statement	Different Aspects	Put Tick (✓)
PO11	**Project management and finance:** : Demonstrate knowledge and understanding of engineering management principles and economic decision-making and apply these to one's own work, as a member and leader in a team, to manage projects and in multidisciplinary environments.	Engineering management principles	✓
		Economic decision-making	✓
		Manage projects	✓
		Multidisciplinary environments	✓

12.4 Knowledge Profiles (K3 – K8) Addressed

The following table shows the Knowledge Profiles (K3 – K8) addressed in EEE 4700/4800 for Project and Thesis.

K	Knowledge Profile (Attribute)	Put Tick (✓)
K3	A systematic, theory-based formulation of engineering fundamentals required in the engineering discipline.	✓
K4	Engineering specialist knowledge that provides theoretical frameworks and bodies of knowledge for the accepted practice areas in the engineering discipline; much is at the forefront of the discipline.	✓
K5	Knowledge that supports engineering design in a practice area.	✓
K6	Knowledge of engineering practice (technology) in the practice areas in the engineering discipline.	✓
K7	Comprehension of the role of engineering in society and identified issues in engineering practice in the discipline: ethics and the engineer's professional responsibility to public safety; the impacts of engineering activity; economic, social, cultural, environmental and sustainability.	✓
K8	Engagement with selected knowledge in the research literature of the discipline.	✓

The following table explains or justifies how the Knowledge Profiles (K3–K8) have been addressed in EEE 4700/4800 (Project and Thesis).

K	Explanation/Justification
K3	The project applies **FDTD** simulations and optimization methods grounded in Maxwell's equations and computational electromagnetics.
K4	The study employs advanced knowledge of **Lorentz–Drude modeling** and plasmonic material behavior at the frontier of photonics.
K5	The iterative optimization of waveguide and resonator geometries reinforces the design principles of photonic engineering.
K6	Tools such as **Lumerical FDTD**, Python API, and material modeling illustrate key technological applications.
K7	The exploration of healthcare, environmental, and sustainability uses demonstrates societal and professional integration.
K8	The work engages with recent research, including **refractory materials** and **reinforcement-learning-based optimization**, to advance plasmonic sensor design.

12.5 Use of Complex Engineering Problems

The design and optimization of plasmonic refractive index sensors using reinforcement learning involved solving complex engineering problems that could not be addressed through straightforward analytical methods. The task required deep domain knowledge in electromagnetics, photonic structures, machine learning algorithms, and simulation tools. It included high dimensional parameter tuning, performance trade offs, and the integration of FDTD based simulation environments with intelligent agents. These challenges align with the attributes of complex problem solving, such as abstract thinking, originality in design, and synthesis of interdisciplinary knowledge, and required structured experimentation, data interpretation, and iterative refinement.

12.6 Socio-Cultural, Environmental, and Ethical Impact

The developed sensor technologies, while rooted in advanced computational design, have broader implications for society. Plasmonic sensors optimized for high sensitivity can be used in medical diagnostics, such as early detection of diseases like cancer or diabetes, promoting health and well-being. They can also aid in environmental monitoring by detecting impurities in water and air. The work promotes sustainable engineering practices by aiming for compact, material-efficient designs. Ethical considerations were maintained by ensuring scientific integrity, proper citation of research, and acknowledgment of computational limitations that could affect practical deployment or scalability. This thesis upholds values of social responsibility and environmental awareness within the engineering context.

12.7 Attributes of Ranges of Complex Engineering Problem Solving (P1–P7) Addressed

The following table shows the attributes of ranges of Complex Engineering Problem Solving (P1–P7) addressed in EEE 4700/4800 for Project and Thesis.

P **Attribute**	**Range of Complex Engineering Problem Solving** Complex Engineering Problems have characteristic P1 and some or all of P2 to P7:	**Put Tick (✓)**
Depth of knowledge required	**P1:** Cannot be resolved without in-depth engineering knowledge at the level of one or more of K3, K4, K5, K6 or K8 which allows a fundamentals-based, first principles analytical approach.	✓
Range of conflicting requirements	**P2:** Involve wide-ranging or conflicting technical, engineering and other issues.	
Depth of analysis required	**P3:** Have no obvious solution and require abstract thinking, originality in analysis to formulate suitable models.	✓
Familiarity of issues	**P4:** Involve infrequently encountered issues.	✓
Extent of applicable codes	**P5:** Are outside problems encompassed by standards and codes of practice for professional engineering.	✓
Extent of stakeholder involvement and conflicting requirements	**P6:** Involve diverse groups of stakeholders with widely varying needs.	
Interdependence	**P7:** Are high-level problems including many component parts or sub-problems.	✓

The following table explains or justifies how the attributes of ranges of Complex Engineering Problem Solving (P1–P7) have been addressed in EEE 4700/4800 (Project and Thesis).

P	**Explanation/Justification**
P1	The project requires knowledge of Electromagnetic Theory, Optimization Algorithms and Inverse Design, Material Properties, and Interdisciplinary Integration.
P2	
P3	The project includes designing non-intuitive structures, multiphysics modeling, and optimization under constraints.
P4	Issues arise from optimization in high-dimensional design spaces, material non-idealities, balancing competing metrics, and application-specific requirements.
P5	Challenges stem from the novelty of inverse design, emerging field of computational plasmonics, material and fabrication constraints, and integration of multidisciplinary knowledge with experimental/theoretical synergy.
P6	
P7	Different problems are aimed to solve during this project including a set of subproblems. Among the sub-problems, some of the most noticeable are Simulation and Modeling Sub-Problems, Optimization Challenges, Integration of Components, and Application-Specific Requirements.

12.8 Attributes of Ranges of Complex Engineering Activities (A1–A5) Addressed

The following table shows the attributes of ranges of Complex Engineering Activities (A1–A5) addressed in EEE 4700/4800 for Project and Thesis.

A **Attribute**	**Range of Complex Engineering Activities** Complex activities mean (engineering) activities or projects that have some or all of the following characteristics:	**Put Tick (✓)**
Range of resources	**A1:** Involve the use of diverse resources (and for this purpose resources include people, money, equipment, materials, information and technologies).	✓
Level of interaction	**A2:** Require resolution of significant problems arising from interactions between wide-ranging or conflicting technical, engineering or other issues.	✓
Innovation	**A3:** Involve creative use of engineering principles and research-based knowledge in novel ways.	✓
Consequences for society and the environment	**A4:** Have significant consequences in a range of contexts, characterized by difficulty of prediction and mitigation.	✓
Familiarity	**A5:** Can extend beyond previous experiences by applying principles-based approaches.	✓

The following table explains or justifies how the attributes of ranges of Complex Engineering Activities (A1–A5) have been addressed in EEE 4700/4800 (Project and Thesis).

A	**Explanation/Justification**
A1	The project uses advanced tools like **Lumerical FDTD** and Python APIs, along with computational resources for optimization. It also integrates interdisciplinary skills in plasmonics, materials science, and computational methods.
A2	The project tackles challenges in optimizing sensor designs, balancing sensitivity, fabrication feasibility, and environmental factors. Solving these requires advanced problem-solving skills and managing trade-offs.
A3	Creativity is applied by using sensitivity as the key optimization parameter, combining plasmonic principles with iterative techniques to discover efficient sensor geometries.
A4	The optimized design has societal benefits, such as improving healthcare diagnostics and environmental monitoring, while also considering practical constraints like fabrication tolerances and material availability.
A5	The project extends beyond previous experience by exploring the inverse design process, where new geometries are derived from desired sensitivity. This principles-based approach requires applying advanced optimization techniques, such as adjoint methods, to achieve the targeted outcomes.

Chapter 13

Conclusions

The reinforcement learning (RL)-based inverse design approach demonstrated a systematic enhancement in the sensitivity of plasmonic refractive index sensors through multiple optimization stages. Beginning with a basic pentagonal ring resonator embedded in a metal-insulator-metal (MIM) waveguide, the RL framework efficiently explored the multidimensional design space defined by geometric parameters such as radius, width, gap, and thickness. Even with a limited number of training episodes and steps, the agent successfully discovered optimized configurations that outperformed manually tuned designs.

In the first stage, the RL agent achieved a notable improvement in sensitivity from 2155.98 nm/RIU (unoptimized) to 2319.45 nm/RIU, confirming its ability to autonomously refine structural parameters for higher performance. With the introduction of nanorods as an additional tunable parameter, field confinement was further enhanced, raising the sensitivity to 2580.20 nm/RIU within only five episodes. In the final optimization stage, topological flexibility was introduced by allowing variation in the number of polygonal sides. This modification enabled the RL agent to evolve the resonator geometry from a pentagon to an octagon, resulting in the highest recorded sensitivity of 2814.45 nm/RIU.

Furthermore, when the figure of merit (FOM) was incorporated into the reward function alongside sensitivity, the model achieved a balanced optimization with a sensitivity of 2638.15 nm/RIU and an FOM of 10.71 RIU^{-1}. These outcomes emphasize the importance of integrating both geometrical and topological parameters within the inverse design process to achieve superior sensing performance.

Overall, this project demonstrates how deep learning, particularly reinforcement learning, can overcome the limitations of traditional trial-and-error-based optimization of plasmonic MIM refractive index sensors. The project also covers all the program outcomes and course outcomes, fulfilling the objectives of outcome-based education through the integration of advanced simulation, optimization, and analytical methods.

13.1 Future Work

Future work aims to enhance the current RL-based optimization framework by addressing computational limitations, expanding algorithmic strategies, and broadening application scopes. Decreasing simulation time through surrogate modeling or parallelized FDTD will accelerate learning cycles, while benchmarking RL against methods like GA and PSO can validate its efficiency. Various performance metrics beyond sensitivity, such as Q-factor or transmission, can be targeted using multi-objective reinforcement learning. The framework may also incorporate advanced algorithms like PPO or SAC for continuous and more stable optimization. Its adaptability will be tested on complex devices such as logic gates, switches, and filters, requiring richer state-action representations. Expanding geometry variations—e.g., multi-layered waveguides, nanohole patterns—will allow for more exhaustive design space exploration. Additionally, building custom datasets may support offline RL or supervised pretraining, aiding generalization across new sensing tasks or materials. These sensors can be integrated into PICs for applications like DEMUX or filtering, and adapted for real-world problems such as human disease diagnosis or environmental impurity detection, establishing RL as a powerful engine for intelligent, scalable inverse photonics design.

13.2 Limitations

Although the proposed inverse-designed plasmonic sensor achieved high sensitivity through simulation and optimization, several limitations remain that affect its computational efficiency, interpretability, and practical implementation. These are summarized below.

1. **High Computational Cost:** Performing full 3D FDTD simulations in conjunction with reinforcement learning algorithms required substantial

computational resources, including high memory usage and extended simulation times. This challenge was particularly pronounced when employing fine mesh resolutions and wide parameter sweeps.

2. **Slow Convergence:** The optimization process, especially within reinforcement learning frameworks, often exhibited slow convergence. A large number of episodes were required to achieve satisfactory performance, which increased overall computation time and occasionally led to premature stagnation.

3. **Lack of Physical Interpretability:** Machine learning-based inverse design introduced a "black-box" limitation, making it difficult to interpret why specific geometries exhibited superior sensitivity. This lack of transparency constrains the extraction of physical insights and limits generalization across different structures.

4. **Overfitting to Simulation Conditions:** Certain designs demonstrated excellent sensitivity under idealized simulation conditions but may not maintain similar performance under practical variations. This behavior indicates potential overfitting to specific boundary conditions and material parameters.

5. **Structural and Fabrication Constraints:** Despite their high simulated performance, some optimized geometries contain nanoscale gaps or complex 3D features that are difficult to realize with current nanofabrication technologies, thus limiting their experimental feasibility.

References

[1] N. L. Kazanskiy, S. N. Khonina, and M. A. Butt, "Plasmonic sensors based on metal–insulator–metal waveguides for refractive index sensing applications: A brief review," *Physica E: Low-Dimensional Systems and Nanostructures*, vol. 117, p. 113 798, Mar. 2020, ISSN: 1386-9477. DOI: 10.1016/j.physe.2019.113798.

[2] S. Mao, L. Cheng, C. Zhao, F. N. Khan, Q. Li, and H. Y. Fu, "Inverse design for silicon photonics: From iterative optimization algorithms to deep neural networks," *Applied Sciences*, vol. 11, no. 9, p. 3822, Apr. 2021. DOI: 10.3390/app11093822.

[3] M. E. Hamza, M. A. Othman, and M. A. Swillam, "Plasmonic biosensors: Review," *Biology*, vol. 11, no. 5, p. 621, May 2022, ISSN: 20797737. DOI: 10.3390/biology11050621.

[4] C. Caucheteur, T. Guo, and J. Albert, "Review of plasmonic fiber optic biochemical sensors: Improving the limit of detection," *Analytical and Bioanalytical Chemistry*, vol. 407, no. 14, pp. 3883–3897, May 2015, ISSN: 1618-2642. DOI: 10.1007/s00216-014-8411-6.

[5] R. A. Mahmud, R. H. Sagor, and M. Z. M. Khan, "Surface plasmon refractive index biosensors: A review of optical fiber, multilayer 2D material and gratings, and MIM configurations," *Optics & Laser Technology*, vol. 159, p. 108 939, Apr. 2023, ISSN: 00303992. DOI: 10.1016/j.optlastec.2022.108939.

[6] G. A. Khan, Y. Lu, and P. Wang, "Plasmon-enhanced refractive index sensing of biomolecules based on metal–dielectric–metal metasurface in the infrared regime," *ACS Omega*, vol. 9, no. 1, pp. 1416–1423, Jan. 2024, ISSN: 2470-1343. DOI: 10.1021/acsomega.3c07809.

[7] S. Verma, A. K. Pathak, and B. M. A. Rahman, "Review of biosensors based on plasmonic-enhanced processes in the metallic and meta-material-supported nanostructures," *Micromachines*, vol. 15, no. 4, p. 502, Apr. 2024, ISSN: 2072-666X. DOI: 10.3390/mi15040502.

[8] M. A. Butt, "Plasmonic sensors based on a metal–insulator–metal waveguide—what do we know so far?" *Sensors*, vol. 24, no. 22, p. 7158, Nov. 2024, ISSN: 1424-8220. DOI: 10.3390/s24227158.

[9] M. A. Butt, N. L. Kazanskiy, and S. N. Khonina, "Metal–insulator–metal waveguide plasmonic sensor system for refractive index sensing applications," *Advanced Photonics Research*, vol. 4, no. 7, p. 2 300 079, Jul. 2023, ISSN: 2699-9293. DOI: 10.1002/adpr.202300079.

[10] S. Guchhait, S. Chatterjee, T. Chakravarty, and N. Ghosh, "A metal–insulator–metal waveguide-based plasmonic refractive index sensor for the detection of nanoplastics in water," *Scientific Reports*, vol. 14, no. 1, pp. 1–9, Dec. 2024, ISSN: 2045-2322. DOI: 10.1038/s41598-024-71874-6.

[11] S. Molesky, Z. Lin, A. Y. Piggott, W. Jin, J. Vucković, and A. W. Rodriguez, "Inverse design in nanophotonics," *Nature Photonics*, vol. 12, no. 11, pp. 659–670, Nov. 2018, ISSN: 1749-4885. DOI: 10.1038/s41566-018-0246-9.

[12] W. Ma, Z. Liu, Z. A. Kudyshev, A. Boltasseva, W. Cai, and Y. Liu, "Deep learning for the design of photonic structures," *Nature Photonics*, vol. 15, no. 2, pp. 77–90, Feb. 2021, ISSN: 1749-4885. DOI: 10.1038/s41566-020-0685-y.

[13] R. S. Hegde, "Deep learning: A new tool for photonic nanostructure design," *Nanoscale Advances*, vol. 2, no. 3, pp. 1007–1023, Mar. 2020, ISSN: 2516-0230. DOI: 10.1039/C9NA00656G.

[14] P. R. Wiecha, A. Arbouet, C. Girard, and O. L. Muskens, "Deep learning in nano-photonics: Inverse design and beyond," *Photonics Research*, vol. 9, no. 5, B182, May 2021, ISSN: 2327-9125. DOI: 10.1364/PRJ.415960.

[15] B. Duan, B. Wu, J.-H. Chen, H. Chen, and D.-Q. Yang, "Deep learning for photonic design and analysis: Principles and applications," *Frontiers in Materials*, vol. 8, p. 791 296, Jan. 2022, ISSN: 2296-8016. DOI: 10.3389/fmats.2021.791296.

[16] D. Witt, J. Young, and L. Chrostowski, "Reinforcement learning for photonic component design," *APL Photonics*, vol. 8, no. 10, p. 106 101, Oct. 2023, ISSN: 2378-0967. DOI: 10.1063/5.0159928.

[17] S. Yan, M. Zhang, X. Zhao, Y. Zhang, J. Wang, and W. Jin, "Refractive index sensor based on a metal–insulator–metal waveguide coupled with a symmetric structure," *Sensors*, vol. 17, no. 12, p. 2879, Dec. 2017, ISSN: 1424-8220. DOI: 10.3390/s17122879.

[18] Z. Zhang et al., "Plasmonic refractive index sensor with high figure of merit based on concentric-rings resonator," *Sensors*, vol. 18, no. 1, p. 116, Jan. 2018, ISSN: 1424-8220. DOI: 10.3390/s18010116.

[19] M. Wang, M. Zhang, Y. Wang, R. Zhao, and S. Yan, "Fano resonance in an asymmetric MIM waveguide structure and its application in a refractive index nanosensor," *Sensors*, vol. 19, no. 4, p. 791, Feb. 2019, ISSN: 1424-8220. DOI: 10.3390/s19040791.

[20] C.-T. C. Chao et al., "Highly sensitive and tunable plasmonic sensor based on a nanoring resonator with silver nanorods," *Nanomaterials*, vol. 10, no. 7, p. 1399, Jul. 2020, ISSN: 2079-4991. DOI: 10.3390/nano10071399.

[21] M. F. Hassan, M. M. Hasan, M. I. Ahmed, and R. H. Sagor, "Numerical investigation of a plasmonic refractive index sensor based on rectangular MIM topology," in *2020 International Seminar on Intelligent Technology and Its Applications (ISITIA)*, IEEE, Jul. 2020, pp. 77–82, ISBN: 978-1-7281-7413-6. DOI: 10.1109/ISITIA49792.2020.9163755.

[22] R. H. Sagor, M. F. Hassan, S. Sharmin, T. Z. Adry, and M. A. R. Emon, "Numerical investigation of an optimized plasmonic on-chip refractive index sensor for temperature and blood group detection," *Results in Physics*, vol. 19, p. 103 611, Dec. 2020, ISSN: 2211-3797. DOI: 10.1016/j.rinp.2020.103611.

[23] R. H. Sagor, M. F. Hassan, A. A. Yaseer, E. Surid, and M. I. Ahmed, "Highly sensitive refractive index sensor optimized for blood group sensing utilizing the fano resonance," *Applied Nanoscience*, vol. 11, no. 2, pp. 521–534, Feb. 2021, ISSN: 2190-5509. DOI: 10.1007/s13204-020-01622-5.

[24] R. A. Mahmud, M. O. Faruque, and R. H. Sagor, "A highly sensitive plasmonic refractive index sensor based on triangular resonator," *Optics Communications*, vol. 483, p. 126 634, Mar. 2021, ISSN: 0030-4018. DOI: 10.1016/j.optcom.2020.126634.

[25] R. A. Mahmud, M. O. Faruque, and R. H. Sagor, "Plasmonic refractive index sensor based on ring-type pentagonal resonator with high sensitivity," *Plasmonics*, vol. 16, no. 3, pp. 873–880, Jun. 2021, ISSN: 1557-1955. DOI: `10.1007/s11468-020-01357-7`.

[26] K. S. Rashid, M. F. Hassan, A. A. Yaseer, I. Tathfif, and R. H. Sagor, "Gas-sensing and label-free detection of biomaterials employing multiple rings structured plasmonic nanosensor," *Sensing and Bio-Sensing Research*, vol. 33, p. 100 440, Aug. 2021, ISSN: 2214-1804. DOI: `10.1016/j.sbsr.2021.100440`.

[27] M. O. Faruque, R. A. Mahmud, and R. H. Sagor, "Highly sensitive plasmonic refractive index sensor using doped silicon: An alternative to MIM structures," *Plasmonics*, vol. 17, no. 1, pp. 203–211, Feb. 2022, ISSN: 1557-1955. DOI: `10.1007/s11468-021-01516-4`.

[28] I. Tathfif, M. F. Hassan, K. S. Rashid, A. A. Yaseer, and R. H. Sagor, "A highly sensitive plasmonic refractive index sensor based on concentric triple ring resonator for cancer biomarker and chemical concentration detection," *Optics Communications*, vol. 519, p. 128 429, Sep. 2022, ISSN: 0030-4018. DOI: `10.1016/j.optcom.2022.128429`.

[29] A. K. M. Rakib, A. T. B. Siddique, M. S. Sakib, M. O. Faruque, and R. H. Sagor, "A numerical analysis of a highly sensitive hexagonal plasmonic refractive index sensor," *Optics Communications*, vol. 530, p. 129 205, Mar. 2023, ISSN: 0030-4018. DOI: `10.1016/j.optcom.2022.129205`.

[30] R. Rahad, A. K. M. Rakib, M. A. Haque, S. S. Sharar, and R. H. Sagor, "Plasmonic refractive index sensing in the early diagnosis of diabetes, anemia, and cancer: An exploration of biological biomarkers," *Results in Physics*, vol. 49, p. 106 478, Jun. 2023, ISSN: 2211-3797. DOI: `10.1016/j.rinp.2023.106478`.

[31] A. K. M. Rakib, R. Rahad, M. O. Faruque, and R. H. Sagor, "ZrN-based plasmonic sensor: A promising alternative to traditional noble metal-based sensors for CMOS-compatible and tunable optical properties," *Optics Express*, vol. 31, no. 15, p. 25 280, Jul. 2023, ISSN: 1094-4087. DOI: `10.1364/OE.494550`.

[32] M. A. Haque, R. Rahad, A. K. M. Rakib, S. S. Sharar, and R. H. Sagor, "Plasmonic sensor for rapid detection of water adulteration in honey and

quantitative measurement of lactose concentration in solution," *Results in Physics*, vol. 51, p. 106 733, Aug. 2023, ISSN: 2211-3797. DOI: 10.1016/j.rinp.2023.106733.

[33] S. G. Shafagh and H. Kaatuzian, "Ultra-high-sensitive plasmonic sensor based on asymmetric hexagonal nano-ring resonator for cancer detection," *Heliyon*, vol. 10, no. 14, e34439, Jul. 2024, ISSN: 2405-8440. DOI: 10.1016/j.heliyon.2024.e34439.

[34] R. Rahad, M. A. Haque, M. O. Faruque, A. S. M. Mohsin, M. S. Mobassir, and R. H. Sagor, "A novel plasmonic MIM sensor using integrated 1 × 2 demultiplexer for individual lab-on-chip detection of human blood group and diabetes level in the visible to near-infrared region," *IEEE Sensors Journal*, vol. 24, no. 8, pp. 12 034–12 041, Apr. 2024, ISSN: 1530-437X. DOI: 10.1109/JSEN.2024.3372692.

[35] M. A. Kabir, A. Taharat, A. I. Keats, A. K. M. Rakib, M. Z. A. Rony, and R. H. Sagor, "High-performance demultiplexer-based lab-on-bio-chip sensor leveraging silicon photonics for point-of-care detection of hemoglobin and blood calcium ion levels," *Optics Express*, vol. 33, no. 9, p. 19 788, May 2025, ISSN: 1094-4087. DOI: 10.1364/OE.554834.

[36] A. Khodaie, H. Heidarzadeh, and F. V. Harzand, "Development of an advanced multimode refractive index plasmonic optical sensor utilizing split ring resonators for brain cancer cell detection," *Scientific Reports*, vol. 15, no. 1, p. 433, Jan. 2025, ISSN: 2045-2322. DOI: 10.1038/s41598-024-84761-x.

[37] M. Faraji, A. Jangjoy, and S. Matloub, "Octa-square split ring-shaped supercell-based plasmonic metamaterials for enhanced dual-spectral detection of cancer biomarkers," *Scientific Reports*, vol. 15, no. 1, p. 33 136, Sep. 2025, ISSN: 2045-2322. DOI: 10.1038/s41598-025-18418-8.

[38] M. A. Butt, "Numerical assessment of a metal–insulator–metal waveguide-based plasmonic sensor system for the recognition of tuberculosis in blood plasma," *Micromachines*, vol. 14, no. 4, p. 729, Mar. 2023, ISSN: 2072-666X. DOI: 10.3390/mi14040729.

[39] M. Danaie and A. Shahzadi, "Design of a high-resolution metal–insulator–metal plasmonic refractive index sensor based on a ring-shaped Si resonator," *Plasmonics*, vol. 14, no. 6, pp. 1453–1465, Dec. 2019, ISSN: 1557-1963. DOI: 10.1007/s11468-019-00926-9.

[40] R. Rahad, A. K. M. Rakib, M. K. Mahadi, and M. O. Faruque, "Fuel classification and adulteration detection using a highly sensitive plasmonic sensor," *Sensing and Bio-Sensing Research*, vol. 40, p. 100 560, Jun. 2023, ISSN: 2214-1804. DOI: 10.1016/j.sbsr.2023.100560.

[41] J. Jumper et al., "Highly accurate protein structure prediction with AlphaFold," *Nature*, vol. 596, no. 7873, pp. 583–589, Aug. 2021, ISSN: 0028-0836. DOI: 10.1038/s41586-021-03819-2.

[42] J. Abramson et al., "Accurate structure prediction of biomolecular interactions with AlphaFold 3," *Nature*, vol. 630, no. 8016, pp. 493–500, Jun. 2024, ISSN: 0028-0836. DOI: 10.1038/s41586-024-07487-w.

[43] A. Mirhoseini et al., "A graph placement methodology for fast chip design," *Nature*, vol. 594, no. 7862, pp. 207–212, Jun. 2021, ISSN: 0028-0836. DOI: 10.1038/s41586-021-03544-w.

[44] A. Fawzi et al., "Discovering faster matrix multiplication algorithms with reinforcement learning," *Nature*, vol. 610, no. 7930, pp. 47–53, Oct. 2022, ISSN: 0028-0836. DOI: 10.1038/s41586-022-05172-4.

[45] L. Yang et al., "Diffusion models: A comprehensive survey of methods and applications," *ACM Computing Surveys*, vol. 56, no. 4, pp. 1–39, Apr. 2024, ISSN: 0360-0300. DOI: 10.1145/3626235.

[46] W. X. Zhao et al., "A survey of large language models," *arXiv preprint arXiv:2303.18223*, Mar. 2025. DOI: 10.48550/arXiv.2303.18223.

[47] A. Merchant, S. Batzner, S. S. Schoenholz, M. Aykol, G. Cheon, and E. D. Cubuk, "Scaling deep learning for materials discovery," *Nature*, vol. 624, no. 7990, pp. 80–85, Dec. 2023, ISSN: 0028-0836. DOI: 10.1038/s41586-023-06735-9.

[48] R. Lam et al., "Learning skillful medium-range global weather forecasting," *Science*, vol. 382, no. 6677, pp. 1416–1421, Dec. 2023, ISSN: 0036-8075. DOI: 10.1126/science.adi2336.

[49] R. C. G. M. Loonen, S. de Vries, and F. Goia, "Inverse design for advanced building envelope materials, systems and operation," in *Rethinking Building Skins*. Elsevier, Jan. 2022, pp. 377–402, ISBN: 9780128224779. DOI: 10.1016/B978-0-12-822477-9.00022-X.

[50] R. Jabbar, R. Jabbar, and S. Kamoun, "Recent progress in generative adversarial networks applied to inversely designing inorganic materials: A brief review," *Computational Materials Science*, vol. 213, p. 111 612, Oct. 2022, ISSN: 0927-0256. DOI: 10.1016/j.commatsci.2022.111612.

[51] F. Bahrami, M. Maisonneuve, M. Meunier, J. S. Aitchison, and M. Mojahedi, "An improved refractive index sensor based on genetic optimization of plasmon waveguide resonance," *Optics Express*, vol. 21, no. 18, p. 20 863, Sep. 2013, ISSN: 1094-4087. DOI: 10.1364/OE.21.020863.

[52] C. M. Lalau-Keraly, S. Bhargava, O. D. Miller, and E. Yablonovitch, "Adjoint shape optimization applied to electromagnetic design," *Optics Express*, vol. 21, no. 18, p. 21 693, Sep. 2013, ISSN: 1094-4087. DOI: 10.1364/OE.21.021693.

[53] Ansys Optics, *Inverse design of waveguide crossing*. Accessed: Nov. 20, 2024. [Online]. Available: https://optics.ansys.com/hc/en-us/articles/360042305314-Inverse-design-of-waveguide-crossing.

[54] Ansys Optics, *Inverse design of y-branch*. Accessed: Nov. 20, 2024. [Online]. Available: https://optics.ansys.com/hc/en-us/articles/360042305274-Inverse-design-of-y-branch.

[55] Ansys Optics, *Inverse design of grating coupler (2d)*. Accessed: Nov. 20, 2024. [Online]. Available: https://optics.ansys.com/hc/en-us/articles/360042800573-Inverse-Design-of-Grating-Coupler-2D.

[56] J. Lu and J. Vučković, "Nanophotonic computational design," *Optics Express*, vol. 21, no. 11, p. 13 351, Jun. 2013, ISSN: 1094-4087. DOI: 10.1364/OE.21.013351.

[57] A. Y. Piggott, J. Lu, K. G. Lagoudakis, J. Petykiewicz, T. M. Babinec, and J. Vučković, "Inverse design and demonstration of a compact and broadband on-chip wavelength demultiplexer," *Nature Photonics*, vol. 9, no. 6, pp. 374–377, Jun. 2015, ISSN: 1749-4885. DOI: 10.1038/nphoton.2015.69.

[58] Z. S. Ballard, D. Shir, A. Bhardwaj, S. Bazargan, S. Sathianathan, and A. Ozcan, "Computational sensing using low-cost and mobile plasmonic readers designed by machine learning," *ACS Nano*, vol. 11, no. 2, p. 2266, Feb. 2017, ISSN: 1936-086X. DOI: 10.1021/ACSNANO.7B00105.

[59] X. Li, J. Shu, W. Gu, and L. Gao, "Deep neural network for plasmonic sensor modeling," *Optical Materials Express*, vol. 9, no. 9, pp. 3857–3862, Sep. 2019, ISSN: 2159-3930. DOI: 10.1364/OME.9.003857.

[60] T. Zhang et al., "Efficient spectrum prediction and inverse design for plasmonic waveguide systems based on artificial neural networks," *Photonics Research*, vol. 7, no. 3, pp. 368–380, Mar. 2019, ISSN: 2327-9125. DOI: 10.1364/PRJ.7.000368.

[61] E. Adibnia, M. A. Mansouri-Birjandi, M. Ghadrdan, and P. Jafari, "A deep learning method for empirical spectral prediction and inverse design of all-optical nonlinear plasmonic ring resonator switches," *Scientific Reports*, vol. 14, no. 1, p. 5787, Mar. 2024, ISSN: 2045-2322. DOI: 10.1038/s41598-024-56522-3.

[62] E. Adibnia, M. Ghadrdan, and M. A. Mansouri-Birjandi, "Nanophotonic structure inverse design for switching application using deep learning," *Scientific Reports*, vol. 14, no. 1, p. 21 094, Sep. 2024, ISSN: 2045-2322. DOI: 10.1038/s41598-024-72125-4.

[63] E. Adibnia, M. Ghadrdan, and M. A. Mansouri-Birjandi, "Inverse design of octagonal plasmonic structure for switching using deep learning," *Results in Physics*, vol. 71, p. 108 197, Apr. 2025, ISSN: 2211-3797. DOI: 10.1016/j.rinp.2025.108197.

[64] S. Khani, P. Rezaei, and M. Rahmanimanesh, "Machine learning analysis of a Fano resonance-based plasmonic refractive index sensor using u-shaped

resonators," *Scientific Reports*, vol. 15, no. 1, p. 23 857, Jul. 2025, ISSN: 2045-2322. DOI: 10.1038/s41598-025-08508-y.

[65] S. A. Zonouri, A. Basem, and Y. M. A. Al-zahy, "Innovative MIM diplexer with neural network enhanced refractive index detection for advanced photonic applications," *Scientific Reports*, vol. 14, no. 1, p. 31 473, Dec. 2024, ISSN: 2045-2322. DOI: 10.1038/s41598-024-83066-3.

[66] A. Darabi and M. R. Malekshahi, "Design and optimization of a compact dual-band metal–insulator–metal filter for high sensitivity refractive index sensing using particle swarm optimization," *Scientific Reports*, vol. 15, no. 1, p. 22 436, Jul. 2025, ISSN: 2045-2322. DOI: 10.1038/s41598-025-05569-x.

[67] A. Khalilian and H. N. Rad. "Design optimized CMOS-compatible hybrid silicon MIM waveguide cavity for label-free sensing." Preprint. arXiv: 2508.18291. [Online]. Available: https://arxiv.org/pdf/2508.18291.

[68] S. A. Zonouri and M. Hayati, "Design of a MIM sensor using an optical resonator and GMDH algorithm for high efficiency applications," *Journal of Computational Electronics*, vol. 23, no. 2, pp. 467–480, Apr. 2024, ISSN: 1569-8025. DOI: 10.1007/s10825-024-02136-x.

[69] K. Hamada, H.-H. Hsiao, and W. Kubo, "Comparison of algorithms using deep reinforcement learning for optimization of hyperbolic metamaterials," *Scientific Reports*, vol. 14, no. 1, p. 31 842, Dec. 2024, ISSN: 2045-2322. DOI: 10.1038/s41598-024-83167-z.

[70] T. Badloe, I. Kim, and J. Rho, "Biomimetic ultra-broadband perfect absorbers optimised with reinforcement learning," *Physical Chemistry Chemical Physics*, vol. 22, no. 4, pp. 2337–2342, Jan. 2020, ISSN: 1463-9076. DOI: 10.1039/C9CP05621A.

[71] L. Rosafalco, J. M. D. Ponti, L. Iorio, R. V. Craster, R. Ardito, and A. Corigliano, "Reinforcement learning optimisation for graded metamaterial design using a physical-based constraint on the state representation and action space," *Scientific Reports*, vol. 13, no. 1, p. 21 836, Dec. 2023, ISSN: 2045-2322. DOI: 10.1038/s41598-023-48927-3.

[72] X. Xu, D. Aggarwal, and K. Shankar, "Instantaneous property prediction and inverse design of plasmonic nanostructures using machine learning: Current applications and future directions," *Nanomaterials*, vol. 12, no. 4, p. 633, Feb. 2022, ISSN: 2079-4991. DOI: 10.3390/nano12040633.

[73] S. A. Maier, *Plasmonics: Fundamentals and Applications.* New York: Springer, 2007, ISBN: 978-0-387-37825-1. DOI: 10.1007/0-387-37825-1.

[74] A. D. Rakić, A. B. Djurišić, J. M. Elazar, and M. L. Majewski, "Optical properties of metallic films for vertical-cavity optoelectronic devices," *Applied Optics*, vol. 37, no. 22, pp. 5271–5283, Aug. 1998, ISSN: 1559-128X. DOI: 10.1364/AO.37.005271.

[75] P. B. Johnson and R. W. Christy, "Optical constants of the noble metals," *Physical Review B*, vol. 6, no. 12, pp. 4370–4379, Dec. 1972, ISSN: 2469-9969. DOI: 10.1103/PhysRevB.6.4370.

[76] E. D. Palik, Ed., *Handbook of Optical Constants of Solids.* Orlando: Academic Press, 1985, ISBN: 978-0-12-544415-6. [Online]. Available: https://www.sciencedirect.com/book/9780125444156/handbook-of-optical-constants-of-solids.

[77] M. A. Ordal, R. J. Bell, R. W. Alexander, L. L. Long, and M. R. Querry, "Optical properties of the metals al, co, cu, au, fe, pb, ni, pd, pt, ag, ti, and w in the infrared and far infrared," *Applied Optics*, vol. 22, no. 7, pp. 1099–1119, Apr. 1983, ISSN: 1559-128X. DOI: 10.1364/AO.22.001099.

[78] "Detailed explanation of the finite element method (FEM)," COMSOL, Accessed: Oct. 7, 2025. [Online]. Available: https://www.comsol.com/multiphysics/finite-element-method.

[79] F. Pisano et al., "Plasmonics on a neural implant: Engineering light–matter interactions on the nonplanar surface of tapered optical fibers," *Advanced Optical Materials*, vol. 10, no. 2, p. 2 101 649, Jan. 2022, ISSN: 2195-1071. DOI: 10.1002/adom.202101649.

[80] "What is finite element analysis (FEA)?" Ansys, Accessed: Oct. 7, 2025. [Online]. Available: https://www.ansys.com/simulation-topics/what-is-finite-element-analysis.

[81] "What is finite-difference time-domain (FDTD)?" Ansys, Accessed: Oct. 7, 2025. [Online]. Available: https://www.ansys.com/blog/what-is-fdtd.

[82] F. L. Teixeira et al., "Finite-difference time-domain methods," *Nature Reviews Methods Primers*, vol. 3, no. 1, pp. 1–19, Dec. 2023, ISSN: 2662-8449. DOI: 10.1038/S43586-023-00257-4.

[83] "A Maxwell's equations based deep learning method for time domain electromagnetic simulations," IEEE Xplore, Accessed: Oct. 7, 2025. [Online]. Available: https://ieeexplore.ieee.org/document/9350148.

[84] P. Zhang, Y. Hu, Y. Jin, S. Deng, X. Wu, and J. Chen, "A Maxwell's equations based deep learning method for time domain electromagnetic simulations," *IEEE Journal on Multiscale and Multiphysics Computational Techniques*, vol. 6, pp. 35–40, 2021, ISSN: 2379-8793. DOI: 10.1109/JMMCT.2021.3057793.

[85] H. Yang, X. Zeng, and X. Wu, "An approach to solving Maxwell's equations in time domain," *Journal of Mathematical Analysis and Applications*, vol. 518, no. 1, p. 126 678, Feb. 2023, ISSN: 0022-247X. DOI: 10.1016/J.JMAA.2022.126678.

[86] U. S. Inan and R. A. Marshall, "The FDTD grid and the Yee algorithm," in *Numerical Electromagnetics*, Cambridge University Press, Jun. 2011, pp. 72–112. DOI: 10.1017/CBO9780511921353.005.

[87] X. Wu, X. Bao, J. Shen, X. Chen, and H. Cui, "Evaluation of void defects behind tunnel lining through GPR forward simulation," *Sensors*, vol. 22, no. 24, p. 9702, Dec. 2022, ISSN: 1424-8220. DOI: 10.3390/S22249702.

[88] L. F. Shampine, "Stability of the leapfrog/midpoint method," *Applied Mathematics and Computation*, vol. 208, no. 1, pp. 293–298, Feb. 2009, ISSN: 0096-3003. DOI: 10.1016/J.AMC.2008.11.029.

[89] K. Hosseini, "CFL stability conditions for the FDTD method in bounded inhomogeneous anisotropic media," *Iranian Journal of Electrical and Electronic Engineering*, vol. 18, no. 2, p. 2398, Jun. 2022, ISSN: 2383-3890. DOI: 10.22068/IJEEE.18.2.2398.

[90] S. D. Gedney and B. Zhao, "An auxiliary differential equation formulation for the complex-frequency shifted PML," *IEEE Transactions on Antennas and Propagation*, vol. 58, no. 3, pp. 838–847, Mar. 2010, ISSN: 0018-926X. DOI: 10.1109/TAP.2009.2037765.

[91] G. Xie et al., "Auxiliary differential equation (ADE) method-based complying-divergence implicit FDTD method for simulating general dispersive anisotropic material," *Optics Express*, vol. 31, no. 11, p. 18 468, May 2023, ISSN: 1094-4087. DOI: 10.1364/OE.490074.

[92] A. S. Jasim, Z. K. Ghazal, and N. A. Hasson, "Z-transform solution for partial difference equations," *International Academic Journal of Science and Engineering*, vol. 11, no. 1, pp. 295–303, Jun. 2024, ISSN: 2454-3896. DOI: 10.9756/IAJSE/V11I1/IAJSE1134.

[93] "The Z-transform: A practical overview," ResearchGate, Accessed: Oct. 7, 2025. [Online]. Available: https://www.researchgate.net/publication/370660126_The_z-transform_A_practical_overview.

[94] C. Jin, B. Zhou, S. Greenhalgh, M. J. Zemerly, M. K. Riahi, and D. Cao, "An accurate and efficient recursive convolution method to simulate viscoacoustic and viscoelastic waves," *IEEE Transactions on Geoscience and Remote Sensing*, vol. 62, pp. 1–12, 2024, ISSN: 1558-0644. DOI: 10.1109/TGRS.2024.3393613.

[95] S. D. Gedney, *Introduction to the Finite-Difference Time-Domain (FDTD) Method for Electromagnetics*. Springer International Publishing, 2011, ISBN: 978-3-031-00584-8. DOI: 10.1007/978-3-031-01712-4.

[96] "Meep documentation," Massachusetts Institute of Technology, Accessed: Oct. 4, 2025. [Online]. Available: https://meep.readthedocs.io/en/latest/.

[97] "Fdtd+," Photon Design Ltd., Accessed: Oct. 4, 2025. [Online]. Available: http://www.fdtdxx.com/.

[98] "Fullwave fdtd simulation software – rsoft photonic device tools — synopsys photonic solutions," Synopsys Inc., Accessed: Oct. 4, 2025. [Online]. Available: https://www.synopsys.com/photonic-solutions/rsoft-photonic-device-tools/passive-device-fullwave.html.

[99] "Fast, modern photonic simulations: Flexcompute tidy3d," Flexcompute Inc., Accessed: Oct. 4, 2025. [Online]. Available: https://www.flexcompute.com/tidy3d/.

[100] "Ansys lumerical fdtd — simulation for photonic components," Ansys Inc., Accessed: Oct. 4, 2025. [Online]. Available: https://www.ansys.com/products/optics/fdtd.

[101] "Python api – lumapi — ansys developer portal," Ansys Inc., Accessed: Oct. 4, 2025. [Online]. Available: https://developer.ansys.com/docs/lumerical/python-lumapi.

[102] "Boundary conditions in feem – simulation object — ansys optics," Ansys Inc., Accessed: Oct. 4, 2025. [Online]. Available: https://optics.ansys.com/hc/en-us/articles/1500011104881-Boundary-conditions-in-FEEM-Simulation-Object.

[103] "Periodic boundary conditions in fdtd and mode — ansys optics," Ansys Inc., Accessed: Oct. 4, 2025. [Online]. Available: https://optics.ansys.com/hc/en-us/articles/360034382734-Periodic-boundary-conditions-in-FDTD-and-MODE.

[104] "Pml boundary conditions in fdtd and mode — ansys optics," Ansys Inc., Accessed: Oct. 4, 2025. [Online]. Available: https://optics.ansys.com/hc/en-us/articles/360034382674-PML-boundary-conditions-in-FDTD-and-MODE.

[105] "Symmetric and anti-symmetric bcs in fdtd and mode — ansys optics," Ansys Inc., Accessed: Oct. 4, 2025. [Online]. Available: https://optics.ansys.com/hc/en-us/articles/360034382694-Symmetric-and-anti-symmetric-BCs-in-FDTD-and-MODE.

[106] "Common features in Ansys Lumerical FDTD — lesson 1," Ansys Innovation Courses, Accessed: Oct. 5, 2025. [Online]. Available: https://innovationspace.ansys.com/courses/courses/lumerical-fdtd-sources/lessons/common-features-in-ansys-lumerical-fdtd-lesson-1/.

[107] "Transmittance – an overview," ScienceDirect Topics, Accessed: Oct. 5, 2025. [Online]. Available: https://www.sciencedirect.com/topics/physics-and-astronomy/transmittance.

[108] "Reflectance – an overview," ScienceDirect Topics, Accessed: Oct. 5, 2025. [Online]. Available: https://www.sciencedirect.com/topics/physics-and-astronomy/reflectance.

[109] M. Ladd, *Introduction to Physical Chemistry*. Cambridge University Press, Jan. 1998, ISBN: 9780521480000. DOI: 10.1017/CBO9781139170925.

[110] "SPR sensitivity and detection limit," Biosensing USA, Accessed: Oct. 5, 2025. [Online]. Available: https://www.biosensingusa.com.

[111] O. Rainio, J. Hällilä, J. Teuho, and R. Klén, "Methods for estimating full width at half maximum," *Signal, Image and Video Processing*, vol. 19, no. 4, pp. 1–7, Apr. 2025, ISSN: 1863-1711. DOI: 10.1007/S11760-025-03820-6.

[112] "Figure of merit – an overview," ScienceDirect Topics, Accessed: Oct. 5, 2025. [Online]. Available: https://www.sciencedirect.com/topics/chemistry/figure-of-merit.

[113] A. Khatoon, A. Daud, and T. Amjad, "Categorization and correlational analysis of quality factors influencing citation," *Artificial Intelligence Review*, vol. 57, no. 3, pp. 1–52, Mar. 2024, ISSN: 1573-7462. DOI: 10.1007/S10462-023-10657-3.

[114] L. S. P. Maia et al., "Inverse design of plasmonic nanostructures using machine learning for optimized prediction of physical parameters," *Photonics*, vol. 12, no. 6, p. 572, Jun. 2025, ISSN: 2304-6732. DOI: 10.3390/PHOTONICS12060572.

[115] "Shape optimization of nanophotonic devices using the adjoint method," IEEE Xplore, Accessed: Oct. 5, 2025. [Online]. Available: https://ieeexplore.ieee.org/document/6989970.

[116] J. S. Jensen and O. Sigmund, "Topology optimization for nano-photonics," *Laser & Photonics Reviews*, vol. 5, no. 2, pp. 308–321, Mar. 2011, ISSN: 1863-8899. DOI: 10.1002/LPOR.201000014.

[117] "What is reinforcement learning?" IBM, Accessed: Oct. 5, 2025. [Online]. Available: https://www.ibm.com/think/topics/reinforcement-learning.

[118] "Reinforcement learning for AI agents: Frameworks, algorithms, and real-world applications," NeuralDNA, Accessed: Oct. 5, 2025. [Online]. Available: https://neuraldna.com/reinforcement-learning-ai-agents/.

[119] "Markov decision processes – 6.390: Introduction to machine learning," Massachusetts Institute of Technology, Accessed: Oct. 5, 2025. [Online]. Available: https://introml.mit.edu/notes/mdp.html.

[120] B. Jang, M. Kim, G. Harerimana, and J. W. Kim, "Q-learning algorithms: A comprehensive classification and applications," *IEEE Access*, vol. 7, pp. 133 653–133 667, 2019. DOI: 10.1109/ACCESS.2019.2941229.

[121] "Beginner's guide to policy in reinforcement learning," Machine Learning Knowledge, Accessed: Oct. 5, 2025. [Online]. Available: https://machinelearningknowledge.ai/beginners-guide-to-what-is-policy-in-reinforcement-learning/.